University of Southampton

THE ELECTRODEPOSITION OF MESOPOROUS TYPE II-VI SEMICONDUCTORS

by
Tim Gabriel

A dissertation submitted in partial fulfilment of the requirements of the degree of Doctor of Philosophy at the University of Southampton

School of Chemistry
June 2007

UNIVERSITY OF SOUTHAMPTON
FACULTY OF ENGINEERING, SCIENCE AND MATHEMATICS
SCHOOL OF CHEMISTRY

Doctor of Philosophy

ABSTRACT

The electrodeposition of mesoporous type II-VI semiconductors
By Tim Gabriel

It has recently been demonstrated that lyotropic liquid crystalline mesophases of non-ionic surfactants can act as nano-scale templates for the electrochemical growth of adherent high-quality metal (e.g. platinum, palladium and cobalt) and elemental semiconductor (e.g. selenium) films leading to well-defined periodic three-dimensional interconnected nanostructures. We report the synthesis of a uniform, high-quality metalloid, tellurium films and II-VI semiconductor compound films of CdTe and ZnO with a hexagonal nanoarchitecture fabricated via this true liquid crystal templating route.

The preparation of the nanostructured mesoporous films was carried out by cathodic electrochemical deposition of various metal semimetal species dissolved in the aqueous domain of the hexagonal lyotropic liquid crystalline phase (H_I) of the non-ionic surfactants octaethyleneglycol monohexadecyl ether ($C_{16}EO_8$) and Brij®56. The deposition mechanism was based on cyclic voltammetry studies. The influence of experimental factors such as the deposition potential, electrolyte composition, additives, temperature were studied in order to improve the surface morphology, crystallinity and nanostructuring of the electrodeposited film. The template mixtures and films were characterised by X-ray diffraction (XRD), transmission electron microscopy (TEM) and polarising optical microscopy (POM) to ascertain the presence of a regular nanostructure. The XRD and TEM data are consistent with the expected H_I nanostructure.

The ability to electrodeposit mesoporous nanostructured semiconductors highlights the possibility of creating a new class of materials that would exhibit unusual electronic and optical properties. We will discuss the results of finite-element electromagnetic simulations and the extent to which the film's optical properties can be understood in terms of form birefringence. Further characterisation of the films was carried out on cadmium telluride films using UV-Vis measurements taken with a metallurgical microscope. These measurements can also demonstrate that such structuring within a film produces strong birefringence, for wavelengths both above and below the semiconductor's bandgap. Preliminary results on bandstructure modification caused by the nanostructuring of these materials will also be presented.

ACKNOWLEDGEMENTS

To Iris for the unbelievable times, ask anyone! You have been a marvel to watch in action and I have learnt a great deal from you. To you, the utmost respect and appreciation to your patience and perseverance and you taking a chance on a Northerner with a funny accent and a laid back swagger.

Xiaohong, it has been a pleasure. I am forever indebted to you for your genius and knowledge in the areas of electrochemistry. George Attard, for all the recognition and belief without it I would have been shelf stacking.

Big up to the Physics chaps: Matt Markham and David Smith two of the nicest physicists I know. Without these guys my PhD wouldn't have been the gem that it is! Seriously, their relentless hard work and enthusiasm have been motivational and astounding. They have both become my work role models.

Many thanks to the people at Merck especially Rod Riddle and Martin Pellat. They provided me with a life and career after the PhD. They saw a potential in me that has led me to greater things, fuelling my thirst for success.

Respect to dem Southampton mans. To Doug: may 'Thought for the day', daily Google searches and 'the wall of heroes' live long in our memories. Thanks for the idle chit chat and the pricks of morality. To Chris: the nicest guy I know, thanks for the smiles and daily support. Thanks to everyone else on the seventh floor and the department who provided support, smiles and instruments.

I shouldn't forget the Northern contingency; Stephens, Damien, Aran, Quincey and Tulip who put up with the lengthy rants, my tardiness, and who helped me meet my quota of holidays for the year.

Special thanks goes to Pops. My soulmate, punch bag and all manner of tension relief. Without you this would have never have been impossible, and I would have ended up in Stores Hall. No-one could ever imagine how much you did to get me through this PhD. I thank you.

Dedicated to Mardi, Pardi, Gabriel, Paul and the late Kitty, without you this would have merely been a dream....

CONTENTS PAGES

CHAPTER ONE:

INTRODUCTION

1.1. Introduction to mesoporous materials

The fabrication and design of materials with controlled nano-architectures has emerged as an active research area that is of fundamental and technological importance (*1*). Physical properties (e.g. catalytic, magnetic) of nanostructured materials can differ immensely from the respective properties of their bulk counterparts. The difference comes from a high internal surface area which is created by a network of nanostructured channels. For example, nanostructured mesoporous cobalt possesses a magnetic coercivity of almost two orders of magnitude greater than that of the non-mesoporous film (2). The introduction of mesoporosity into platinum powder improves the specific surface area from 35 $m^2\ g^{-1}$ for platinum black to 60 $m^2\ g^{-1}$ for mesoporous platinum powder (3), thus providing enhanced catalytic activity. Finally, mesoporous tin electrodes reduce the degradation caused by the insertion and removal of lithium ions, thus giving rise to increased battery life times (*4*). The technological importance of these metals, semiconductors, metal oxides and alloys ranges from their use as electrocatalysts and batteries, supercapacitors, fuel cells and sensors, (*4-6*) and a number of other physically enhanced materials.

The introduction of a porous network of channels into type II-VI semiconductors may create a material with highly functional electronic and optical properties. This may lead to a modification of the band gap energy due to the quantum confinement effects. Quantum confinement effects have been observed in semiconductor nanoparticles, where the radius of the nanoparticles was reduced from 3.8 to 3.2 nm leading to an increase in the bandgap energy from 1.57 to 1.60 eV (*7*). Much larger effect was observed with CdSe and PbS.

1.2. Mesoporous materials

1.2.1 Porosity

Porosity describes the fraction of the porous sample's bulk volume occupied by pores of void space. A classification based on the pore size diameter was proposed by IUPAC (the International Union of Pure and Applied Chemistry) and is shown in table 1.1.

Table 1: IUPAC classification of pore sizes

Pore Type	Pore Width
macropore	>50 nm
mesopore	2-50 nm
supermicropore	1.4-2 nm
micropore	0.5-1.4 nm
ultramicropore	0.5 nm

Porous materials have a plethora of uses, as mentioned in section 1.1, and pore size is a significant factor in determining their function. For example, the adsorption of gases and liquids in activated carbons (a porous carbon material) occurs through van der Waals' forces of attraction and capillary action (*8*), and therefore these porous material are used as molecular sieves. However, the use of these as simple molecular sieves has changed, and the correct type of porosity within a material can induce properties such as form birefringence (*9*) and quantum confinement. Control of the pore size is restricted due to the preparative methods and inherent structure of the material such as in zeolites, where pore sizes and cages are restricted to about 1.5 nm. This type of material (with pore sizes in the 1.5 nm range) also proves to be restrictive for many catalytic applications such as cracking heavier fractions of crude oil and sieving biomolecules and metals with bulky ligands.

1.2.2 Activated carbons

Activated carbons are an example of simple porous materials, originating from carbonaceous materials such as bituminous coal, coconut shell or wood (figure 1.1) (*10*). These carbon precursors are transformed into activated carbons by a gasification process followed by pore enlargement process. The carbon surface can then be functionalised by heating it in the presence of CH_4, H_2O CO_2, CO and O_2, which allows selective adsorption within the pores for particular applications such as molecular sieves (*11*). These materials contain a series of channels of non-uniform size and shape, thus making pore filling and pore size measurement difficult (*12*). The simplicity and availability of this material make it a useful molecular sieve or catalyst. The random yet useful structure of these materials encouraged a drive to develop more functional materials possessing highly defined size and shape porosities.

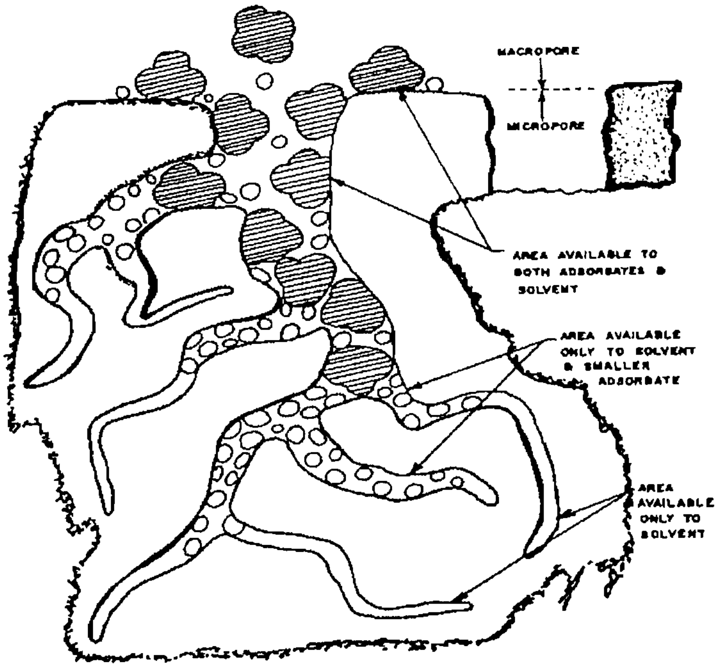

Figure 1.1: The adsorptive effects of the carbon pore.

1.2.3 Zeolites

The highly uncontrollable formation of the porous system in activated carbons and the irregularity of the pore size and shape distribution restricted the utility of these materials. However, by the 1950's a new type of porous material called a Zeolite, had been created. Zeolites are silicate materials generally composed of aluminosilicate and consisting of a periodic three-dimensional crystalline framework structure containing pore holes (cages) in the microporous region, with an average diameter of 1-1.4 nm. They were the first mesoporous material to be synthesized with control over the desired pore sizes. The crystalline nature of zeolites provides a well defined, uniform structure.

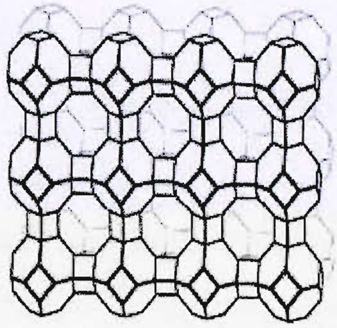

Figure 1.2: The organised 3-dimensional pore structure of a crystalline microporous material Zeolite A [LTA], with the molar composition of the synthesis solution: 6.1-1.58SiO_2:Al_2O_3:17Na_2O:0.9-6.5$(TMA)_2O$:389H_2O:3$^iPrO_2$

Zeolites are generally synthesised by the hydrothermal crystallization of a heterogeneous gel, consisting of a liquid and a solid phase. The reaction media contains cation(s) (e.g. Si, Al, P) which form a framework, sources of a mineralizing agent (e.g. HO^-, F^-); mineral cations or organic species (cations or neutral molecules); and a solvent (*13*). Figure 1.2 shows an example of a Zeolite, (LTA).

These synthetic materials can be used for selective catalysis or the separation of gases or liquids. Zeolites can be used as catalysts and also be found in household goods such as washing powders and water softeners, with approximately 70 % of all zeolites being used in detergents (*14*). More interestingly they can be used in the conversion of petroleum to methanol (*15*). Their high surface area and controlled pore size distribution has created viable uses as ion exchangers, catalysts and catalyst supports and also in adsorption and molecular sieving processes (*16*). However, zeolites have a limited pore size, and therefore low accessibility of the pores. Increasing the control over pore size and shape dimensions would give rise to greater industrial applications for porous materials, enabling them to act as more precise and more functional tools.

1.3. The use of liquid crystals as a template in the preparation of mesoporous materials

The demand for a greater range of pore sizes gave reason to develop new methods of fabricating porous materials by employing surfactants such as pluronics and polyoxyethylene glycols to act as structure directing aids and templates. These surfactants form liquid crystal mesophases and heralded a new era in tailoring porous materials, giving even greater control over the pore size and shape by comparison to the zeolites.

1.3.1 Liquid crystals (LC)

Crystals and liquids are differentiated by the molecular ordering within them. Molecules in a crystal are positionally and orientationally ordered, whereas molecules in a liquid diffuse randomly throughout a sample container. However, between these two phases exists a molecular ordering which is more pronounced than in liquids and less ordered than in crystals. This phase is called the liquid crystal phase and shares properties of both liquids and crystals.

Liquid crystal formation occurs via the self-assembly of specific molecules whose structural arrangement lies between that of a crystalline solid and an isotropic liquid. These structures can be affected by external physical conditions such as temperature, pH and concentration of the polar solvent and surfactant itself. The liquid crystals can be grouped into two types (figure 1.3):

a. Lyotropic – the formation of lyotropic liquid crystals is dependant on concentration in a polar solvent and temperature (figure 1.3a).
b. Thermotropic – the formation of thermotropic liquid crystals is dependant on the temperature (figure 1.3b).

Thermotropic liquid crystals usually consist of rod or disc shaped molecules with a rigid core and flexible peripheral alkyl tails. 4-pentyl-4′-cyanobiphenyl (5CB), a rod shaped molecule is commonly used (figure 1.3b), but more complex materials such as myristate, and 4-pentylphenyl-trans-4′ pentylcycloheycl carboxylate are also used.

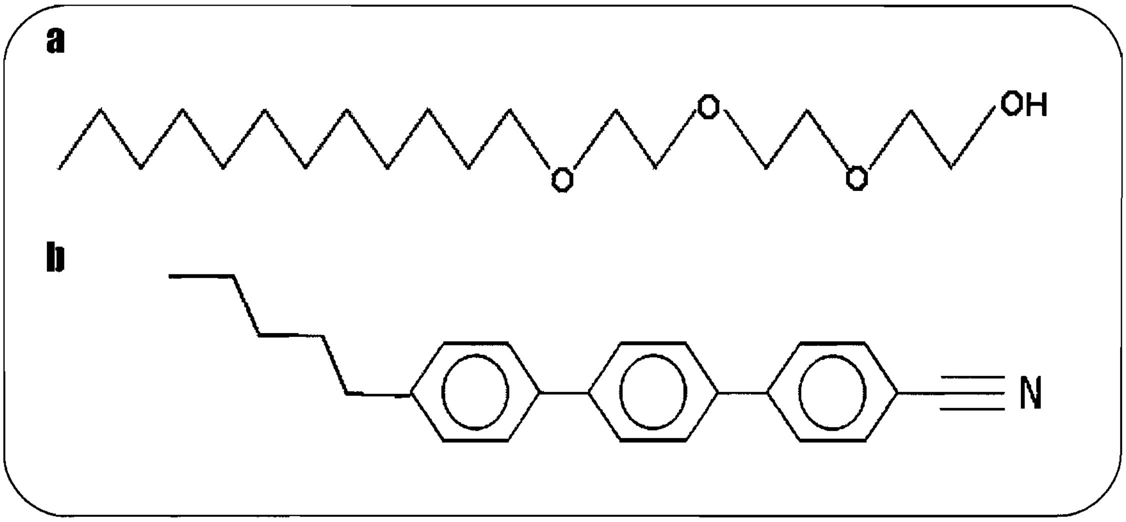

Figure 1.3: Two types of molecules which form liquid crystals by self-assembly: a). lyotropic liquid crystal surfactant molecule, $C_{12}EO_4$ and b). a thermotropic liquid crystal molecule 5-cyanobutadibenzene.

For the formation of a liquid crystal as a template for materials, lyotropic liquid crystalline phases are formed by surfactant molecules at high concentrations (>30 wt. %). Table 1.2 shows surfactants employed for liquid crystal templating, such as non-ionic polyoxyethylene (POE) surfactants (e.g., $C_{16}EO_8$) and polymeric surfactants (e.g., pluronics). It is also possible to find cationic surfactants such as cetyltrimethylammonium bromide (CTAB), and anionic surfactants like sodium dodecyl sulphate (SDS) which form liquid crystalline phases. The type of amphiphilic surfactant molecule is described by the charge on the head group (CTAB has an ammonium ion positioned at the end of the molecule).

Lyotropic liquid crystals form in polar solvents (e.g. water) due to the hydrophobic effect. In water, 3 to 3.5 hydrogen bonds are present between water molecules and the entropy between the molecules is at its highest. However, the addition of surfactant molecules to water would require water molecules to form 3.5 to 4 hydrogen bonds (surfactant molecules repel the water molecules), therefore decreasing the entropy in the solution. This is energetically unfavourable therefore surfactant molecules aggregate dynamically and collectively into a variety of phases, depending on the concentration. to avoid this. Water molecules also push the surfactant molecules together, reducing the effect of the surfactant molecules and increasing the entropy.

Table 1.2: Surfactants used to make lyotropic liquid crystals.

Surfactant	Structure	Description
$C_{16}EO_8$	$CH_3(CH_2)_{15}(OCH_2CH_2)_8OH$ Octaethylene glycol monohexadecyl ether	Non-ionic surfactants Expensive as pure materials
$C_{12}EO_8$	$CH_3(CH_2)_{11}(OCH_2CH_2)_8OH$ Octaethylene glycol monododecyl ether	
Brij®56	$CH_3(CH_2)_{15}(OCH_2CH_2)_{10}OH$ Decaethylene glycol monohexadecyl ether (average ethylene glycol chain length of 10)	Non-ionic surfactants Cheap Low level of purity
Pluronics (P123)	$HO(OCH_2CH_2)_x(OCH_2CH_2CH_2)_y(OCH_2CH_2)_xOH$ and variations of.	Non-ionic surfactant Long chain block copolymer
CTAB	$CH_3(CH_2)_{15}N(CH_3)_3Br$ Cetyltrimethylammonium Bromide	Cationic surfactant Cheap Commonly used to prepare M41S materials

1.3.2 Templating structures

Surfactant molecules (Table1.2) are bifunctional amphiphilic molecules containing a water insoluble (hydrophobic) hydrocarbon tail and a water soluble (hydrophilic) head group such as hydroxyl groups (figure 1.4a). When mixed with a polar solvent the surfactant molecules aggregate to form micelles (due to the hydrophobic effect), provided that the surfactant concentration is above the critical micelle concentration (CMC), normally >1 % (figure 1.4b). The hydrophobic sections of the molecules position themselves on the inside of the aggregate and hydrophilic parts on the outside. Figure 1.4c shows that at 50wt.% $C_{16}EO_8$ and 50wt.% water the surfactant can go on to form the hexagonal phase (figure 1.4c).

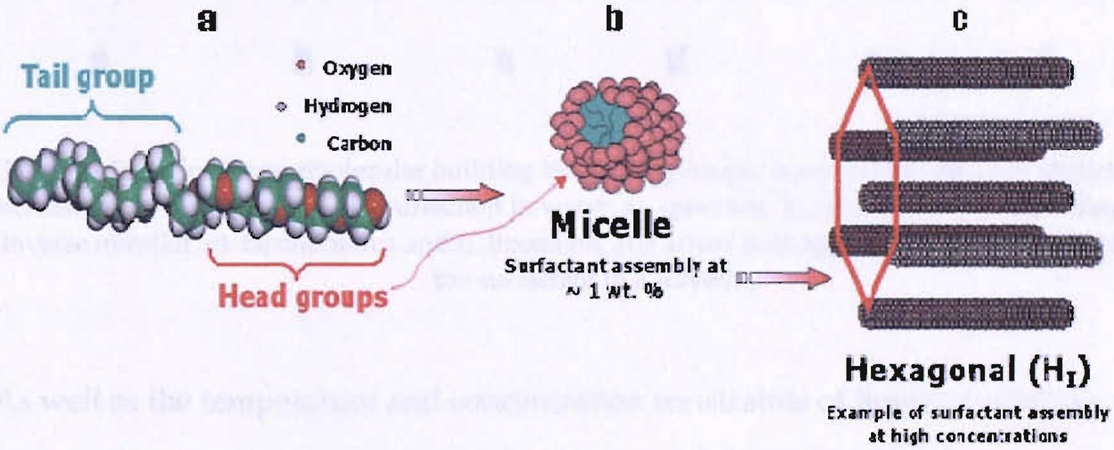

Figure 1.4: a). the $C_{16}EO_8$ surfactant molecule b).upon increasing its concentration in water to the critical micellar concentration (CMC) c). upon increasing its concentration to ~50 wt.% to form the hexagonal (H_I) mesophase phase.

In this structure the aggregates arrange themselves as cylindrical rod-like structures with varying length, to form a closely packed hexagonal lattice. Temperature and concentration are two important factors in the self-assembly of liquid crystal mesophases. For example, at a given temperature, increasing the concentration of the amphiphile to concentrations higher than the CMC leads to the development of other topological structures, as shown in Figure 1.5

(*17*). The planar bilayer as illustrated in figure 1.5c, is made up of flat bilayers which are separated by water. The layers have the ability to slide over each other which gives the mixtures greater fluidity over other topological structures. At higher concentrations the bicontinuous phase may form (figure 1.5e), which is composed of aggregates making up a large and complex interconnecting 3D structure. This is considerably more viscous than the hexagonal phase and the lamellar phase due to the lack of shear planes.

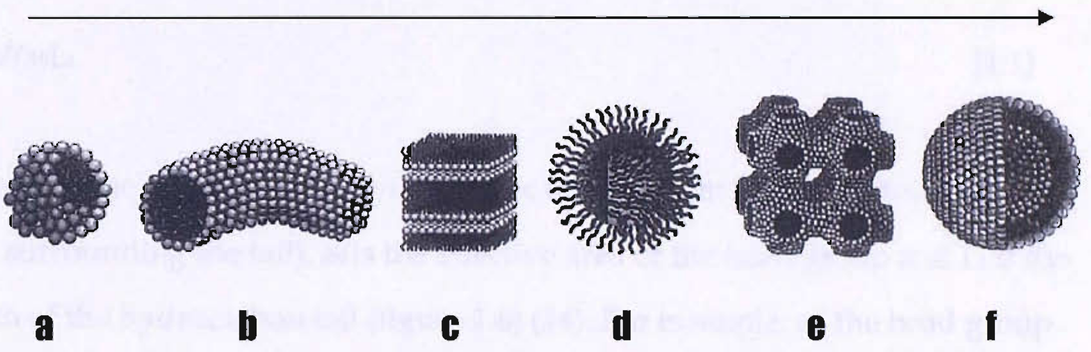

Figure 1.5: Various supramolecular building blocks of lyotropic liquid crystal micelles obtained by increasing the concentration of a surfactant in water: a). spherical, b).cylindrical c). planar bilayer, d). inverse micellar, e). bicontinuous and f). liposome. The arrow indicates increasing concentration of the surfactant in a solvent.

As well as the temperature and concentration constraints of liquid crystalline phases, the surfactant's molecular structure also defines the phase. Modification of the hydrophilic head groups or chain lengths (hydrophobic tails) will have a distinct effect over the lyotropic liquid crystal phase formed.

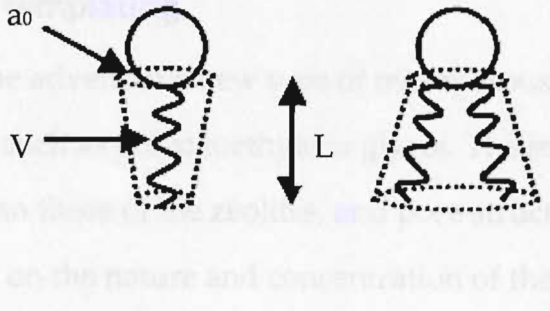

Figure 1.6: Schematic representation of a surfactant molecule adopting; a). the conical shape ('ice-cream cone') and the b). the inverse conical shape ('champagne cork').

The molecular structure of the micelle is determined by the forces of attraction and repulsion of the hydrophobic tail and the hydrophilic head groups. There are also steric interactions and ionic interactions to consider. In general, the structure of the surfactant aggregate is related to the geometric constraints of the ratio of the polar head group surface to the hydrophobic volume. The relationship between the molecular structure of the surfactant molecule, and its phase behaviour, the critical packing parameter (c) is given by equation 1.1:

$$c = V/a_0L_t \qquad [1.1]$$

where V is the volume of the hydrophobic tail area (nm^3) (within the dotted lines surrounding the tail), a_0 is the effective area of the head group and L_t is the length of the hydrocarbon tail (figure 1.6) (*14*). For example, as the head group (e.g. $C_{16}EO_{12}$ to $C_{16}EO_4$) becomes smaller as too does a_0, therefore the volume of the hydrophobic tail area increases by comparison. This reduces the tendency for the micelle to curve towards the hexagonal phase (H_I) and the generation of the lamellar phase (L_α) is preferred.

1.4. The synthesis of mesoporous materials using liquid crystalline template mixtures

1.4.1 Using MCM templating

The year 1992 saw the advent of a new type of mesoporous material fabricated by using surfactants such as polyoxoethylene glycol. The materials possessed pore sizes greater than those of the zeolites, and pore structures that could be modified depending on the nature and concentration of the surfactant template used in the lab. These materials were first fabricated by Beck *et. al.* and following this they went on to form a group of surfactant templated mesoporous amorphous silicas, called the M41S series (figure 1.7) (*18*). These silicas, with pore sizes in the range of 2-10 nm, were synthesized by using low surfactant concentrations (<30 wt.%) or copolymer molecules that create micellar arrays (*19, 20*). These surfactants can be employed as structuring agents in cooperative assembly processes between an organic surfactant and inorganic silica precursor species. This technique managed to meet demands for larger pore sizes in the mesoporous domain, allowing the accommodation of larger molecules in the pores.

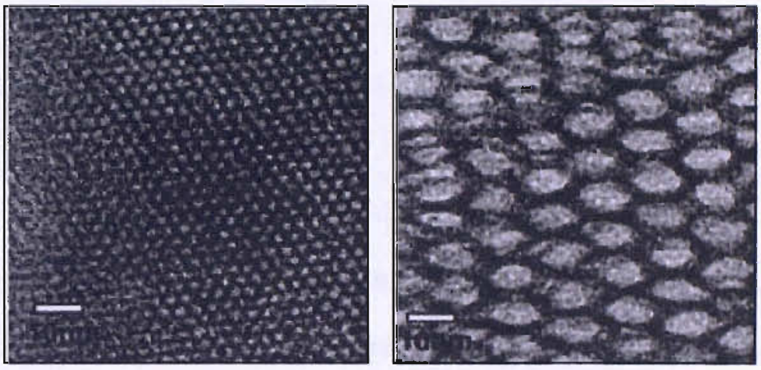

Figure:1.7: Transmission electron micrographs of MCM-41 materials with (a). 2 nm and (b). 10 nm pore channels. 2nm and 10nm are indicated by the scale bar in the bottom left corner of the images, respectively.

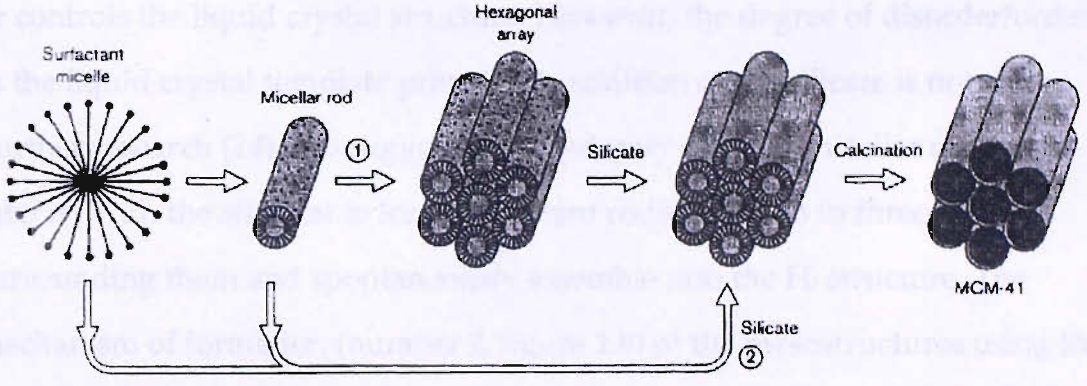

Figure 1.8: A reaction scheme showing the two route proposed by Beck *et. al*. for the fabrication of MCM-41, a hexagonal mesoporous silicas.

The M41S family consists of three structure types, MCM-41 (Mobil Corporation Material 41), containing a hexagonal arrangement of channels, MCM-48, with a complex interconnecting, 3-dimensional, channel system and finally MCM-50 consisting of a lamellar structure (*19, 21, 22*). It was subsequently shown that mesoporous metal oxides can also be obtained in this way using a range of surfactants. Materials fabricated via the MCM route have also been used as host materials for the loading of ruthenium cluster carbonyls thereby improving their catalytic properties. These materials can be tailor made with various pore sizes and wall thicknesses and even the incorporation of transition metals into MCM-41 materials or the partial exchange of silica for alumnina in M41S is possible. There have been two proposed routes (figure 1.8) (*16*). Mechanism 1 suggests that liquid crystals form a template structure before the addition of the silicate. While mechanism 2 suggests that the formation of the mesoporous structure occurs on the addition of the silicate. The silica precursor solution provides associative formation of the template structure while the liquid crystal silica influences the ordering. Initially, Mobil assumed the former mechanism. However, numerous sources of research have provided contradictory information. For example, according to ^{14}N NMR investigations by Chen *et. al*. (*23*), the liquid crystal's micellar structure was not present in the synthesis medium, providing further evidence that the silica species influences or controls the liquid crystal structure. However, the degree of disorder/order in the liquid crystal template prior to the addition of the silicate is not clear. Further research (*24*) also suggests the randomly ordered micellar cylinders, interact with the silicates to form surfactant rods with two to three layers surrounding them and spontaneously assemble into the H_I structure. The mechanism of formation (number 2, figure 1.8) of the mesostructures using the MCM mesoporous materials route was contradicted by work carried out by Attard *et. al* in 1995 (*1*). Attard reported that templating of silica mesostructures using the liquid crystalline mesophases, formed by non-ionic polyoxyethylene surfactants, required high concentrations of >30 wt.% and not <30 wt. % as reported by Beck. The templated silica phase contained pore diameters in the region of 3-10 nm, figure 1.9.

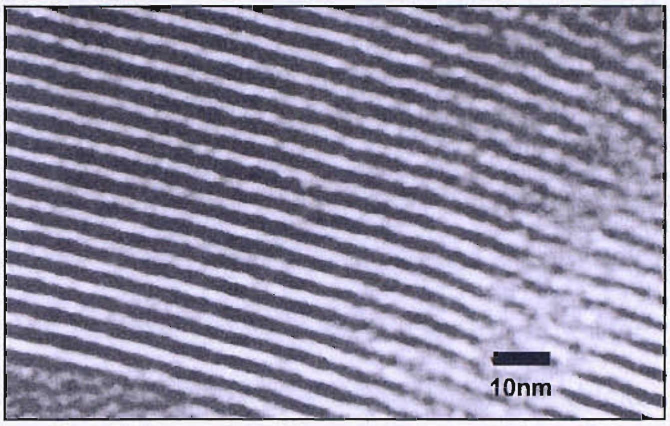

Figure 1.9: Transmission electron micrograph of calcined silica synthesised in the lamellar phase of $C_{16}EO_8$, scale bar 10 nm.

1.4.2 True Liquid Crystal Templating TLCT

Generating mesoporous materials using liquid crystalline template mixtures improved on the existing zeolitic structures. The True Liquid Crystal Template (TLCT) method employed the use of surfactants, similar to those used in the MCM templating of mesoporous silica, but at concentrations >30% (*1*). Surfactants like $C_{16}EO_8$ were first used to construct mesoporous silicates, using TMOS as the inorganic precursor, in the TCLT method. The preparation of a mesoporous silica directly from a liquid crystal phase involves the addition of tetramethylorthosilicate (TMOS) to a surfactant (> 50 wt%), water and acid mixture. Initially, a large amount of methanol is produced which destroys the liquid crystal phase, but removing the methanol under a gentle vacuum can regenerate the phase. After leaving the mixture to gel, the surfactant is removed by calcination. The aqueous domains of the surfactant phases determine the regions in which condensation of the silica network occurs. Consequently, the structure of the calcined silica is a cast of the supramolecular architecture of the liquid crystal phase.

The work carried out by Attard, Bartlett and Owen *et. al.* (*2, 4, 5, 25-34*) highlights the fact that the M41S route to mesoporous materials is reliant on the self assembly of micellar structures at low concentrations, whereas TLCT uses concentrations at much higher levels which are capable of reproducing predictable structures. The hydrothermal stability of the MCM-41 materials is poor in comparison to the true liquid crystal templating method. The MCM walls tend to be ~1 nm whereas TLCT walls tend to be thicker (3 nm) and give rise to more stable materials in hydrothermal conditions (*14*). Higher surfactant concentrations are more stable and allow greater control over the pore morphology to cover both normal and inverse phase templating. The MCM method can also be limited by headgroup-precursor interactions, where the surfactant and mineral species are opposite in the synthesis conditions (*35*). The direct method is not limited to inorganic oxides (i.e. silica), and it is possible to produce a wide variety of materials including polymers and metals, metal oxides and semiconductors.

1.4.3 Electrodeposition of mesoporous metals and semiconductors using TLCT

Following the pioneering work of Attard *et. al.*(*1*) the versatility of TLCT became apparent. Not only could the technique successfully predict the topology of the mesoporous product but it provided a route to the electrodeposition of mesoporous metals, such as platinum (*3*).

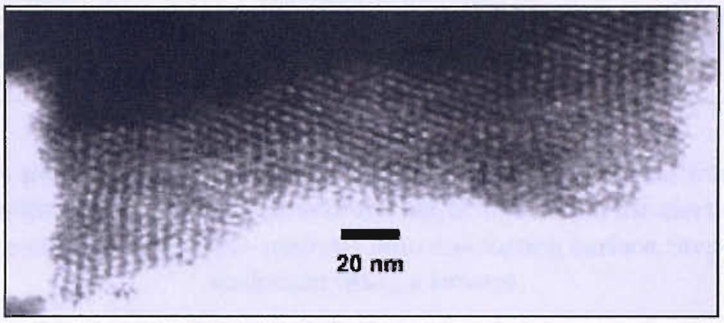

Figure 1.10: Transmission electron micrograph of a sample of H_I–eRh deposited from a mixture of 12 wt.% $RhCl_3$, 47 wt.% $C_{16}EO_8$, 2 wt.% heptane and 39 wt.% water.

This became a generic method for fabricating a wide range of mesoporous materials such as nickel (*34*), tin (*28*) and rhodium (*36*). A TEM micrograph of mesoporous rhodium is shown in figure 1.10. The image shows the structure of a mesoporous ruthenium film. The pores are shown end-on with a diameter of about 3.5 nm and a 6 nm pore to pore centre distance.

Another major advantage of the direct templating strategy is that it can afford the fabrication of thin metallic films with long range periodic and uniform nano-architectures via electrodeposition. The use of electrodeposition means that this is also a cost effective, versatile fabrication method with the potential to be scaled up and adapted to industrial processes. The preparation of a wide range of elements such as palladium (*33*), platinum (*5*), tin (*28*), and cobalt (*2*), but also nickel oxides (*37*) and alloys (*29*) has already been achieved. Figure 1.10 illustrates the principle of this templated approach to nanostructured films. A metal salt precursor solution (~50 wt.%) is mixed with a non-ionic surfactant (~50 wt.%) to prepare the liquid crystalline template electrolyte.

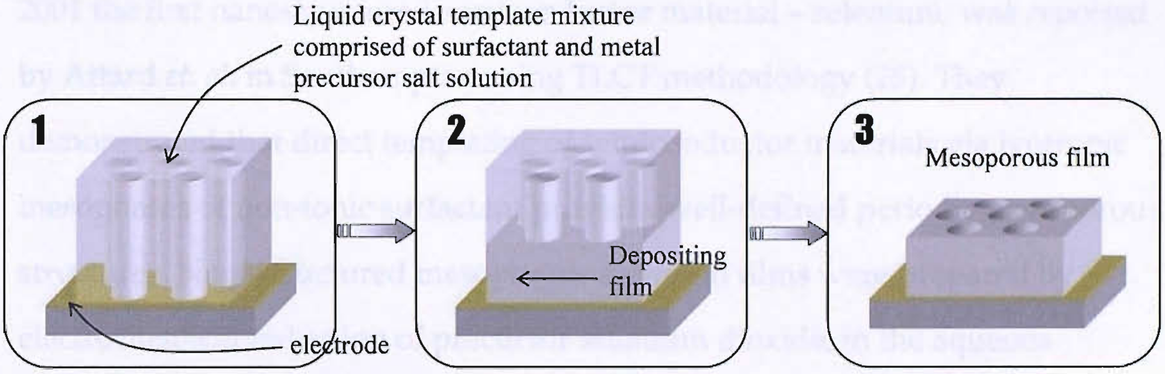

Figure 1.11 A simplified schematic of the three step process of the electrodeposition of mesoporous thin films. Step 1: Preparation of the liquid crystal and the electrodeposition cell. Step 2 electrodeposition of conductive material onto conducting surface. Step 3: removal of the surfactant using a solvent.

In the case of a hexagonal phase, the metal ions reside around the hexagonally arranged cylindrical surfactant micelles (figure 1.11, step 1). Using a three electrode cell, comprised of a reference, counter and working electrode, application of an electrode potential allowed electrodeposition of the metal on the electrode surface. A potential difference is then applied between the reference electrode and the working electrode. The counter electrode carries the current. This creates the transport of metal ions through the liquid crystal phase (figure 1.11, step 2). After deposition and surfactant removal the film is a direct cast of the lyotropic liquid crystalline phase (figure 1.11, step 3). TEM is extensively and successfully used to visualise dimensions in the mesoporous range and although a reliable tool for the analysis of the pore sizes, preparing the films by electrodeposition on substrates causes problems. Preparation of the nanostructured films for TEM analysis requires the films to be scraped on to the TEM grid. Using this method is unreliable as the position of the sample on the transmission electron microscope grid may not always reveal the pores. An example of the observed porous structure is visible in figure 1.11.

The electrodeposition of mesoporous metals was further developed, and by 2001 the first nanostructured semiconductor material – selenium, was reported by Attard *et. al.* in Southampton using TLCT methodology (25). They demonstrated that direct templating of semiconductor materials via lyotropic mesophases of non-ionic surfactant provides well-defined periodic mesoporous structures. Nanostructured mesoporous selenium films were prepared by electrochemical reduction of precursor selenium dioxide, in the aqueous domains of a hexagonal lyotropic phase of $C_{16}EO_8$. This method disregards the use of co-adjuvants (i.e. substance which affects the size of the mesophase head-group) and calcination processes and relies solely on electrodeposition as a method to build the nanostructured material. The result was hexagonally nanostructured mesoporous films of extended spatial periodicities with high surface areas and uniform pore structures. TEM studies of the selenium films revealed the presence of a system of closely packed hexagonal shaped structures, with a pore wall thickness at the point of contact between neighbouring pores was 2.5 ± 0.2 nm, figure 1.12. The lighter coloured circular

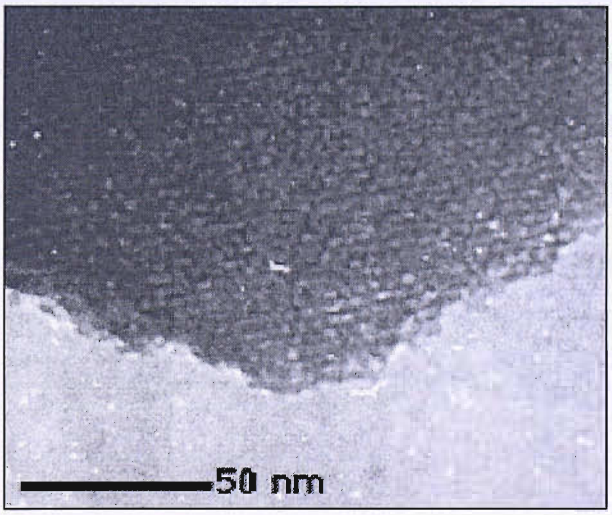

Figure 1.12: Transmission electron micrographs of selenium electrodeposited from the hexagonal liquid crystalline phase of $C_{16}EO_8$ at 65 °C onto a 1 cm^2 nickel sheet electrode.

regions, in figure 1.12, correspond to the pores after removal of the surfactant, whereas dark regions correspond to the selenium pore walls (*25*). The electrodeposition of mesoporous semiconductors from the domains of a liquid crystal mixture requires different conditions to the electrodeposition of non-mesoporous semiconductor materials. This is due to the experimental constraints imposed by the liquid crystalline mesophases. For example, the deposition of mesoporous semiconducting selenium from liquid crystalline plating mixtures requires significant modifications of the electrochemical deposition conditions used in the isotropic aqueous system. A temperature of 100°C and a saturated SeO_2 in 9 M H_2SO_4 solution is used to prepare the non-mesoporous film, however when preparing the mesoporous film the deposition temperature is limited to 55-65 °C due to the lack of liquid crystal structure at higher temperatures. The deposition potential and the composition and concentration of components (10 mM SeO_2 and 2 M) (*25*) must also be significantly different. Temperature, pH, and also the effect on the viscosity and mobility of the ions in the mixture must be taken into consideration. Following this H_I-eZnO has also been prepared by Choi *et. al.* using less pure surfactant mixtures such as Brij®56 (*38*).

The mesoporous semi-metal and semiconductor films are of considerable interest due to their potential use in technological applications, such as enhanced solar cells, ultra sensitive chemical sensors and improved photocatalysis. The following chapters provide the initial steps in producing these materials in a reproducible, low cost, straightforward manner.

1.5. References

1. G. S. Attard, J. C. Glyde, C. G. Goltner, *Nature* **378**, 366 (1995).
2. N. B. Bartlett, P. N. Birkin, A. M. Ganhem, P. de Groot, M. Sawicki, *Journal of the Electrochemical Society* **148**, C119 (2001).
3. G. S. Attard, P. N. Bartlett, N. R. B. Coleman, J. M. Elliot, J. R. Owen, J. H. Wang., *Science* **278**, 838 (1997).
4. A. H. Whitehead, J. M. Elliot, J. R. Owen, *Journal of Power Sources* **81-82**, 33 (1999).
5. G. S. Attard, C. G. Goltner, J. M. Corker, S. Henke, R. H. Templer, *Angew. Chem. Int. Ed. Engl.* **36**, 1315 (1997).
6. A. Lasia, *Journal of Electroanalytical Chemistry* **397**, 27 (1995).
7. H. Arizpe-Chavez, R. Ramirez-Bon, F. J. Espinoza-Beltran, O. Zelaya-Angel, J. L. Martin, R. Riera, *Journal of Physics and Chemistry of Solids* **61**, 511 (2000).
8. P. N. Cheremisinoff, F. Ellerbusch, *Carbon Adsorption Handbook* (1978), pp. 14-17
9. M. Born, E. Wolf, *Principles of Optics* (Pergamon Press, ed. 2nd, 1964), pp. 51.
10. P. N. Cheremisinoff, F. Ellerbusch, *Carbon Adsorption Handbook* (1978), pp. 5.
11. A. Linares-Solano, *Carbon and coal gasification.* F. J. A. Moulijjn, Eds. (Marinus Nijhoff publishers: Dordenct, 1986), pp.
12. T. Gabriel, Undergraduate Final Year Report, University of Newcastle-upon-Tyne (2000).
13. R. A. Rakoczy, Y. Traa, *Microporous Mesoporous Materials,* 69 (2003).
14. A. A. Soler-Illia, C. Sanchez, B. Lebeau, J. Patarin, *Chemical Review* **102**, 4093 (2002).
15. I. W. Hamley, *Introduction to soft matter polymers, colloids, amphiphiles and liquid crystals* (Wiley, 2000), pp. 134-147.
16. M. E. Raimondi, J. M. Seddon, *Liquid Crystals* **26**, 305 (1999).
17. D. F. Evans, H. Wennerstrom, *The Colloidal Domain Where Physics, Chemistry, Biology and Technology Meet* (Weinheim,, 1994), pp. 51
18. J. S. Beck, J. C. Vartuli, *Curr. opin. solid State mater. Sci* **1**, 76 (1996).
19. C. T. Kresge, M. E. Leonowicz, *Nature* **359**, 710 (1992).
20. J. S. Beck, J. C. Vartuli, W. J. Roth, M. E. Leonowicz, C. T. Kresege, K. D. Schmitt, C. T. W. Chu, D. H. Olson, E. W. Sheppard, S. B. McCullen, J. B. Higgins, J. L. Schlenker, *Journal of the American Chemical Society* **114**, 110834 (1992).
21. J. S. Beck, J. C. Vartuli, J. G. Kennedy, *Chemical Materials* **6**, 1816 (1994).

22. J. C. Vartuli, K. D. Schmitt, C. T. Kresege, *Chemical Materials* **6**, 2317 (1994).
23. C. Y. Chen, S. L. Burkett, H. X. Li, M. E. Davis, *Microporous Materials* **2**, 27 (1993).
24. J. Marwan, PhD, University of Southampton (2002).
25. I. Nandhakumar, J. M. Elliot, G. S. Attard, *Chemical Materials* **13**, 3840 (2001).
26. N. R. B. Coleman, PhD, Southampton University (1997).
27. J. M. Elliot, G. S. Attard,P. N. Bartlett, N. R. B. Coleman, A. S. Merckel, J. R. Owen, *Chemistry of Materials* **11**, 3602 (1999).
28. A. H. Whitehead, J. M. Elliot, J. R. Owen, G. S. Attard, *Chemical Communications*, 331 (1999).
29. G. S. Attard, S. A. A. Leclerc, S. Maniguet, A. E. Russell, I. Nandhakumar, R. B. Gollas, P. N. Bartlett, *Microporous and Mesoporous Materials* **44-45**, 159 (2001).
30. M. Ganhem, PhD, Southampton University (2001).
31. T. Gabriel, I. S. Nandhakumar, G. S. Attard, *Electrochemical Communications* **4**, 610 (2002).
32. I. S. Nandhakumar, T. Gabriel, M. M. Markham, D. C. Smith, J. J. Baumberg, G. S. Attard, *Chemical Communications* **12**, 1374 (2004).
33. P. N. Bartlett, B. Gollas, S. Guerin, J. Marwan, Physical Chemistry Chemical Physics, **4**, 3835 (2002).
34. P. A. Nelson, J. M. Elliot, G. S. Attard, J. R. Owen, *Chemistry of Materials* **14**, 524 (2002).
35. Q. Huo, D. I. Margolese, U. Ciesla, P. Feng, T. E. Gier, P. Sieger, R. Leon, P. M. Petroff, F. Schuth, G. D. Stucky, *Nature* **368**, 317 (1994).
36. N. B. Bartlett, J. Marwan, *Microporous and Mesoporous Materials* **62**, 73 (2003).
37. H. Luo, J. Zhang, Y. Yan, *Chemistry of Materials* **15**, 3769 (2003).
38. K. Choi, H. C. Lichtenegger, G. D. Stucky, *Journal of the American Chemical Socitey* **124**, 12402 (2002).

CHAPTER TWO:

EXPERIMENTAL PROCEDURES

In this chapter the experimental techniques required to carry out research into the fabrication and characterisation of mesoporous semiconductor materials are presented. Included are descriptions of the materials used, the fabrication of template mixtures, details of the optical birefringence apparatus and measurement techniques.

2.1 Chemicals and Materials

All chemicals were of analytical grade and used as obtained without further purification. The surfactants used throughout this work were Brij®78 ($C_{18}EO_{20}$, polyoxyethylene(20) stearyl ether) and Brij®56 ($C_{16}EO_{10}$, polyoxyethylene(10) cetyl ether) available from Aldrich and Fluka respectively, and $C_{16}EO_8$ (Octaethylene glycol monohexadecyl ether) available from Jan Dekker International.

The deposition of semi-metals and semiconductors from both aqueous and liquid crystalline phases were prepared by using the following solutions;

2.1.1 Electrodeposition of Tellurium

Tellurium dioxide (TeO_2, 99.9995%), and sulfuric acid (H_2SO_4, 99.999%), obtained from Aldrich, were stirred together with gentle warming.

2.1.2 Electrodeposition of Cadmium Telluride

Cadmium sulfate ($CdSO_4$, 99.999%), cadmium acetate ($Cd(OAc)_2$, 99.99+%), cadmium perchlorate ($Cd(ClO_4)_2$, 99,999%), cadmium nitrate ($Cd(NO_3)_2$ 99.999%), sulfuric acid (H_2SO_4, 99.999%) and citric acid (99.999%) were used. To prepare cadmium telluride the tellurium solution from 2.1.1 is added to a solution containing cadmium sulphate and high purity water.

2.1.3 Electrodeposition of Zinc Oxide

Zinc nitrate hydrate ($Zn(NO_3)_2$, 99.999%), zinc chloride ($ZnCl_2$, 99.999%), zinc perchlorate hexahydrate ($Li(ClO_4)_2$) were all obtained from Aldrich. Solutions were prepared by dissolving in water while stirring.

Glacial acetic acid analar grade (CH_3COOH, 99.99+%) and potassium hydroxide (KOH, 99%) were obtained from BDH. All aqueous solutions and liquid crystal templates were prepared using high purity water from an Elgar purification system with a resistivity of 18 MΩ cm^{-1}. All glassware used was left to soak overnight in a water/Decon (3%) solution and rinsed thoroughly with purified water.

Gold electrode substrates were prepared by initially evaporating 25 nm of a chromium adhesive underlayer (for better adhesion of a gold layer) which was followed by a 250 nm layer of evaporated gold (Agar, 99.99%), on a 1 mm thick microscope slide. The gold electrodes were cleaned by soaking in isopropanol for at least 24 hours and subsequent sonification for 10 minutes in isopropanol. Cadmium sulfide films on tin oxide coated glass substrates ($CdS|SnO_2|glass$) were also used as electrodes. These were prepared by chemical bath deposition, and were supplied by BP Solar and Paul O'Brian's group (Manchester University). Indium tin oxide substrates were supplied by Delta technologies.

2.2 Liquid crystal template preparation

The precursor salt solution is prepared by dissolving the desired metal compound (TeO_2, $CdSO_4$ see solution mixtures in section 2.1) in 2 M sulfuric acid followed by addition of citric acid to allow deposition on $CdS|SnO_2|glass$

substrates. Ternary and quaternary templating mixtures were prepared using the required wt.% of surfactant and precursor salt solution. The metal precursor salt solution, surfactant and stirrer bar were then added to a glass vial or screw lid jar. The mixture was heated to its melting point (which is dependant on the components of template mixture) on a hotplate/stirrer, and then stirred vigorously for 10 minutes. Removal from the hotplate allowed the mixture to cool forming a translucent viscous gel. Finally the mixture was then left overnight in order to fully homogenise before any optical characterisation and electrodeposition.

In all cases the texture, and therefore the phase of the liquid crystal template mixture was verified by polarised optical microscopy (POM). The microscope, an Olympus BH2 polarised light microscope was equipped with a Linkam TMS90 heating/cooling stage and temperature control unit. The temperature could be maintained to within ± 0.1 °C of the set temperature during the experiments. The analysis of the mixtures required the preparation of a thin film of the mixture sandwiched between a coverslip and a glass slide. Phase diagrams of the templating media, in the composition range of 30-90 wt. % of surfactant at temperatures between 20 to 80 °C, were investigated. The individual phases were identified on the basis of their optical texture, viscosity and the shape of any air bubbles. Angular air bubbles signify the presence of highly structuredphase such as the hexagonal.

2.3 Electrochemical instrumentation and cell preparation

Electrodeposition of the mesoporous film was carried out using a μAutolab type II potentiostat. Electrodeposition was carried out potentiostatically using a three-electrode cell. Gold, CdS coated tin oxide and indium tin oxide substrates were used as the working electrode with an area of ~2 cm^2, a large area (~2 cm^2). The edges of the electrodes were taped off using polyimide tape. A platinum wire gauze and a home made saturated calomel electrode (SCE) were used as the counter electrode and reference electrode, respectively. The SCE was calibrated against a commercial SCE. Potentials are reported with respect to a saturated calomel electrode (the SCE is -0.247 V *vs.* NHE) or a cadmium ion/cadmium reference electrode (-0.429 V *vs.* NHE), which was comprised of a cadmium wire immersed in a 0.5 M $CdSO_4$ solution and separated from the deposition solution by a glass frit. Small differences in the measured voltages were tolerated for these experiments (<5 mV). The SCE reference electrodes were stored in saturated potassium chloride solutions and rinsed with de-ionised water before use, while the cadmium electrode was stored in a 0.5 M cadmium sulphate solution.

The electrodeposition temperature was dependant on the desired semiconductor film and the surfactant phase stability, and ranged from ambient to 85 °C. The cell set-up, used for ambient temperature conditions, can be seen in Figure 2.1a, and a schematic of the cell is shown in figure 2.1b. (The Viton seal was used to hold the liquid crystal template in place on the gold surface).

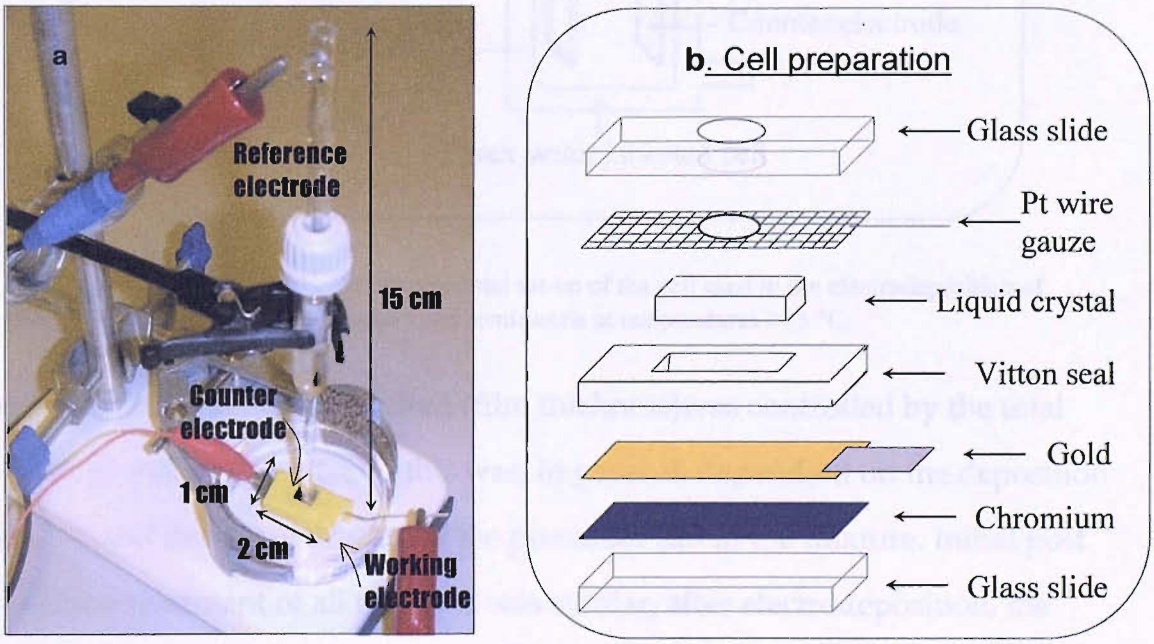

Figure 2.1: a). Photograph of the electrochemical set-up for the deposition of mesoporous materials. b). diagram of the construction of n electrodeposition cell using a liquid crystal template mixture.

In cases where elevated deposition tempertures were used, the temperature was controlled by the use of a water-jacketed Pyrex cell. A rubber bung was placed at the top of the cell to prevent water loss and therefore subsequent loss of the hexagonal phase . The cell set-up is shown in figure 2.2a. The cell temperature was maintained to an accuracy of 0.1 °C throughout with the use of a water bath. After setting up the cell (figures 2.1a-c), the liquid crystal electrolyte mixture was heated above the isotropisation temperature (of the desired phase) for approximately 20 minutes. The mixture was then allowed to cool, without assistance, to 10 °C below the isotropisation temperature for reformation of the phase. The cell temperature was then set to the required deposition temperature.

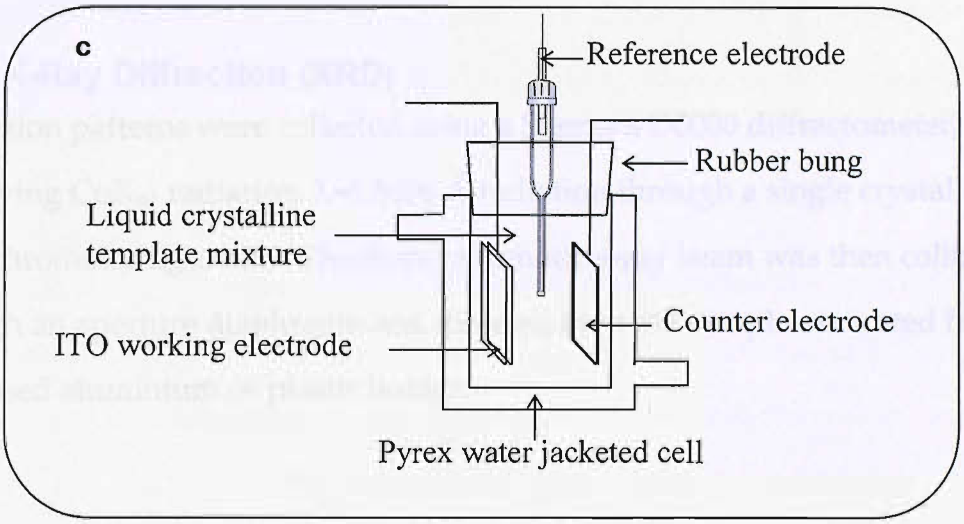

Figure 2.1c: Diagram of the experimental set-up of the cell used in the electrodeposition of semiconductors and semimetals at temperatures >25 °C.

The amount of material deposited (film thickness)was controlled by the total amount of charge passed, and this was, in general, dependant on the deposition duration and the concentration of the precursor salt in the mixture. Initial post deposition treatment of all the films was similar; after electrodeposition, the surfactant on the substrate was removed by extensive rinsing with deionised water, followed by placing it in isopropanol overnight whilst being stirred.

2.4 Characterisation and analysis of liquid crystal templates and their electrodeposited films

Experimental observations of the organisation of the micellar phases show that they are sensitive towards internal variations such as hydrophobic structure and head group, and external factors including pH, temperature, pressure and the electrolyte composition.

The following sections describe the characterisation of liquid crystal templates and their films using various tecniques such as X-ray diffraction (XRD), polarised optical microscopy (POM), scanning electron microscopy (SEM) and transmission electron microscopy (TEM).

2.4.1 X-Ray Diffraction (XRD)

Diffraction patterns were collected using a Siemens D5000 diffractometer, employing $CuK_{\alpha 1}$ radiation, λ=1.5406 Å radiation through a single crystal monochromator figure 2.2. The monochromatic x-ray beam was then collimated through an aperture diaphragm and directed onto the sample, mounted flush in a recessed aluminium or plastic holder.

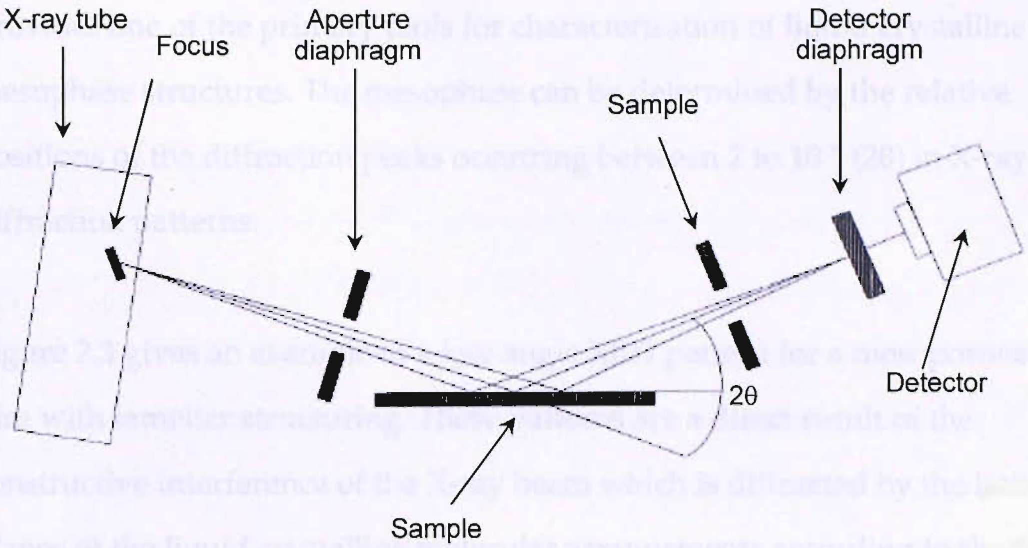

Figure 2.2: A Schematic representation of the Siemens D5000 diffractometer.

X-Rays diffracted from the sample were detected by a standard scintillation counter. The sample goniometer was rotated at a constant angular velocity and the detector moved at twice this velocity to ensure the diffraction angle, 2θ.

2.4.1.1 Low-angle X-ray diffraction (XRD)

Low angle X-ray diffraction was carried out using the same Siemens D5000. Although not designed to carry out low angle work it provided colloborative evidence for the identification of mesoporous structures in the template mixture and film. For low angle XRD measurements were taken over the range ~1-5 (2θ) degrees and at a scan rate of 6 degrees min^{-1} for 1 hour.

Characterisation of mesophases is routinely carried out by low angle XRD and provides one of the primary tools for characterisation of liquid crystalline mesophase structures. The mesophase can be determined by the relative positions of the diffraction peaks occurring between 2 to 10 ° (2θ) in X-ray diffraction patterns.

Figure 2.3 gives an example of a low angle XRD pattern for a mesoporous silica film with lamellar structuring. These patterns are a direct result of the constructive interference of the X-ray beam which is diffracted by the lattice planes of the liquid crystalline molecular arrangements according to the Bragg equation (equation 2.1):

$$n\lambda = 2d\sin\theta \qquad [2.1]$$

where d is the lattice spacing, λ is the wavelength, n is the order of the diffraction peak, and θ is the angle between the incident and scattered beams. XRD data can also provide information on the repeat distance between pores by

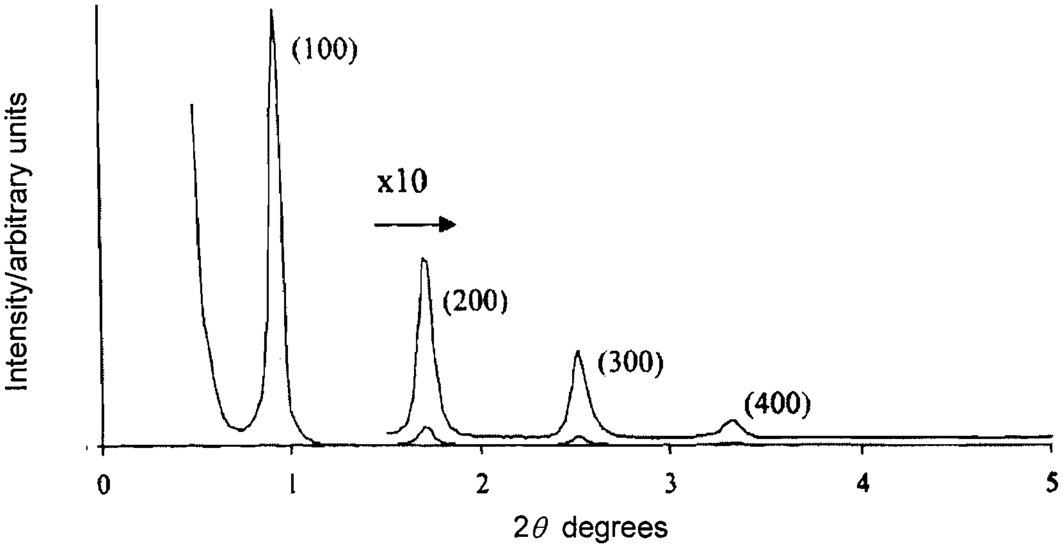

Figure 2.3: 1D X-ray diffraction pattern of calcined silica film approximately 200-500 nm thickness with lamellar mesostructural ordering .

applying equation 2.2:

$$d_{100} / \cos 30^\circ \qquad [2.2]$$

Further information can also be ascertained from x-ray diffraction data. A small (full-width at half-height maximum FWHM of peak) FWHM and the presence of higher order diffraction peaks is normally an indication for a well ordered film with longer range periodicity of the material. Another indication of high ordering within a film is the number of higher order diffraction peaks observed in the pattern.

The ratio of the reciprocal d-*spacings* of the diffraction lines permits identification of the mesoporous structure or phase and the indexing to a particular symmetry. Table 2.1 shows the low angle X-ray diffraction patterns characterised by the peaks corresponding to the diffraction planes and their

	space group	hkl list	spacing ratio
Hexagonal Phase	P6mm	100	1
		110	√3
		200	2
		210	√7
Lamellar		100	1
		200	2
		300	3
Cubic	Ia3d(230)	110	√2
		200	2
		211	√6
		220	√8
		310	√10
		222	√12

Table 2.1: Selection rules for the space groups associated with the liquid crystal phases and the relative spacings of the first Bragg reflections. Only the most common found cubic phases in lyotropic systems are shown. The information is obtained form the international tables of crystallography.

relative reciprocal d-*spacings*. For example, when mixed with water $C_{16}EO_8$ can exist as several different phases that can be identified by low angle XRD and the observed peaks and the relative d-spacing. Four peaks (<100>, <110>, <200>, <210>) in the ratio of $1:\sqrt{3}:2:\sqrt{7}$ are observed for the hexagonal phase of a surfactant in water, whereas the cubic Ia3d(230) phase may reveal up to 6 peaks (<110>, <200> , <211> etc.) with the reciprocal d-*spacings* of $\sqrt{2}$, 2, $\sqrt{6}$ etc.. Figure 2.3 shows the ratio for a lamellar mesostructured silica film with the peak positions in the ratio of 1:2:3. One must note that ionic doping of liquid crystalline materials can also cause the collapse of the higher order diffraction peaks, this is assumed to be a result of the ionic interactions with the surfactant molecules. This will be addressed in greater detail in section 3.2. Also when using this technique to identify mesoporous electrodeposited materials, only the first order diffraction peak is observed (*1-3*). This is caused by the lack of long range ordering exhibited by the material.

2.4.1.2 Wide angle X-ray diffraction (XRD)

Wide XRD was used to determine the crystal structure and the structural chemical identity of the electrodeposited mesoporous tellurium, cadmium telluride and zinc oxide films. Comparisons were then made with literature results for their bulk counterparts. XRD measurements were also taken for the electrode surfaces as a reference. Wide angle X-ray diffractograms were recorded over a suitable range (usually 10-80 (2θ) degrees) for an overnight period.

2.4.2 Polarised optical microscopy (POM)

Polarised optical microscopy (POM) is used to identify the phases of liquid crystalline mixtures formed by surfactants. POM is a technique that uses crossed polarised filters and an optical microscope to examine a materials ability to change the plane of polarised light. Light cannot pass through the crossed polarised filters, therefore the optical image appears black. If a sample of a liquid crystalline mixture such as Brij®56 and water is placed between a glass slide and a cover slip, and then placed in between the filters, images such as those in figure 2.4 may be observed.

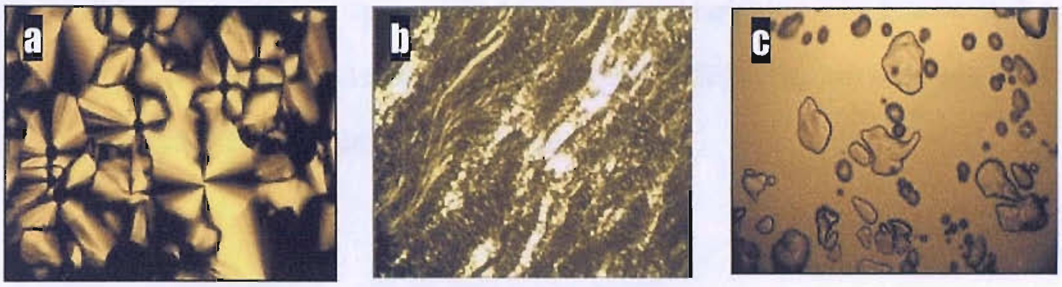

Figure 2.4: The hexagonal (a), lamellar (b) and cubic (c) lyotropic liquid crystalline phases of $C_{16}EO_8$, observed using polarised optical microscopy (POM).

Liquid crystals have the ability to alter the plane of polarised light, thus allowing light to pass through the polarisers. When a liquid crystal phase possesses two different refractive indices, at 90° to one another, they are described as birefringent or optically anisotropic. Liquid crystals phases such as the hexagonal and lamellar phases figure 2.4a and b, respectively, are birefringent, but cubic phases are non-birefringent, figure 2.4c. Figure 2.4a is the hexagonal phase and the result observed for a liquid crystal sandwiched between a coverslip and a microscope slide. The example shows 50wt.% $C_{16}EO_8$ and 50wt.% water when homogenously mixed and view under the microcope rosettes are observed. Figure 2.4b shows the texture of the lamellar phase which has a non-uniform director. This sweeping mosaic effect is typical for the lamellar phase.

In the cubic structure the molecules are very much orientated in positions along all three axis, whereas the lamellar and hexagonal only represent 1D and 2D geometries respectively. For a material to be birefringent it must posses a molecular director in either one or two dimensions. The hexagonal phase is two dimensional and lamellar is 1D.

The optical texture which is observed in POM depends on both the phase structure and the nature of the defects within it (defects result in scattering of light which is anisotropic). In practice, identification by POM also relies on the verification of phase viscosity and the shape of any bubbles. For example the hexagonal phase is viscous with angular bubbles, while the lamellar phase is less so as the flat bilayers can slide over each other.

2.4.3 Liquid crystal phase diagrams

Liquid crystalline phases can be identified using XRD and POM. Figure 2.4a showed that POM can indicate the phase by its optical texture e.g. hexagonal phases display a rosette/fanlike birefringent pattern, its viscosity and the shape of any bubbles present. The mesophase can be further confirmed by the corresponding Bragg reflections in the low angle XRD patterns (figure 2.3), e.g. hexagonal mesophase with a *d*-spacing ratios of $1{:}\sqrt{3}{:}\ 2$. A phase diagram can be constructed on the basis of XRD and POM data identifying the relevant attributes of each phase. Figure 2.5 shows the binary phase diagram for $C_{16}EO_8$ with water.

On heating and cooling the surfactant template mixtures POM can indicate, by a change in the optical texture of the phase, the temperature at which the phase ceases to exist, or becomes a different phase. This is known as the isotropisation temperature. In the case of the hexagonal to lamellar phase transition for 50 wt.% $C_{16}EO_8$, the template mixture undergoes a change from a feathery optical texture to a black, featureless optical texture at approximately 57 °C when observed by POM.

The diagram describes the compositional and temperature regions where liquid crystal phases, such as H_I, V_I, I_I and L_α can exist as stable phases. For instance, the cubic phase exists in several forms, one of which is the I_I phase, which consists of micelles packed on a body-centred cubic lattice, with a very viscous texture (figure 2.5). The lamellar phase (L_α) is made up of flat bilayers which are separated by water. The diagram depicts the domains of separated phases such as L_I + W (water). These mixed phases are reached at a boundary called the cloud point, where the mixture becomes rich in micelles surrounded by the solvent (H_2O), denoted by W + L_I.

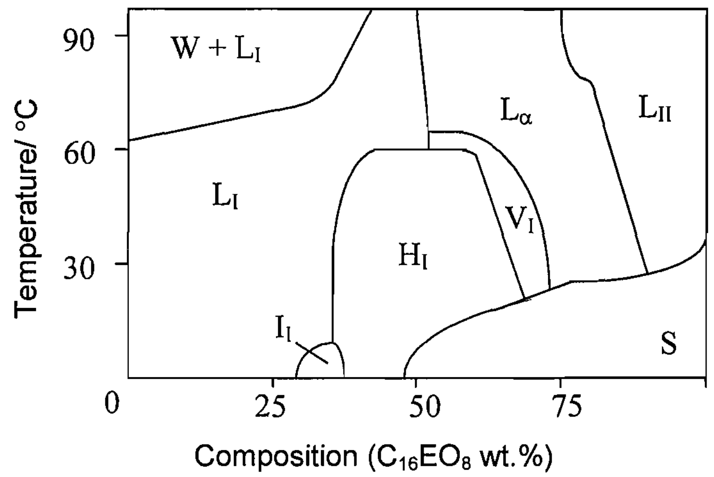

Figure 2.5: Phase diagrams showing phase boundaries for $C_{16}EO_8$ in water at various concentrations and temperatures. Phases: W – water, L_I – micellar, H_I – hexagonal, I_I – cubic micellar, L_I – micellar, V_I – cubic bicontinuous, L_{II} – inverse lamellar, S – solid. (4)

2.4.4 Transmission electron microscopy (TEM)

Structural characterisation and confirmation of the deposited film's nanostructure was carried by *transmission electron microscopy*. TEM micrographs were obtained using a JEOL 2000FX Transmission Electron Microscope. An electron beam formed by a gun, accelerates electrons produced from a filament operating at a voltage of 200 kV. Focusing and magnification is achieved by using a series of electromagnetic lenses. The electron beam is focused onto the sample using condenser lenses and magnification of the transmitted image is carried out with an objective and projector lenses. Figure 2.6 shows a diagram of a transmission electron microscope

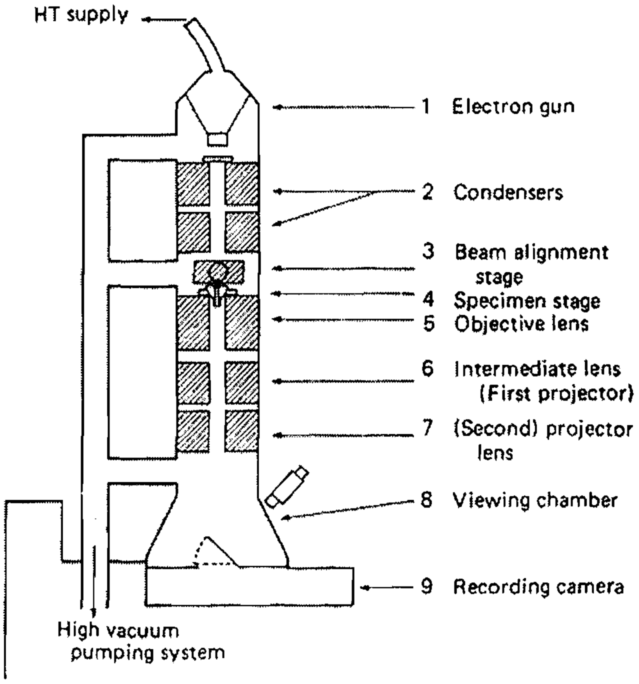

Figure 2.6: Schematic of a transmission electron microscope

For TEM characterization films were initially dried overnight (under ambient conditions, in a covered container). Then a drop of water was placed onto the TEM supporting grid. (a circular, 3.05 mm, 400 mesh carbon-coated copper grid, Agar Scientific Ltd). The film was scraped off with a scalpel onto the droplet of water. The grids were dried by placing them in an oven for two hours.

2.4.5 Scanning Electron Microscopy (SEM)

Images of the films microstructure were obtained using a Philips EL30 ESEM scanning electron microscope (SEM). A filament creates an electron beam which is then accelerated to an operating voltage of between 20-30 kV. The electron beam is focussed onto the mesoporous film. The secondary electrons are detected allowing imaging of the surface. Electron dispersive X-ray can also be carried out.

All samples were prepared by sticking them onto an aluminium stub using double sided carbon tape. Films prepared for cross-sectional scanning electron microscopy analysis were cut, using a diamond glass cutter, and imaged at a cross section to the cleavage plane in order to reveal the thickness of the electrodeposited film. The SEM was also equipped with an energy dispersive X-Ray (EDX) unit for studying the chemical composition of the deposited films.

2.5 Optical measurements

2.5.1 Birefringence observed by POM

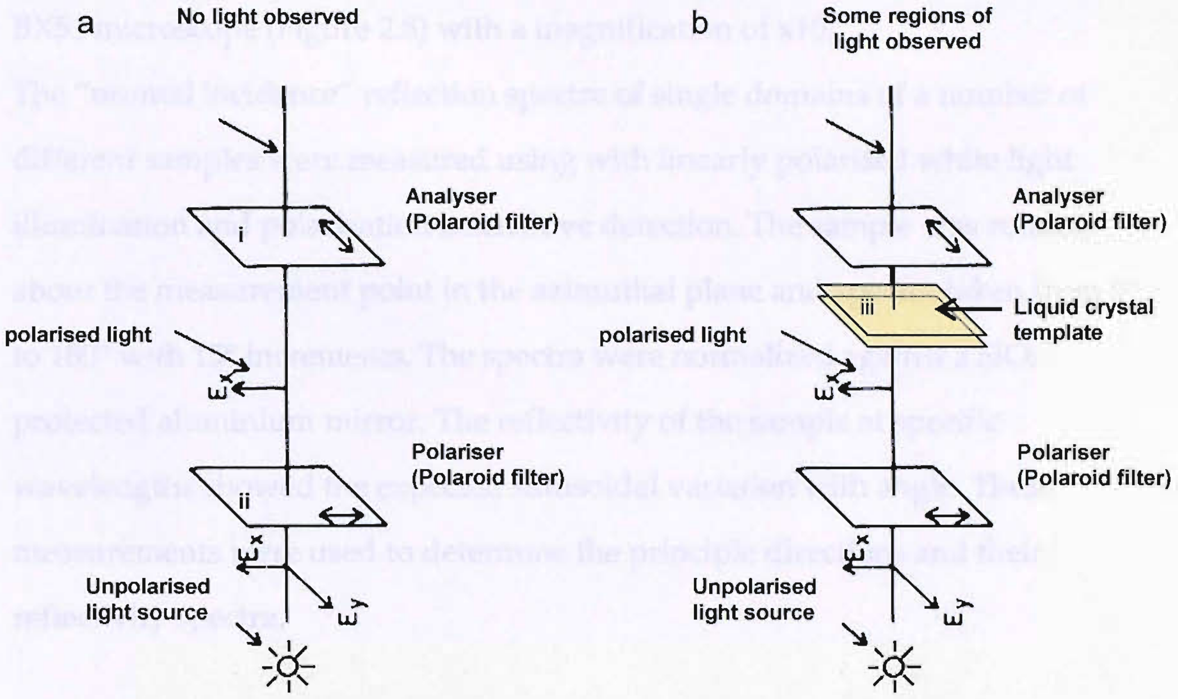

Figure 2.7: Schematic diagram of the positioning of polaroid filters in a polarised light microscope. i). Analyser: polaroid filter, ii). Polariser: polaroid filter, iii). Liquid crystal sample sandwiched between a glass slide (below) and a coverslip.

The polarised light microscope has a pair of crossed polaroid filters. The analyser (figure 2.7ai) is situated above the sample, while the polariser (figure 2.7aii) is positioned below. A source of unpolarised light is shone from below producing a completely black image when viewed from the analyser. Placing a liquid crystal template mixture sandwiched between two glass plates (figure 2.7biii), allows some rotation of the polarised light, and after passing through the analyser light and dark regions are observed.

2.5.2 Birefringence measurements: micro-spectroscopy

Investigation of the optical properties was performed by M. L. Markham in the University of Southampton School of Physics and Astronomy. Polarised optical microscope images of the mesoporous films were recorded using an Olympus BX51 microscope (Figure 2.8) with a magnification of x10.

The "normal incidence" reflection spectra of single domains of a number of different samples were measured using with linearly polarised white light illumination and polarisation insensitive detection. The sample was rotated about the measurement point in the azimuthal plane and spectra taken from 0° to 180° with 15° increments. The spectra were normalized against a SiO_2 protected aluminium mirror. The reflectivity of the sample at specific wavelengths showed the expected sinusoidal variation with angle. These measurements were used to determine the principle directions and their reflectivity spectra.

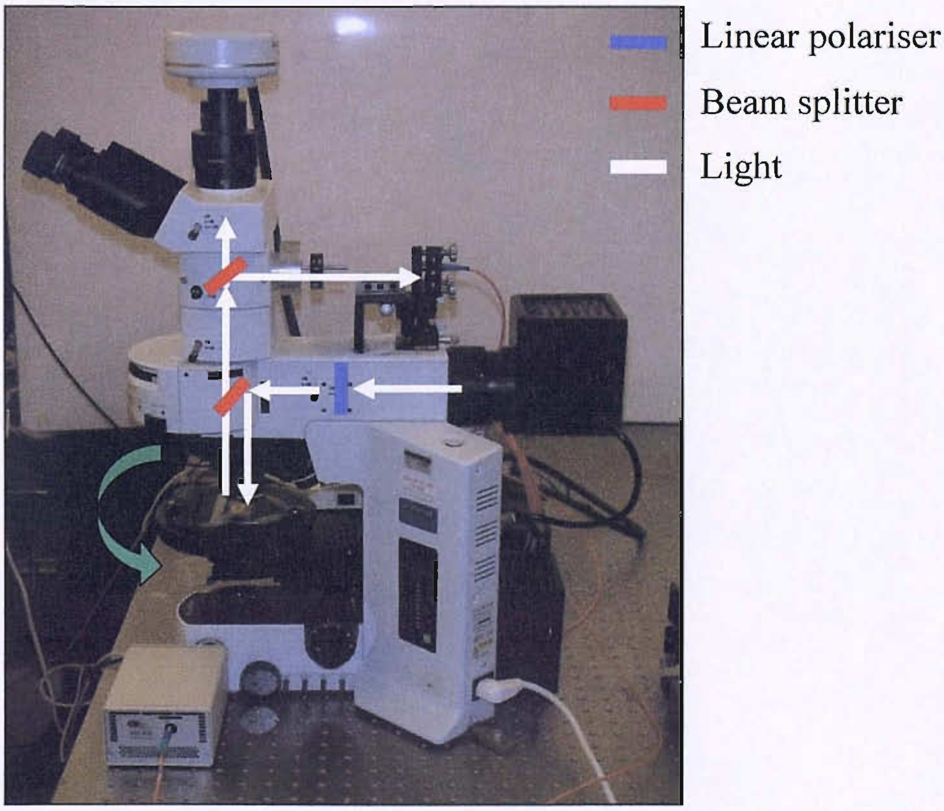

Figure 2.8: Image of the microscope used for birefringence measurement.

UV-Vis transmission and reflectance spectra were recorded using Jasco UV-Vis V570 spectrometer over a wavelength range of 190 nm to 2500 mn with an aluminium and air reference baseline respectively. However, gold substrates only allowed reflectance measurements to be taken, while transmission and reflectance measurements could be taken with cadmium sulfide and indium tin oxide films.

2.6 References

1. N. B. Bartlett, P. N. Birkin, A. M. Ganhem, P. de Groot, M. Sawicki, *Journal of the Electrochemical Society* **148**, C119 (2001).
2. I. Nandhakumar, J. M. Elliot, G. S. Attard, *Chemical Materials* **13**, 3840 (2001).
3. K. Choi, H. C. Lichtenegger, G. D. Stucky, *Journal of the American Chemical Socitey* **124**, 12402 (2002).
4. N. R. B. Coleman, PhD, Southampton University (1997).

CHAPTER THREE

FABRICATION AND CHARACTERISATION OF NANOSTRUCTURED TELLURIUM

3.1 INTRODUCTION

Over the last 10 years tellurium (Te) has become the focus of intense research because of its existing and potential use in a wide range of technological devices. Tellurium is already used as a surface modifier in electrocatalysis (*1*), and as a growth layer for germanium (2) and cadmium telluride on Si (001) surfaces (3). It is also a prominent binary and ternary element in photovoltaic (PV) and photoelectrochemical (PEC) cells in II-VI semiconductors such as CdTe, ZnTe and CdHgTe (*4, 5*) and is also used as a back contact in PV cells (*6*). More complex systems incorporating tellurium are now under investigation such as: Te in zeolite structures (*7*) and porous silicates (*8*), Te as a self assembled monolayer surface (SAM) (*9*) and finally Te used in non-linear optics (NLO) systems (*10, 11*). Our motivation for synthesizing mesoporous nanostructured films of tellurium was driven by its relevance as a component in binary and ternary compound semiconductors such as CdTe and HgCdTe which are considered to be promising candidates for photovoltaic and various optoelectronic applications. Furthermore, tellurium is one of the metalloids and has particularly interesting electronic properties (*12*). Nanostructured metalloid/semiconducting films with one or more critical dimension in the nanometer range can be expected to possess unusual electronic and optical properties. These may be of relevance to understanding the fundamental physics of low-dimensionality structures and, potentially, to applications in sensors, optical devices and solar cells.

The electrochemistry of tellurium is complex (*9, 13-28*) because tellurium is an amphoteric element, and can exist as a multivalent species Te(II), Te(0) and Te(IV) giving rise to complex electrochemical reactions. It can be electrodeposited from both acidic and alkaline solutions, however in the present study we will only focus on the electrodepositon of tellurium from acidic media (*13-17, 19-22, 27, 28*). The electrocactive species in acidic media is the telluryl cation which is formed by the dissolution of tellurium dioxide or tellurite salts in acidic solutions. It is now generally accepted that the reduction of Te(IV) to Te(0) is a 4 electron diffusion-controlled process, (i.e. the rate of deposition is affected by a change in concentration of the Te(IV) ions due to the depletion of reactive ions in the aqueous medium) (*14, 23, 29*) according to the equation:

$$HTeO_2^+{}_{(aq)} + 3H^+{}_{(aq)} + 4\ e^- \longrightarrow Te_{(s)} + 2H_2O_{(l)} \qquad [3.2]$$

At electrode potentials more negative than ~-0.6 V *vs*. SCE a second mechanism for Te(0) deposition can occur (*30*):

$$HTeO_2^+ + 5H^+ + 6e^- \longrightarrow H_2Te\ + 2\ H_2O \qquad [3.3]$$

and

$$2H_2Te\ +\ HTeO_2^+ \longrightarrow 3\ Te_{(s)} + 2\ H_2O + H^+ \qquad [3.4]$$

The reaction processes associated with the electrodeposition of Te (reaction 3.2) are dependant on experimental conditions such as pH, precursor salt concentration, temperature and the electrode substrate, some of which will be addressed in this chapter.

Tellurium dioxide has a low solubility.Its solubility in acid solutions is determined by:

$\mathrm{Log}_{10}\ [TeO_2] = -0.845pH - 2.5$ where $(1.2 < pH < 2.6)$ (*31*)

(with the concentration of TeO_2 in mol dm^{-3}).

Therefore, extremely low pH conditions are required to aid dissolution (*32*). Electrochemically this provides problems since low pH values promote hydrogen evolution at potentials close to that of bulk Te deposition. Although a low pH increases the solubility of Te enabling higher tellurium solution concentrations and thereby higher deposition rates (*32*) this also results in dendritic films (*33*) which are not of good optical grade quality. Recent studies have shown that complexing agents such as citric acid (*25, 34*) and a new tellurium precursor salt, in the form of metastable TeO_2 (*35*), can increase the solubility of Te at pH values ~2.5. In this way the concentration of tellurium precursor salts in plating baths can be increased while the deposition overpotential can be reduced and a high deposition rate can be maintained (*36*).

As previously mentioned the electrode substrate influences deposition of the tellurium. The reversible Nerstian potential for bulk tellurium deposition from $HTeO_2^+$ is 0.284 V *vs.* SCE and is given by equation 3.6. However, much of the literature reveals that for bulk tellurim deposition to occur on foreign substrates such as Au and ITO, large negative overpotentials of ~-0.5 V must be used.

$$E = 0.551 + \frac{2.3RT}{nF}\log\frac{1}{[HTeO_2^+][H^+]^3} \quad \text{and } n = 4 \qquad vs.\ \text{NHE} \qquad [3.6]$$

Strong intramolecular bonding to Au and ITO electrodes is evidenced in cyclic voltammetry by a large potential separation between the anodic and cathodic peaks. Cyclic voltammetry studies of tellurium deposition on gold reveal that the electrodeposition of Au is irreversible, suggesting that strong interactions, described as alloy or surface compound formation, occurs between gold and tellurium (*16*). These strong interactions have been observed on tin oxide, germanium (2) and silicon (001) substrates (*37*).

Peter, Mori and Stickney *et. al* (*22, 24*) have also conducted studies into the effects of the substrate on tellurium deposition employing cyclic voltammetry. A wide range of substrates such as silicon, glassy carbon, gold and ITO were investigated and the results show that Te deposition critically depends on the nature of the substrate. It is suggested that tellurium deposition on metals is different to that on semiconductors (*32*), especially with respect to the hydrogen electrochemistry (*33*). For example, on ITO for tellurium deposition to occur requires more negative overpotentials than on gold and platinum (*13*). The successful electrodeposition of an element must occur at potentials more positive than its limiting current deposition, otherwise a high rate of deposition leads to the growth of a dendritic film. Also at very negative deposition potentials hydrogen evolution becomes a significant factor (*21, 38*).

It has recently been shown that well adherent and films of mesoporous selenium (Se) can be prepared by electrodeposition from a liquid crystal surfactant template. The following sections will describe the results of a study in which the true liquid crystal templating strategy has been extended to the fabrication of mesoporous films of tellurium. Information regarding the behaviour of Te^{4+} in the domains of a liquid crystal template mixture will be presented and examined along with the feasibility of producing highly adherent, H$_I$-eTe films using surfactant templates will also be assessed. The limitations of surfactant based depositions with respect to the electrode potential will also be discussed using the results from chronoamperometry, wide angle XRD and FE-SEM investigations. Finally the results of characterisation studies on the mesoporous tellurium films using low angle XRD and TEM will be presented.

3.2 EMPLOYING LIQUID CRYSTAL TEMPLATES:

3.2.1 Polarised optical microscopy and the hexagonal phase template

Polarised optical microscopy (POM) was used to identify the phase structures within the liquid crystal template mixtures based on their characteristic optical texture. Different micellar structures (phases) were observed depending on the ratio of the precursor tellurium salt solution to the surfactant concentrations, and the temperature employed.

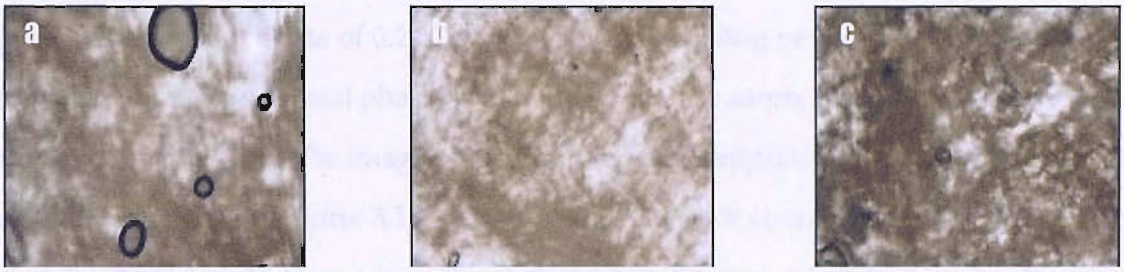

Figure 3.1: Polarised optical micrographs of hexagonal phase template mixtures comprised of 5 mM TeO_2 and 2 M H_2SO_4 mixed with (a). 40 wt.%, (b). 50 wt.% and (c). 60 wt.% concentrations of $C_{16}EO_8$. All images 0.71 mm wide.

Figure 3.1 shows the optical textures for template mixtures containing various wt.% of a 5 mM TeO_2 and 2 M H_2SO_4 solution and $C_{16}EO_8$. Figures 3.1a, 3.1b and 3.1c show the results using 40 wt.%, 50 wt.% and 60 wt.% $C_{16}EO_8$, respectively. The POM images (figures 3.1a-c) clearly depict the feathery appearance associated with the hexagonal

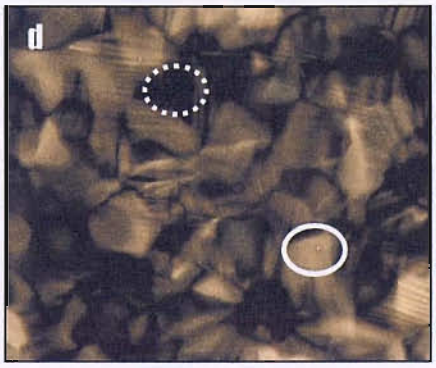

Figure 3.1d: Polarised optical micrographs of H_I Te template mixture from figure 3.1b after heating to a temperature of 70 °C and cooling at a rate of 0.2 °C min^{-1} to <60 °C. Circles indicate the differently oriented directors of the surfactant. Image 0.71 mm wide

(H_I) phase. In figure 3.1a, angular bubbles were observed which is indicative for the hexagonal phase. Finally another sign of the hexagonal phase was the high viscosity of the mixture. This was verified by gently moving the coverslip with the template sandwiched between the glass slide beneath. The surfactant molecules in the H_I phase are arranged in periodically spaced cylindrical columns disposed on a hexagonal array. At 50 wt.% it was possible to prepare a reproducible, well-defined hexagonal phase mixture.

To provide a more ordered structure a 50 wt. % H_I phase template mixture (figure 3.1b) was heated above its isotropisation temperature (64 °C) at a rate of 5 °C min^{-1} and then gradually cooled at a rate of 0.2 °C min^{-1}. This slow cooling process allows improved formation of the hexagonal phase by comparison to the as-prepared template mixture shown in Figure 3.1d. The image of the liquid crystal template now shows larger more clearly defined light (Figure 3.1d, dotted circle) and dark areas (Figure 3.1d, solid circle), which denote areas where the surfactant molecules are aligned in one direction in one region of the same colour.

3.2.2 Phase diagrams

POM can be used to determine the phase diagram for liquid crystal template mixtures based on the concentration and temperature boundaries of a specific surfactant system. Ensuring electrochemical depositon from the the desired liquid crystal phase (e.g. such as the hexagonal phase) requires careful control over surfactant/electrolyte concentrations and temperature. Therefore, POM enables us to construct a phase diagram which allows a particular micellar aggregate structure to be deduced at a particular concentration and temperature. Figure 3.2 shows the phase diagram which is obtained when using a mixture of a tellurium electrolyte solution (2 M H_2SO_4 and 5 mM TeO_2) and $C_{16}EO_8$. This is also the template mixture which is used for the electrodeposition of mesoporous tellurium films on gold (section 3.2.1). At low concentrations (<32 wt. %) of $C_{16}EO_8$ over the temperature range 20-90 °C the micellar phase (L_I) is observed. By increasing the surfactant concentration to between 32 and 64 wt. % and at temperatures from 20 to 50 °C, the hexagonal (H_I) phase exists. At higher temperatures (55-90 °C) and within this concentration limit the micellar (L_I), hexagonal

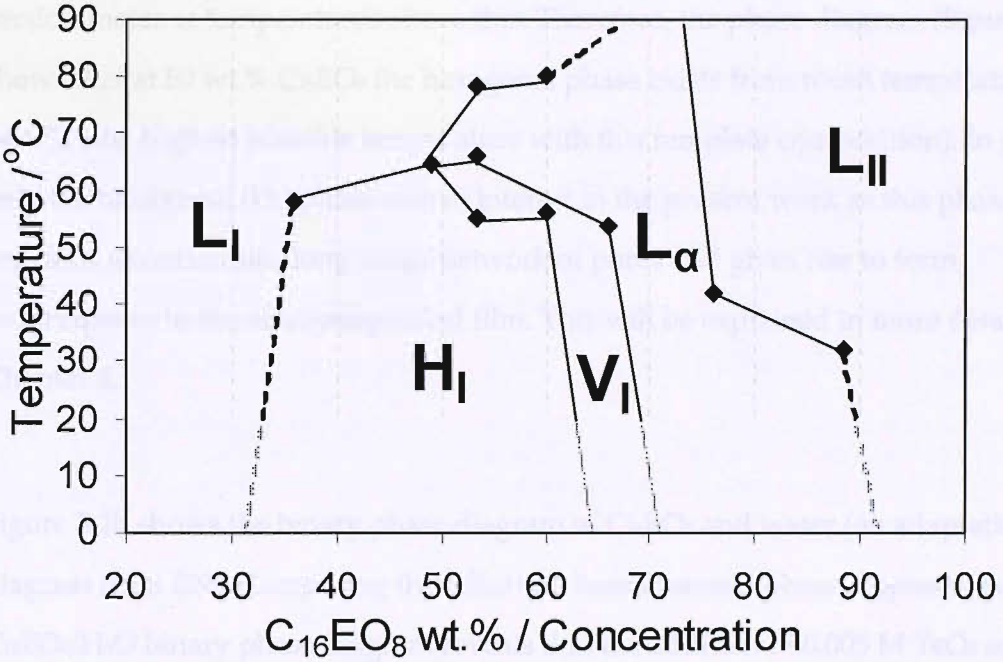

Figure 3.2a : The phase diagram for $C_{16}EO_8$ mixed at various concentrations with an aqueous solution containing 5 mM TeO_2, and 2 M H_2SO_4 (pH = 0.05). The dotted lines indicate undefined boundaries. Below 20 °C the phase boundaries cannot be defined and dotted lines only offer a guide.

(H_I), lamellar (L_α) and cubic (V_I) phase may exist (depending on the temperature). The fact that more than one phase can be produced at a certain concentration or temperature emphasises the need for strict control over both the temperature and concentration conditions in order to create a well defined liquid crystal template mixture phase. At higher concentrations of 72-90 wt.% the lamellar phase ($L\alpha$) predominates over the 20 to 30 °C range while the inverse micellar (L_{II}) phase predominates at temperatures above this. Therefore, the phase diagram (figure 3.2a) shows that at 50 wt.% $C_{16}EO_8$ the hexagonal phase exists from room temperature to 64.4 °C (the highest possible temperature with this template composition). In general, only the hexagonal (H_I) phase was of interest in the present work as this phase provides a continuous, long range network of pores and gives rise to form birefringence in the electrodeposited film. This will be explained in more detail in Chapter 4.

Figure 3.2b shows the binary phase diagram of $C_{16}EO_8$ and water (an adaptation of a diagram from (*39*). Comparing the tellurium based ternary phase diagram and the $C_{16}EO_8/H_2O$ binary phase diagram reveals that the addition of 0.005 M TeO_2 and 2 M H_2SO_4 creates minor differences in the phase boundaries. It should be noted that the I_I phase is not apparent in figure 3.2a, as the POM of the template mixtures was not investigated over the temperature ranges of 0 to 20 °C. This suggests that addition of

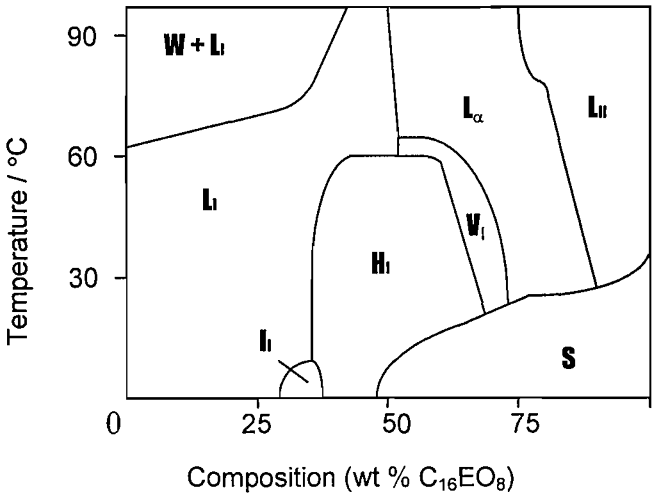

Figure 3.2b: Binary $C_{16}EO_8$ + water phase diagram.

sulphuric acid and the tellurium salt at these concentrations did not destablise the observed liquid crystal phases and in terms of the hexagonal phase provided further stabilisation of the phase at higher temperatures.

Other Te based template mixtures

Electrochemical fabrication of mesoporous tellurium films was also carried out on ITO substrates. For this a low sulphuric acid concentration was required to avoid dendritic film growth and template mixtures containing 50 wt.% of a 0.5 mM TeO_2 and 0.025 M H_2SO_4 solution (pH = 1.49) with 50 wt.% $C_{16}EO$ were used for this purpose. As a 5 mM tellurium and 2 M sulfuric acid and $C_{16}EO$ liquid crystal mixture did not markedly change the phase boundaries by comparison to the $C_{16}EO_8$/water system (seen in figure 3.2b), it was concluded that using 0.5 mM TeO_2 and 0.025 M H_2SO_4 to prepare a liquid crystal template mixture would have a neligible effect on its binary phase diagram. Hence a separate phase diagram was not constructed under these conditions.

3.3 ELECTRODEPOSITION OF H$_{\mathrm{I}}$-eTe

3.3.1 Cyclic Voltammetry on Gold

Cyclic voltammetry was used to define the major characteristics of tellurium electrochemistry on metal electrodes from an aqueous solution and from the domains of a liquid crystal mixture.

Primarily, gold was selected as the working electrode material because of its ease of handling and its large electrochemical potential window allowing well-defined Te deposition features. In addition, optically transparent indium tin oxide (ITO) substrates were also used.

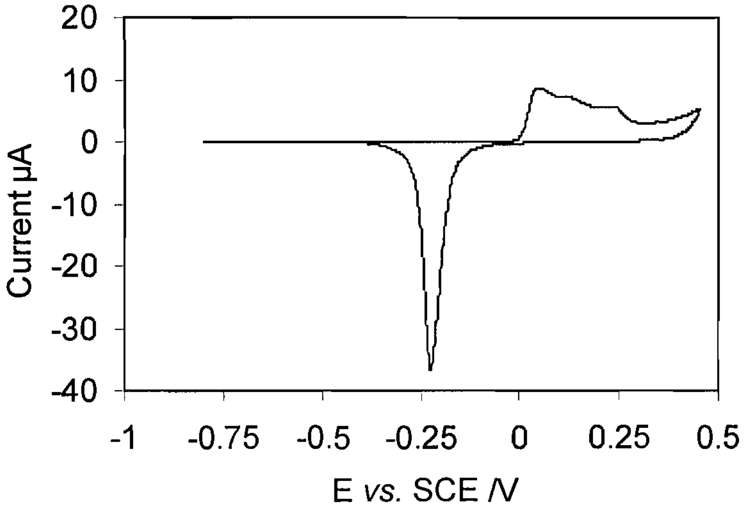

Figure 3.3: Cyclic voltammogram of a 0.5 mm gold wire immersed in a 2 M H_2SO_4 solution at a scan rate of 20 mV/s at ambient temperature conditions.

Before any experiments were conducted the cleanliness of the gold electrode was established by cyclic voltammetry in order to ensure reproducibility and consistency. Therefore, a voltammogram of Au in a blank electrolyte solution (2 M H_2SO_4) was taken and is shown in figure 3.3. This represents a clean Au electrode. The clean gold working electrode surface was prepared by flame annealing in a butane flame in the case of a gold wire, and sonication in isopropanol in the case of gold on glass electrodes. This was done prior to recording the voltammograms and was essential to assure that the surface was free of impurities.

The cyclic voltammogram depicted in figure 3.3 reveals three characteristic features. Firstly, a large double layer region, extending from -0.8 V to -0.4 V *vs.* SCE. Secondly, an intense cathodic stripping peak at -0.22 V *vs.* SCE and finally a broad oxygen adsorption peak from 0.0 V to 0.45 V *vs.* SCE with a current maximum at 0.05 V *vs.* SCE. These cyclic voltammogram features are representative of a clean gold surface (*40*). Following this it was now possible to reproducibly electrodeposit tellurium onto the gold working electrode from an aqueous solution and also from a liquid crystalline mixture.

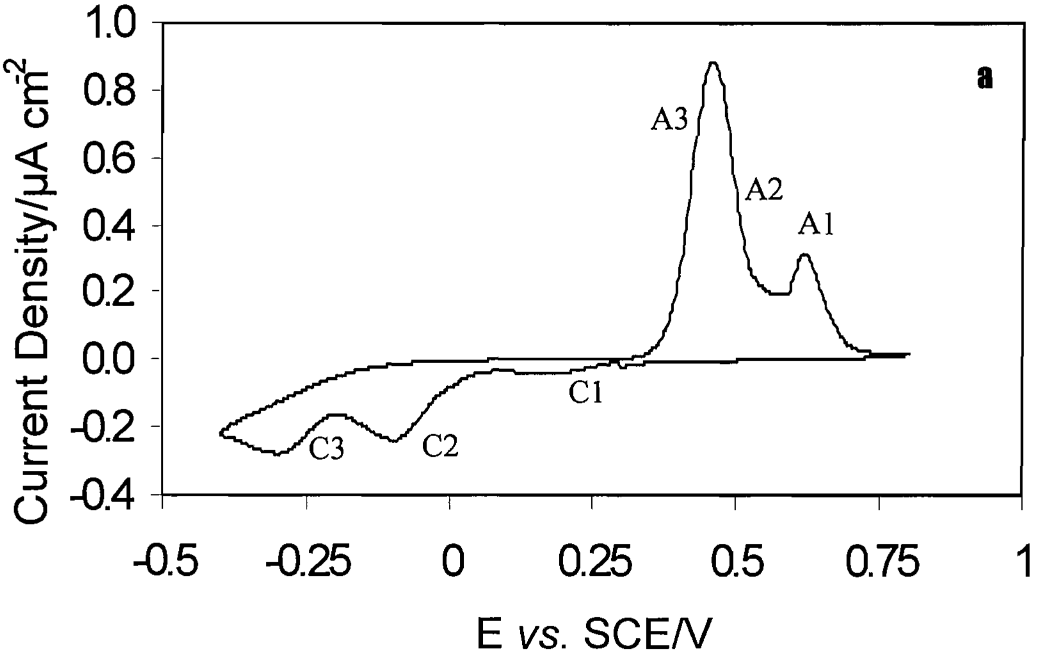

Figure 3.4a: Cyclic voltammogram of a gold electrode in a mixture of 50wt.% of 0.005 M TeO_2, 2 M H_2SO_4 and 50 wt. % $C_{16}EO_8$. Scan rate = 20 mV/s and ambient temperature conditions. Electrode area: 1.23 cm^2

Cyclic voltammogramms of gold electrodes in solutions containing 0.005 M TeO_2 and 2 M H_2SO_4 with and without $C_{16}EO_8$ were carried out in order to compare the electrochemistry of Te in both media. Figure 3.4a displays a cyclic voltammogram for the deposition of tellurium on polycrystalline gold from templating mixtures containing 50 wt. % of $C_{16}EO_8$ and 50 wt. % of a solution containing 0.005 M TeO_2 and 2 M H_2SO_4. The voltammogram exhibits two clear reduction features at 0.16 and -0.08 V (C1 and C2) prior to the onset of bulk tellurium deposition at –0.310 V (C3). C1 and C2 can be assigned to the underpotential deposition (UPD) of tellurium in accordance with other studies. UPD refers to a process whereby a metal is electrodeposited onto a foreign metal substrate at potentials more positive than that required for the reversible Nernstian potential for bulk deposition ($E_{eq} = 0.598$). This is a consequence of a stronger adsorbate-substrate interaction relative to a weaker adsorbate-adsorbate interaction (*26*). For tellurium, interatomic bonding is thermodynamically more favourable than intra-atomic bonding (*41*). The corresponding oxidative stripping peaks were observed in the subsequent positive scan. Firstly, peak A3 at 0.47 V is associated with the oxidative stripping of bulk tellurium from C3. The following peaks A1 (0.63 V) and A2 (0.50 V) (peak A2 appears as a very slight shoulder on peak A3) correspond to the stripping of tellurium deposited at C1 and C2 respectively. The cyclic voltammogram of tellurium deposition as obtained here from a liquid crystalline mixture is in good agreement with those reported in other studies which were obtained from aqueous solutions. (*12, 22, 26, 27*)

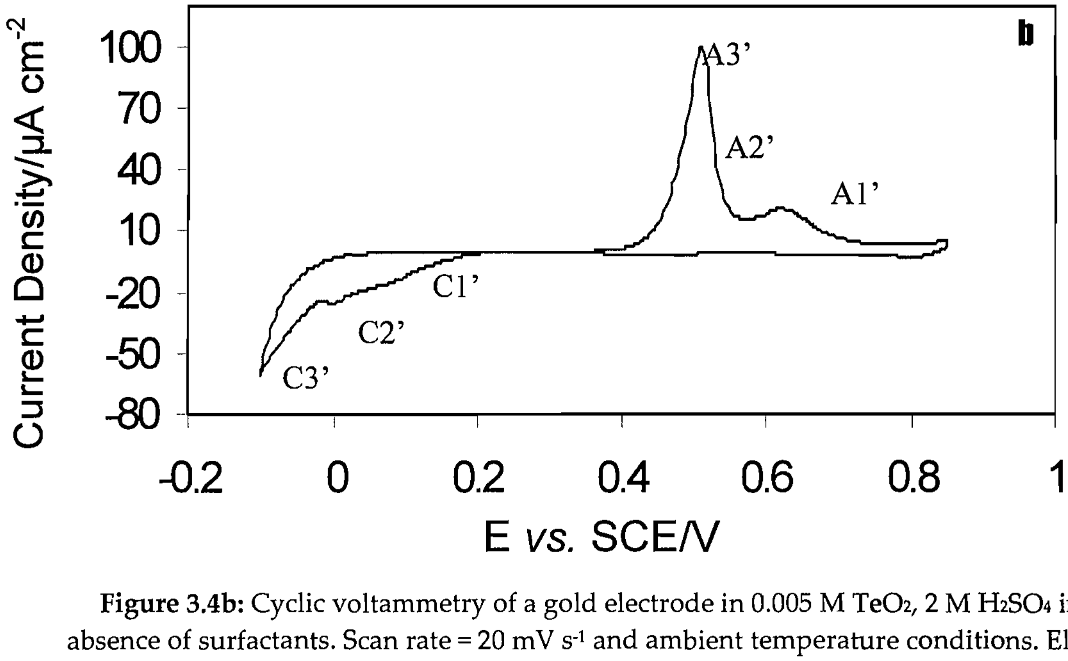

Figure 3.4b: Cyclic voltammetry of a gold electrode in 0.005 M TeO_2, 2 M H_2SO_4 in the absence of surfactants. Scan rate = 20 mV s^{-1} and ambient temperature conditions. Electrode area: 1.19 cm^2.

The integated area under the cathodic peaks (C1, C2 and C3) and the anodic peaks (A1, A2, A3) was determined and the difference in charge was found to be -1.37±0.03 mC cm^{-2}. The cathodic charge was greater by comparison to the anodic charge for the cyclic voltammetry of a gold working electrode in a mixture comprising 50 wt.% of a solution containing 5 mM TeO_2 /2 M H_2SO_4 and 50wt.% $C_{16}EO_8$ (figure 3.4a). By comparing the charges for the reduction and oxidation reactions confirmed that the reaction is not reversible.

For comparison cyclic voltammograms of Te deposition on gold were also acquired from a solution containing no surfactant and are shown in figure 3.4b. On the negative scan, cathodic peaks associated with the deposition of Te on gold are observed, commencing at 0.2 V, where the first peak is observed (C1′). The second peak, C2′, is detected by a current increase at 0.1 V. The final current density increase, C3′ commences at -0.025 V and rapidly increases at more negative potentials. On the positive scan coalescence of the A3′ and A2′ peaks is observed at ~0.475 V resulting in an intense peak. The stripping of the 1st tellurium peak occurs at 0.63 V (A1′), a difference of only 0.05 V from the surfactant based cyclic voltammetry for the deposition of Te on Au. The difference in peak positions between the respective anodic and cathodic peaks observed in figure 3.4b agree well with those reported by Stickney and Ikemiya (*16, 27*). A large potential difference (0.78 V) exists between the cathodic and anodic peaks of the first (C1′) and (A1′) tellurium peak in the voltammogram (figure 3.4b), suggesting that the deposition of tellurium is irreversible (*27*). This is due to a thermodynamically favourable strong interaction between tellurium and gold. Reduction of the electrodeposited tellurium and subsequent oxidation becomes difficult due to the strong interatomic bonding between the tellurium and the gold.

The cyclic voltammogram in Figure 3.4a shows a negative shift of almost -0.3 V for bulk tellurium deposition in the liquid crystal mixture. This may be a direct result of the viscous nature of the template mixture, reducing the diffusion rate of Te^{4+} ions thus producing slower kinetics. A further indication for the reduction in the rate of tellurium deposition as a direct result of the presence of the liquid crystal phase can be seen by looking at the current density values in both the cyclic voltammogram, 3.4a and b. For example, the peak current density associated with peak A3′ is approximately 100 times higher than that found for peak A3.

3.3.2 Cyclic voltammetry of tellurium on indium tin oxide

Figure 3.5 shows the cyclic voltammogram of an ITO electrode in a mixture of 50 wt.% of a solution containing 0.5 mM TeO_2, 0.025 M H_2SO_4 (pH 1.49) and 50 wt. % $C_{16}EO_8$ over the potential range 0.8 V to -0.8 V *vs.* SCE. The origin of the scan was 0.0 V and a scan rate of 20 mV s^{-1} was used. The onset of a cathodic current is observed at -0.25 V and rises to a current density of 0.055 mA cm^{-2} at -0.43 V. The current density then decreases to a plateau region of 0.05 mA cm^{-2} in the potential region -0.53 V to 0.64 V *vs.* SCE. Following this the current density increases sharply to -0.072 mA cm^{-2} at 0.71 V *vs.* SCE. Finally there is a substantial increase in the current at -0.75 V rising to a current density of -0.20 mA cm^{-2}. The anodic scan shows an initial current density peak and plateau of 0.01 mA cm^{-2} from 0.1 to 0.325 V (A1). The following peak occurs at 0.54 V rising to 0.045 mA cm^{-2} (A2). C1 can be assigned to the underpotential deposition of Te. While the peak observed at C2 is assumed to be bulk Te, the cathodic peak at C3 may be attributed to hydrogen evolution because electrodeposition of Te at potentials more negative than -0.6 V leads to dendritic non-adherent films, where the deposition is competing with H_2 evolution as evidenced by the formation of pinholes on the electrode surface. The cathodic and anodic peak positions observed in the cyclic voltammogram for a solution containing 5mM TeO_2 in 2 M H_2SO_4 are 0.2 V more positive than those obtained by Kadirgan *et. al.*(*13*). It must be noted that these results were obtained using 0.3 mM TeO_2 at a pH of 1.6 and therefore the difference in the electrode potential may be due to the higher pH and difference in plating bath. However, it is proposed that the electrodeposition reaction for Te shown in equation 3.2 is the same for Kadirgan *et. al.* (*13*) The potential range for the occurrence of reaction 3.1 is less than -0.5 V *vs.* SCE and therefore more negative than the values obtained by Dennison on a rotating disk glassy carbon electrode (*33*), but in agreement with Mori *et. al.* (*24*).

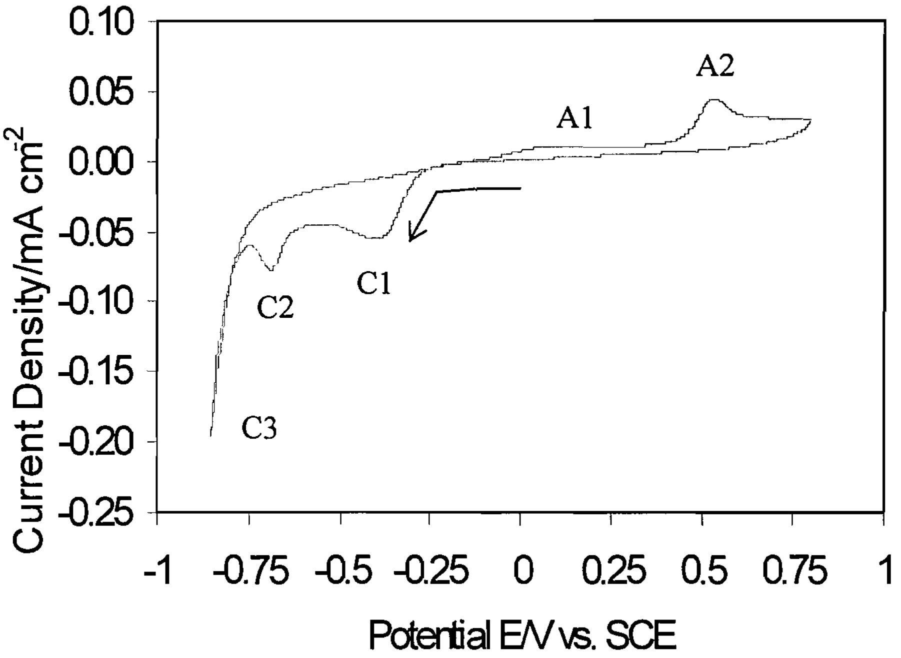

Figure 3.5: Cyclic voltammogram of a ITO electrode in a mixture of 50 wt.% of a solution containing 0.5 mM TeO_2, 0.025 M H_2SO_4 and 50 wt. % $C_{16}EO_8$ mixture. Scan rate = 20 mV s^{-1} and ambient temperature. pH =1.49. Electrode area= 1.27 cm^2

The deposition of bulk tellurium on ITO (figure 3.5) occurs at –0.5 V, which is approximately –0.4 V lower than the value found for tellurium deposition on Au (figures 3.4a and b) the reduction features are similar but are shifted to more negative potentials. The more negative electrodepositon potential for H_I-eTe on ITO compared with H_I-eTe on Au can be accounted for by the nature of the electrode and the sensitivity of Te electrochemistry with regard to the nature of the substrate. The growth of Te nucleation sites on the surface of the ITO electrode is much more difficult (due to iR drop effects) than on the Au. Therefore higher over potentials are required to induce the electrodeposition. Also, a significantly higher pH of 1.49 was used to carry out the electrodeposition of tellurium on ITO, as opposed to 0.05 for gold electrodes. The use of higher pH values also leads to a more negative reversible Nernstian potential for tellurium bulk deposition. Figure 3.5 shows a C3 peak appearing at -0.8 V. This final cathodic increase shows a very sharp reduction peak and may be attributed to hydrogen evolution.

3.3.3 Chronoamperometry of tellurium electrodeposition

Figure 3.6 shows current-time transients for the electrochemical deposition of tellurium within the domains of a hexagonal phase of a liquid crystal template containing 5 mM

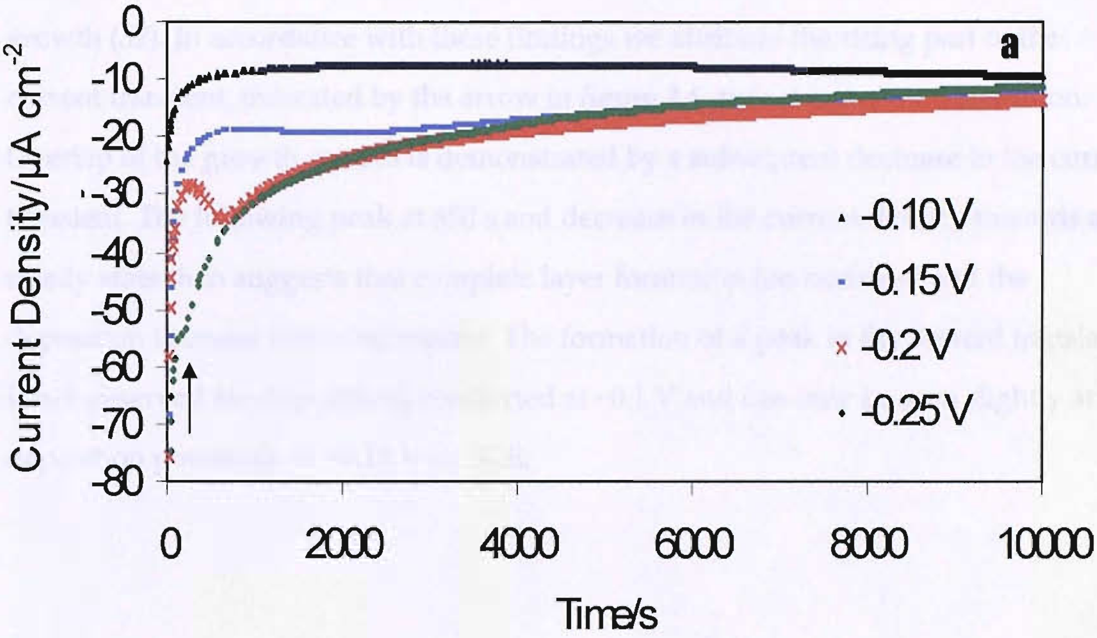

Figure 3.6: Current time transients for the electrodeposition of H_I-eTe on Au carried out at potentials between –0.10 V to –0.25 V *vs.* SCE. Electrode area: 1.24 cm^{-2}.

TeO_2 and 2 M H_2SO_4. The depositions were all carried out under constant potential control between –0.10 and –0.25 V *vs.* SCE. The deposition transients depict a general trend of a current density which decreases as time progresses. However, at a potential of –0.2 V the initial current density decreases and reaches a minimum of –29 μA cm^{-2} after 350 seconds, then increases to –37 μA cm^{-2} at 830 seconds. The current density then decreases to –11 μA cm^{-2} towards the end of the experiment. At more negative potentials a constant current density is observed after 120 seconds where a maximum then occurs at –54 μA cm^{-2}. The current density then continues to decrease to 8.4 μA cm^{-2}. It should be noted that all the current density profiles displayed tend to a minimum of approximately –10 μA cm^{-2}.

The current transients for depositions carried out at –0.2 V *vs.* SCE provide some evidence for the kinetics of nucleation and growth. Previous studies for the electrodeposition of tellurium in an acidic medium have shown that the rising part of the transient suggests instantaneous nucleation and 3D growth under diffusion control (*38*). In general, the shape of transient responses to potential step experiments shown predicts that the shape of the current transient (figure 3.6, -0.2 V *vs.* SCE) would also be instantaneous nucleation and 3D growth under diffusion control. It has also been sugested that the overall shape of the transient can be a guide to the mechanism of growth (*38*). In accordance with these findings we attribute the rising part of the current transient, indicated by the arrow in figure 3.6, to instantaneous nucleation. Overlap of the growth centres is demonstrated by a subsequent decrease in the current transient. The following peak at 650 s and decrease in the current density towards a steady state then suggests that complete layer formation has occurred and the deposition is under diffusion control. The formation of a peak in the current transients is not observed for depositions conducted at −0.1 V and can only be seen slightly at deposition potentials of −0.15 V *vs.* SCE.

3.4 SURFACE MORPHOLOGY AND FILM QUALITY

3.4.1 Scanning electron microscopy (SEM)

Figure 3.7a shows the Te deposits formed at -0.2 V on a gold electrode at ambient temperatures using a solution containing 2 M H_2SO_4 and 0.005 M TeO_2. Tellurium aggregates on the electrode surface demonstrate the inhomogenous growth of bulk tellurium on gold. EDX results showed that a pure tellurium layer was present and SEM images revealed series of amorphous aggregates of tellurium (figure 3.7b). Figure 3.8a to c reveal the variation in the surface morphology of H_1-eTe electrodeposited at potentials ranging from -0.2 to -0.3 V *vs.* SCE. Although the films were adherent and shiny to the bare eye, SEM micrographs revealed that the films were not flat. This is unlike the images observed for mesoporous films, which were featureless and flat. Dennison *et. al.* showed that dendritic growth occurs for tellurium films deposited in a sulfate media at room temperature (33). It is postulated that a reduction in deposition rate imposed by the liquid crystal template mixture improves the surface morphology. The following results show the effect of the H_1 phase on the surface morphology of electrodeposited H_1-eTe films.

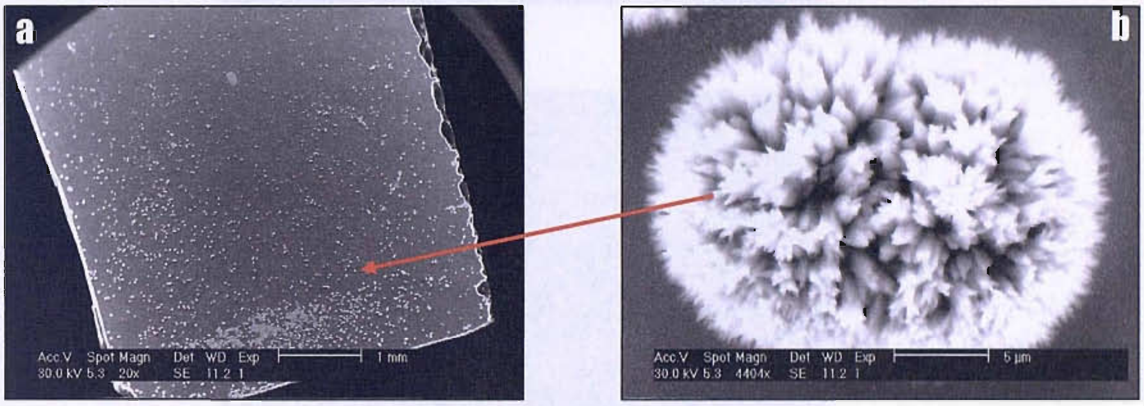

Figure 3.7: SEM images of a Te film on a clean gold electrode at −0.2 V *vs.* SCE from a solution containing 2 M H_2SO_4 and 0.005 M TeO_2. (a) entire electrode with many amorphous tellurium aggregates and (b). Magnified view of an amorphous aggregate.

The H_I-eTe films electrodeposited within the potential window of –0.2 V to –0.3 V *vs.*

Figure 3.8: FE-SEM micrographs of H_I-eTe films electrodeposited at a). –0.2 V, b). -0.25 V and c). –0.3 V *vs.* SCE from a mixture containing 50 wt. % of a 5 mM TeO_2/2M H_2SO_4 solution and 50 wt. % $C_{16}EO_8$. The charge density for the films was 0.82 C cm^{-2} in all three cases.

SCE from the domains of a hexagonal phase template mixture were adherent with a grey lustre and highly reflective in appearance which are desirable features for optical studies.

Deposition potentials more positive than −0.2 V led to films that were adherent but inhomogeneous, grey-brown and dendritic in appearance with poor reproducibility, while at potentials more negative than −0.3 V *vs.* SCE the films, were less adherent and non-reflective when grown using the same plating baths. Electrodeposition of H_I-eTe on ITO at -0.5 V *vs.* SCE yielded adherent, smooth grey metallic films.

A cross-sectional scanning electron micrograph of a H_I-eTe film, electrodeposited onto a gold on glass substrate at -0.2 V *vs.* SCE from the hexagonal liquid crystal phase is shown in figure 3.9. The film appears to be uniform and dense over the gold electrode. The edge of the film is observed at a tilt angle of 70 °.

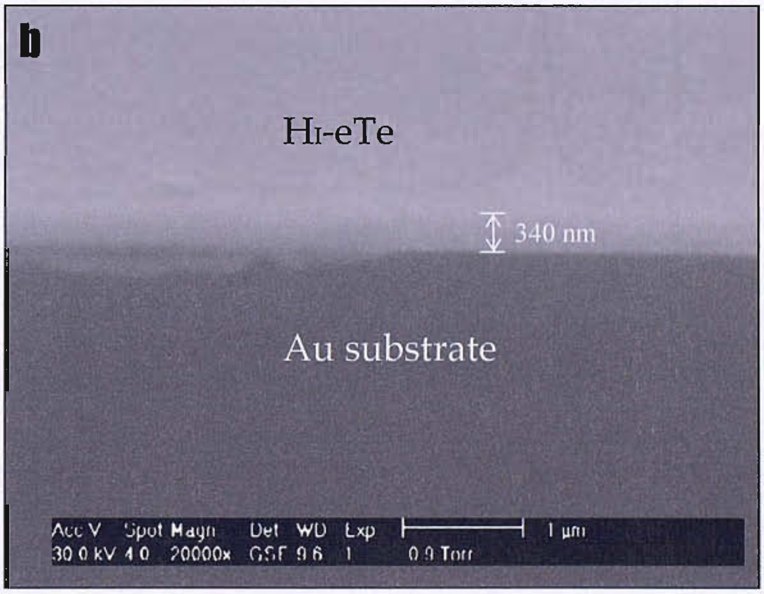

Figure 3.9: Scanning electron micrograph of a H_I –eTe film electrodeposited at -0.2 V *vs.* SCE on a gold substrate from a mixture containing 50 wt. % of a 5 mM TeO_2/2M H_2SO_4 solution depicting at a 70 °tilt.

The observed thickness of the film was measured to be 340 nm using a SEM, with the film at a tilt angle of 70°. However, assuming a perfect hexagonal nanostructure and 100% current efficiency a film thickness of 403 nm was calculated for the Te film using the charge passed during a deposition at -0.2 V *vs.* SCE with a charge of 0.82 C cm^{-2}.

This indicates that the electrodeposition of mesoporous Te from a liquid crystalline template mixture at -0.2 V *vs.* SCE occurs with a current efficiency of ~84%. This may indicate competing reactions, such as H_2 evolution. To improve the current efficency the pH may be lowered leading to a more negative H_2 evolution potential (34, 42).

3.4.2 Wide Angle XRD

The film crystallinity, and therefore the identity of the electrodeposited material, can be established by wide angle XRD. The wide angle XRD patterns of H_I-eTe prepared using $C_{16}EO_8$ (50 wt.%) are shown in Figure 3.10a. The scans were taken in the range of 20-30 ° (2θ) to include the <100> and <101> Te peaks, otherwise these would be 'hidden' by the intense Au peak at 39 ° (2θ) (figure 3.10b). The recorded patterns for H_I-eTe are compared to a typical polycrystalline powdered tellurium pattern from the

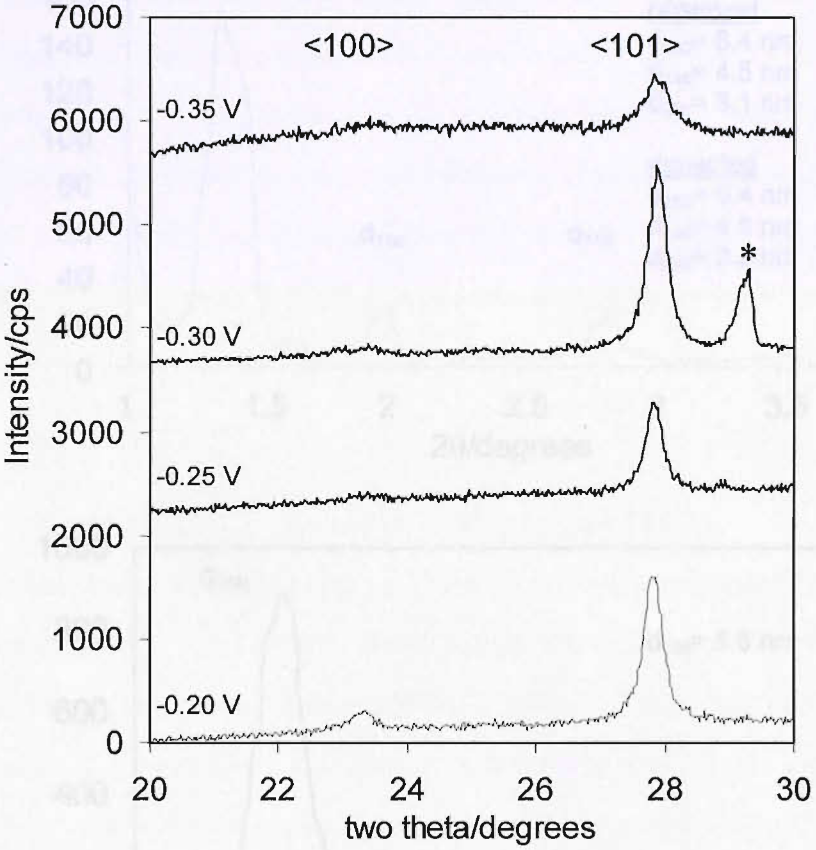

Figure 3.10a: Wide angle XRD for H_I-eTe films on Au deposited at potentials from –0.2 V to –0.35 V *vs.* SCE, at ambient temperature conditions.

Journal of Chemical Physical Diffraction Structures (JCPDS) database, where the <100> and <101> peaks are of an intensity ratio of 1:6 and at positions 23.1 and 27.7 (2θ), respectively (Table 3.1). For comparison, X-ray diffraction data for a non-mesoporous tellurium film is also given (Table 3.1).

Table 3.1: XRD data for H$_I$-eTe, a thin polycrystalline Te film and JCPDS values for powdered hexagonal Te.

Peaks	Te JPCDS		Bulk Te film			H$_I$-eTe film (-0.2 V *vs.* SCE)		
(hkl)	2(θ)/ degrees	Relative Intensity	2(θ)/ degrees	Relative Intensity	Crystallite size/nm	2(θ)/ degrees	Relative Intensity	Crystallite size/nm
100	23.1	16.4	23.4	18.9	22.4	23.4	28.7	31.5
101	27.7	100	27.3	100	74.5	27.8	100	105.6

For mesoporous depositions carried out at -0.2 V *vs.* SCE the XRD diffractogram indicates two clearly defined peaks at 23.4 and 27.8 (2θ) degrees corresponding to the <100> and <101> peaks respectively. These peaks are in close agreement with those for powdered tellurium. The relative peak intensity of the mesoporous film electrodeposited at –0.2 V is 1:11. However, powdered tellurium gave a relative

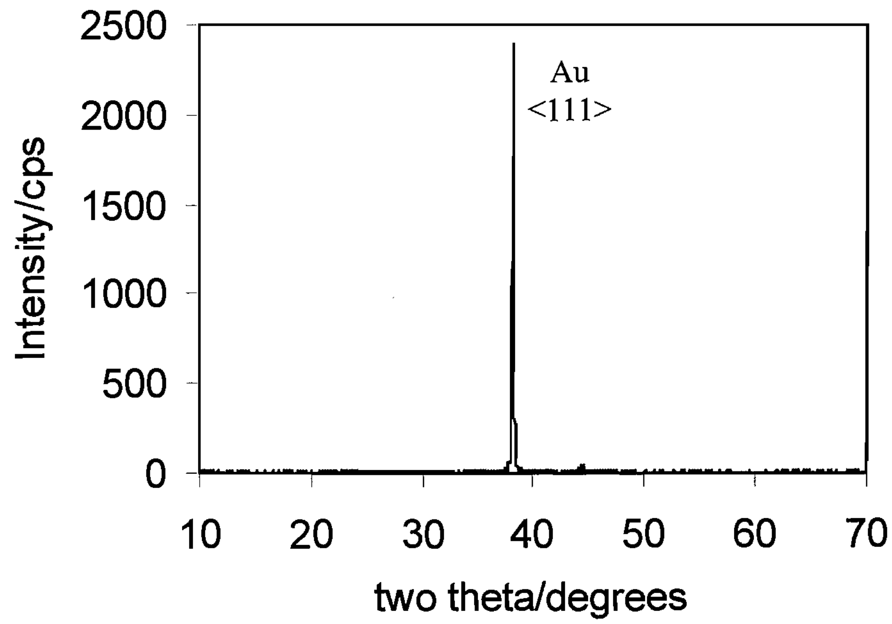

Figure 3.10b: Wide angle XRD for a clean gold on glass electrode.

intensity of 1:6 for the <100> and <101> peaks at 23.1 and 27.7 (2θ). The XRD pattern shows there is a strong <101> texture for the hexagonal close packed structure.

It should be noted that a variation in the potential greatly affected the crystallinity of the films. All films show evidence of the <101> tellurium peak at 27.7 (2θ), however the difference in peak intensity between samples cannot confirm a specific change in crystallite orientation. Deposition at –0.3 V *vs.* SCE gives rise to a peak at 29.5 (2θ) (indicated by an asterix in figure 3.10a). This is an unknown peak and inconsistent with other results. Although, H_I-eTe films deposited at more negative potentials (-0.3 V) appears to produce flatter, denser films (figure 3.8), wide angle XRD patterns showed a decrease in the intensity of the <100> peak. This suggests a reduction in

a). the film thickness

b). the hexagonal film structure

c). the general quality of the film.

Assuming a homogeneous strain across crystallites, the size of microcrystallites can be estimated from the full width half maximum (FWHM) values of the XRD diffraction peaks. The mean crystallite size t, for H_I-eTe and Te was estimated from the FWHM of the <100> and the <101> reflection, using the Debye-Scherrer's equation,

$$b_{101} = 0.9\lambda Cu/(t \cos \theta_{101/100}) \qquad [3.9]$$

where λ is the wavelength (1.5406 Å for Cu $K_{\alpha1}$, and $\theta_{101/100}$ is the peak position. Table 3.1 shows the crystallite size for <100> and <101> peaks for electrodeposited bulk Te and H_I-eTe films.

Energy Dispersive X-Ray (EDX) provides further evidence for the Te content of the films. EDX confirms that H_I-eTe films grown at potentials from -0.2 to -0.3 V *vs.* SCE are tellurium. Trace elements oxygen, sulfur and chloride were found to be present in the films.

To verify whether annealing of the mesoporous tellurium films would induce recrystallisation and as a consequence better quality films these were placed inside a quartz furnace at 400 °C under an O_2 atmosphere for 1 hour. We have observed that this post deposition treatment can render the material non-mesoporous as evidenced by no peaks in the low angle XRD patterns. Therefore, annealing was not applied any further.

3.5 DETERMINING THE MESOPOROSITY

3.5.1 Low angle X-Ray Diffraction (XRD)

Mesoporous films can be characterised by their low angle XRD diffraction patterns. Figure 3.11a shows the XRD pattern for the hexagonal phase (H_I) of a template mixture

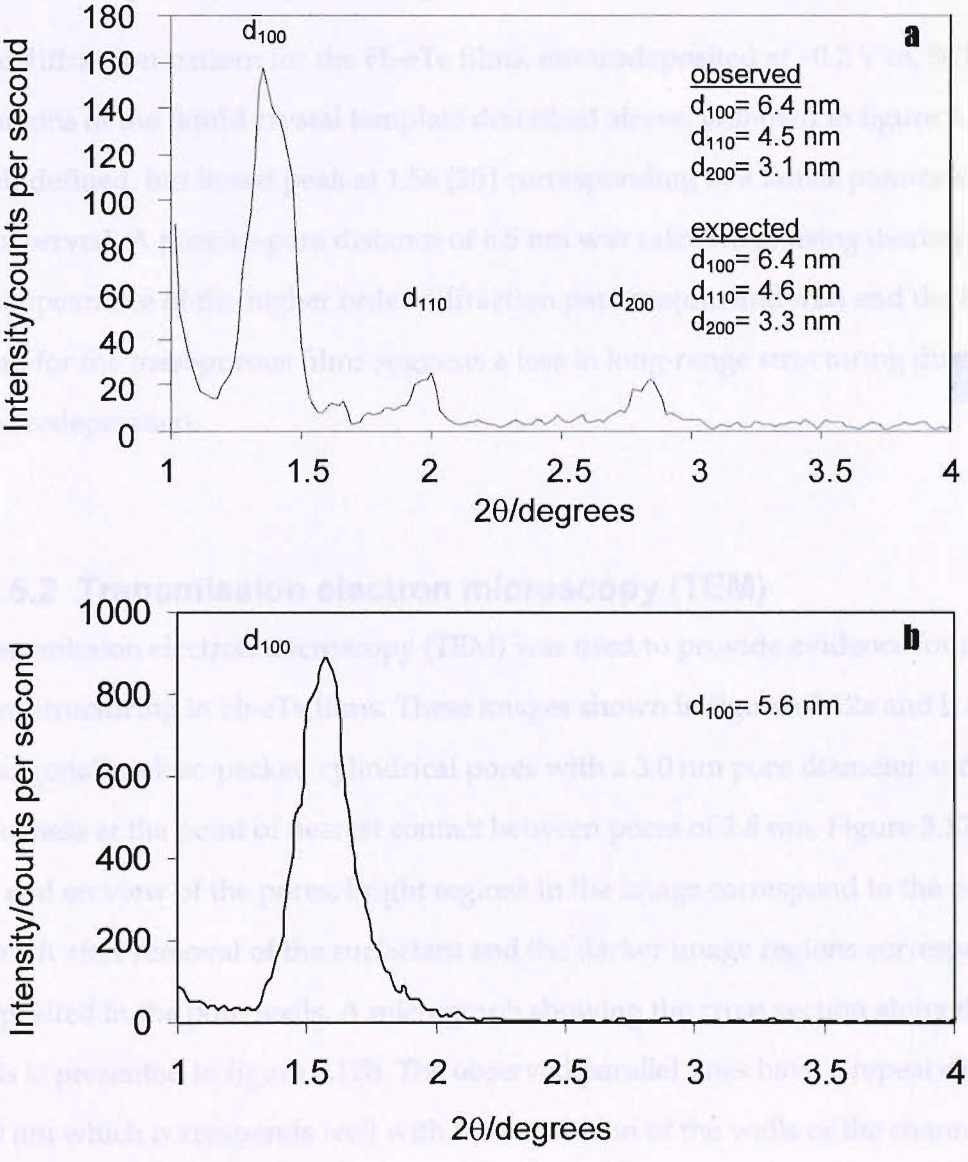

Figure 3.11: Low angle XRD patterns for (a). a liquid crystal template mixture comprised of a 50 wt.% solution of 5 mM TeO_2 + 2 M H_2SO_4 and 50 wt.% $C_{16}EO_8$, and (b). an electrodeposited H_I-eTe film from the mixtur described in (a). The proposed *d*-spacing peak and corresponding lattice parameters are given.

containing 50 wt.% $C_{16}EO_8$ and 50 wt.% of an electrolyte solution containing 5 mM TeO_2 and 2 M H_2SO_4. Low angle XRD clearly reveals a primary d_{100} reflection at 1.37 ° (2θ) which can be translated into a lattice parameter of 6.4 nm using the Bragg equation (chapter 1). The liquid crystal template mixture is highly ordered and this is evidenced by the presence of two higher order diffraction peaks, d_{110} and d_{20}. The 110 and 200 *d*-spacings have a lattice parameter of 4.5 nm and 3.1 nm, respectively. The *d*-spacings are in close agreement to the positional ratio of $1:1/\sqrt{3}:1/2$ (see expected values in figure 3.11a) for the hexagonal structure d-spacings supplied by JCPDS (chapter 2). This suggests there maybe some phase mixing. The difference in ratio may be closer to the lamellar phase peak positioning.

The diffraction pattern for the H_I-eTe films, electrodeposited at –0.2 V *vs.* SCE in the domains of the liquid crystal template described above, is shown in figure 3.11b. A well-defined, but broad peak at 1.58 (2θ) corresponding to a lattice parameter of 5.6 nm is observed. A pore-to-pore distance of 6.5 nm was calculated, using $d_{100}/\cos 30°$. The disappearance of the higher order diffraction patterns(d_{110} and d_{200}) and the broad d_{100} peak for the mesoporous films suggests a loss in long-range structuring during electrodeposition.

3.5.2 Transmission electron microscopy (TEM)

Transmission electron microscopy (TEM) was used to provide evidence for the nanostructuring in H_I-eTe films. These images shown in figures 3.12a and b reveal hexagonally, close-packed cylindrical pores with a 3.0 nm pore diameter and a wall thickness at the point of nearest contact between pores of 2.8 nm. Figure 3.12a depicts an end on view of the pores; bright regions in the image correspond to the pores which are left after removal of the surfactant and the darker image regions correspond to Te deposited in the pore walls. A micrograph showing the cross section along the channel axis is presented in figure 3.12b. The observed parallel lines have a repeat distance of 3.0 nm which corresponds well with the separation of the walls of the channels. Therefore, the pore-to-pore value from TEM measurements is 5.8 nm which is not in close correspondence to the value of 6.5 nm obtained by X-ray diffraction (section

3.5.1). The deviation from the X-ray diffraction results are caused by the orientation of the mesoporous film with respect to the incident X-ray beam. Variation in the film height and angle of the film in the sample holder may lead to significant deviations in the calculated lattice parameter. Table 2 compares the pore dimensions of HI-eTe and HI-ePt films. The mesoporous tellurium pore values are comparable with those found for mesoporous platinum (43).

[illegible]

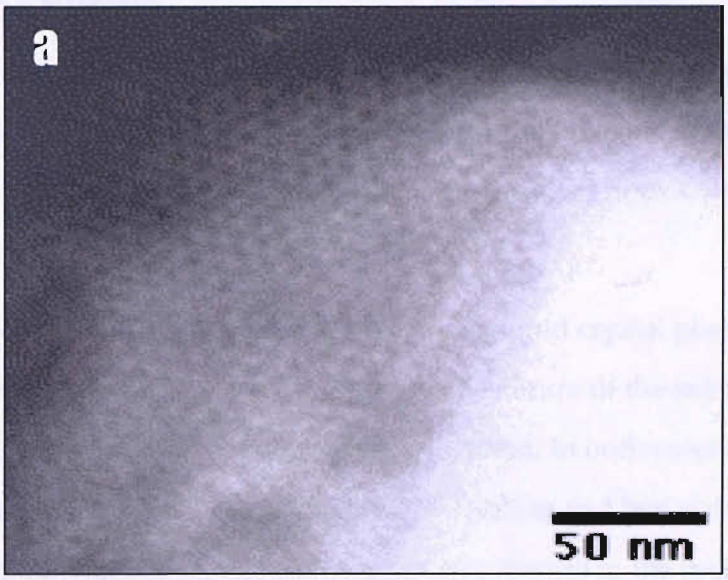

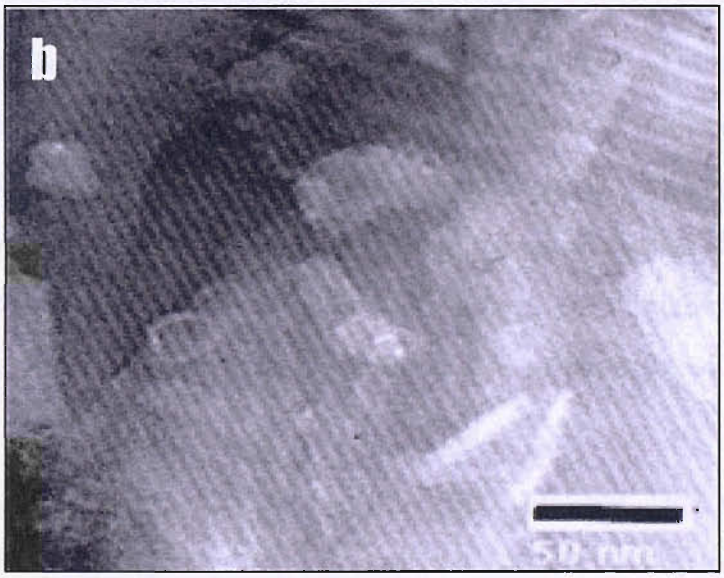

Figure 3.12: Transmission electron micrographs of H_I-eTe on Au prepared from a mixture containing 50 wt. % of $C_{16}EO_8$ and a 50 wt. % solution of 5 mM TeO_2 and 2 M H_2SO_4. a). end on view of pores, b). side view of pores.

Table 3.2: Comparison of H_I-eTe and H_I-ePt film features.

	H_I-eTe templated from $C_{16}EO_8$	H_I-ePt templated from $C_{16}EO_8$
Density (ρ) / g cm^{-3}	6.24	21.4
Pore radius (r) / nm	1.5	1.5
Repeat distance (a) / nm	6.5	5.0
Effective volume %	80.4	77.3
Surface area (Theoretical) / m^2 g^{-1}	52	13

3.6 CONCLUSIONS

The results obtained for nanostructured mesoporous thin films of tellurium highlight that liquid crystal templating offers a generic route for the production of metalloid. High quality and well adherent films of H_I-eTe were grown at potentials of -0.2 V and -0.5 V *vs.* SCE on gold and ITO substrates, respectively.

The results obtained for the cyclic voltammetry in the liquid crystal phase indicate that although tellurium electrochemistry is sensitive to the nature of the substrate (metallic Au or semiconducting ITO) similarities were also evident. In both cases a large negative overpotential was required to promote nucleation and hence deposition. Tellurium underpotential deposition was an apparent feature in the cyclic voltammograms on both substrates.

The cyclic voltammograms for the aqueous phase and liquid crystal phase deposition showed large differences in the current densities at the same electrode potentials. The current densities were 100 times greater with the aqueous phase depositions, suggesting lower diffusion coefficients in the hexagonal liquid crystal phase due to the increased viscosities. With regards to the film morphology, improvements were observed with the flatness of the films. A reduction of the current density led to a flatter films.

The films were successfully characterised by SEM, EDX, FE-SEM, TEM and XRD. The nanostructure within the deposited tellurium films was confirmed by low angle XRD and TEM; evidencing a pore size of 6.4 nm and 5.8 nm, respectively. Since the mesopore diameters and the topology of the nanoarchitecture are under direct experimental control, this novel approach to nanostructured semiconductors affords unique systems in which the relationships between nanoarchitecture and quantum size effects can be explored.

The fabrication of mesoporous tellurium films represents an intial step forward towards the fabrication of type II–VI semiconductors such as CdTe which will be discussed in chapter 4.

3.7 REFERENCES

1. J. M. Feliu, M. J. Llorca, R. Gomez, A. Aldaz, *Surface Science* **297**, 209 (1993).
2. N. Takeuchi, *Surface Science Letters* **426**, L433 (1999).
3. F. Jackson, Berlouis, Rocabois, *Journal of Crystal Growth* **159**, 200 (1996).
4. S. K. Das, G. C. Morris, *Solar Energy Materials and Solar Cells* **28**, 305 (1993).
5. B. B. Bozzini, M. A. Cavallotti, *Thin Solid Films* **361-362**, 388 (2000).
6. D. Kraft, A. Thissen, J. Broetz, S. Flege, M. Campo, A. Klein, W. Jaegermann, *94* **94**, 3589 (2003).
7. X. R. Wang, Z. K. Tang, W. K. Ge, *Physica B* **271**, 386 (1999).
8. K. Jain, P. K. Singh, S. T. Laxmikumar, *Indian Journal of Physics and Proceedings of the Indian Association for the Cultivation of Science-Part A* **78A**, 261 (2004).
9. D. Woo, S. Choi, D. Hun, H. Kang, S. Park, *Jorunal of Physical Chemistry and Chemical Physics* **3**, 3382 (2001).
10. M. Asobe, *Optical fibre technology* **3**, 142 (1997).
11. D. Arivuoli, *Journal of Physics* **57**, 871 (2001).
12. I. Yagi, J. M. Lantz, S. Nakabayashi, R. M. Corn, K. Uosaki, *Journal of Electroanalytical Chemistry* **401**, 95 (1996).
13. F. Kadirgan, S. Kutun, S. Suzer, *Annali di Chimica* **88**, 705 (1998).
14. T. Montiel-Santillan, O. Solorza-Feria, H. Sanchez-Soriano, *Journal of Solid State Electrochemistry* **6**, 433 (2002).
15. T. Montiel-Santillan, O. Solorza-Feria, H. Sanchez-Soriano, *International Journal of Hydrogen Energy* **27**, 461 (2002).
16. T. A. Sorenson, K. Varazo, D. W. Suggs, J. L. Stickney, *Surface Science* **470**, 197 (2001).
17. S. Webster, S. Dennison, *Journal of Electroanalytical Chemistry* **314**, 207 (1997).
18. G. Maurin, D. Pottier, *Journal of Materials Science Letters* **6**, 817 (1987).
19. V. M. Bigelis B. G. Skorodumov, G. N. Kim, I. I. Trinkin, V. N. Kadushkin, V. G. Ulanov, L. V. Navalikhin; O. A. Abrarov, P. K. Khabibullaev, *Elektrokhimiya* **20**, 384 (1984).
20. J. de Becdelievre, A. M. de Becdelievre, M. J. Barbier, *Mat. Res. Bull* **5**, 73 (1970).
21. I. A. Alekperov, F. S. Novruzova, *Elektrokhimiya* **5**, 97 (1969).
22. D. W. Suggs, J. L. Stickney, *Journal of Physical Chemistry* **95**, 10056 (1991).
23. T. Traore, R. Modolo, O. Vittori, *Electrochemica Acta* **33**, 991 (1988).
24. E. Mori, C. K. Baker, J. R. Renolds, J. Rajeshwar, *Journal of Electroanalytical Chemistry* **252**, 441 (1988).
25. R. Diaz, S. Vincente, J. M. Merino, F. Rueda, P. Ocon, P. Herrasti, *Journal of materials chemistry* **10**, 1623 (2000).
26. T. A. Sorenson, D. W. Suggs, I. Nandhakumar, J. L. Stickney, *Journal of Electroanalytical Chemistry* **467**, 270 (1999).
27. N. Ikemiya, D. Iwai, K. Yamada, R. Vidu, S. Hara, *Surface Science* **369**, 199 (1996).
28. S. Dennison, S. Webster, *Journal of Electroanalytical Chemistry* **333**, 287 (1992).
29. J. M. Rosamilia, B. Miller, *Journal of Electroanalytical Chemistry*, 261 (1986).
30. I. Nandhakumar, PhD, Southampton (1999).

31. Y. Sugimoto, PhD, Southampton University (1991).
32. E. A. Meulenkamp, L. M. Peter, *Journal of the Chemical Society, Faraday Trans.* **92** (1996).
33. S. Dennison, S. Webster, *Journal of Electroanalytical Chemistry* **314**, 207 (1991).
34. T. Ishizaki, T. Ohtomo, A. Fuwa, *Journal of the Electrochemical Society* **151**, C161 (2004).
35. C. Konigstein, M. Neumann-Spallart, *Journal of the Electrochemical Society* **145** (1998).
36. J. H. Chen, C. C. Wan, *Journal of Electroanalytical Chemistry* **365**, 87 (1994).
37. S. Santucci, S. Di Nardo, L. Lozzi, M. Passacantando, P. Picozzi, *Surface Science* **352-354**, 1027 (1996).
38. D. Pletcher, *Electrochemical Processes* (The Electrochemistry Consultancy, 1991), pp. 63
39. D. J. Mitchell, G. J. T. Tiddy, L. Waring, T. Bostock, M. P. McDonald, *J. Chem. Soc. Faraday Trans. I* **79**, 975 (1983).
40. I. Nandhakumar, PhD, Southampton University (1999).
41. D. M. Kolb, H. in Gerischer, C. W. E. Tobias, *Advances in electrochemistry and electrochemical engineering* (Wiley, New York, 1978), pp. 125.
42. J. M. Elliot, G. S. Attard, P. N. Bartlett, N. R. B. Coleman, A. S. Merckel, J. R. Owen, *Chemistry of Materials* **11**, 3602 (1999).
43. N. R. B. Coleman, PhD, Southampton University (1997).

CHAPTER FOUR:

FABRICATION AND CHARACTERISATION OF NANOSTRUCTURED CADMIUM TELLURIDE

4.1 Introduction

CdTe is a type II-VI semiconductor whose importance has risen in both commercial and academic research fields over the past thirty years (*1-3*). This is due to its use in a range of applications including luminescent displays, transistors, infrared detectors, optical elements and most importantly photovoltaics (PV) (*9-11*). Cadmium telluride's use in photovoltaic and photoelectrochemical (PEC) (*9*) devices is significant due to its direct bandgap of 1.44 eV and high optical absorption coefficient, making it ideally suited as a material in photovoltaics.

The suitability of CdTe as a PV or PEC component is further heightened by the simple production of CdTe in both the p and n type forms. Generally, semiconductors can be doped to produce p-n homojunction solar cells, by doping the lattices near the interface with small concentrations of foreign atoms which act as either electron donors or acceptors (*10*). Also, n- to p-type conversion of CdTe can be achieved by post fabrication thermal annealing in various gaseous environments such as helium, argon and air (*1*). The type conversion can be later verified by measuring the photocurrent response and the degree of recrystallisation (observed by a change in the wide angle XRD spectra). However, the most effective CdTe cells require the fabrication of a heterojunction interface, with cadmium sulfide (CdS) as a thin window layer. Indium tin oxide can be used as a transparent conducting oxide (TCO) and anti-reflection coating.

There are several practical limitations to the use of CdTe in photovoltaic and photoelectrochemical devices such as photosensitivity, electrolyte corrosion and environmental issues. For example, in PEC the solution must be optimized together with the adsorption of ions at semiconductor surfaces in order to suppress photocorrosion (*12*). The future progress of CdTe, as a solar cell component, is clearly uncertain due to the toxic nature of tellurium and in particular cadmium.

Numerous studies (*1, 3, 9, 13-16*) have demonstrated that the electrodeposition of CdTe thin layer films from aqueous solution provides a low-cost, low temperature and large-scale production alternative to the high costs of vacuum-based epitaxial techniques. Electrodeposition can easily control the film thickness by monitoring the amount of charge passed during electrodeposition. For CdTe an additional advantage is the production of n-type and p-type materials by a mere change in the deposition potentials.

The cathodic electrodeposition of CdTe has received more attention than the anodic deposition due to the extensive control over the stoichiometry, and also the ability to produce both n- and p-type CdTe from the same solution. CdTe deposited from alkaline solutions is thought to form powdery deposits. The cathodic electrodeposition of CdTe from aqueous solutions was pioneered by Panicker *et al.* in 1978 (*10*). This was conducted from aqueous solutions containing $CdSO_4$, H_2SO_4 and TeO_2. The deposition of Te is the rate limiting step and promotes the deposition of Cd ,therefore to ensure stoichiometric deposition of Te, low concentrations of its precursor (TeO_2) were used with a large excess of $CdSO_4$.

Although acidic solutions have been employed for the deposition of CdTe Awakura has consistently used basic electrolytes containing ammonia (NH_3) (*17*), ethylenediamine (*18*) also resulting in uniform, near stoichiometric polycrystalline CdTe films (*19*). The particularly low and high pH values required for CdTe deposition has also encouraged the electrodeposition from non-aqueous solutions (*20, 21*). The following reaction mechanism associated with the cathodic electrodeposition of CdTe from aqueous solutions has been proposed: the first step consists of a 4-electron reduction of Te(IV) from $HTeO_2^+$ ions, to Te(0) which results in the deposition of tellurium, reaction 4.1:

$$HTeO_2^+ + 3H^+ + 4e^- \longrightarrow Te + 2H_2O \qquad [4.1]$$

Due to the low solubility of TeO_2 and the need to limit the concentration ratio with respect to cadmium, the Te is limited by mass transport and hence it is a diffusion controlled reaction. During the following step, the electrodeposited tellurium reacts rapidly with the excess of Cd^{2+} ions (the formation of CdTe is promoted by nucleation sites of Te) leading to a thermodynamically stable surface compound (reaction 4.2). Due to the Te promotion of Cd deposition, less negative deposition potentials than the Nernstian standard potential for Cd are required.

$$Cd^{2+} + Te + 2e^{-} \longrightarrow CdTe \qquad [4.2]$$

Previous studies (*3, 9, 10, 22-25*) on the electrodeposition of semiconductor films have shown that careful consideration must be exercised over electrochemical deposition conditions in order to produce highly ordered films suitable for practical applications. For example, the stoichiometry in CdTe films is controlled by factors such as substrate, deposition potential, current density, and electrolyte constituent concentration ratios (*26-29*). But most importantly it is determined by the relative rates of deposition of the two deposited elements. Both rates must be equal for producing stoichiometric films. Stoichiometric films of CdTe on CdS can be produced using potentiostatic growth at potentials slightly positive of the equilibrium potential for bulk cadmium. Peter and Meulenkamp have clearly stressed the importance of the substrate with respect to stoichiometric CdTe films (*28*). Cowache *et al.* demonstrated that sensitized tin oxide can be used to produce stoichiometric high quality films of CdTe optical and structural properties (*25, 30*), because semiconductor substrates provide an epitaxially matched substrate (*25, 30*). However, this thesis will show that stoichiometric H_I-eCdTe can also be obtained on metallic substrates such as gold.

Only a few studies in the literature have reported the electrodeposition of CdTe in aqueous acidic media in the presence of surfactant molecules (*31-33*). For example, Lincot *et al.* (*31*), states that the rate of the electrodeposition of CdTe from acidic aqueous solutions containing its precursor salts is reduced when the surfactant used is at concentrations less than its critical micellar concentration (CMC). We will look at how the surfactant also reduced the rate of deposition.

In the following sections describe the electrodeposition of CdTe on various substrates (gold and ITO) in the presence and absence of a liquid crystalline phase of non-ionic surfactants. In particular we first report the results obtained for non-mesoporous CdTe samples which will then be used in the deposition of mesoporous CdTe. We also describe for the first time the growth of H_I-eCdTe using the TLCT methods on gold and ITO electrode surfaces with a view to using mesoporous CdTe films for photovoltaic applications these films were subsequently grown on ITO electrodes using a citric acid bath. Numerous experiments on the deposition of CdTe were required in order to achieve the correct stoichiometry, which is an important factor for the use of CdTe in photovoltaics. For example, high levels of tellurium lead to electron-hole recombination centres within the CdTe film and controlling the composition of the films is key to obtaining good photoluminescence and photoconductivity. More important to this study is the fact that nanostructured CdTe with one or more critical dimensions in the nanometer range, may possess novel electronic and optical properties in comparison to its non-nanostructured counterparts. Nanostructured CdTe has already been produced in the form of nanowire arrays (*34*) and CdTe nanocrystals (*35*).

4.2 Mesoporous template mixtures for H_I-eCdTe

In Chapter 3 we have seen that the addition of 5 mM tellurium dioxide and 2 M sulfuric acid to various concentrations of $C_{16}EO_8$ did not significantly change the phase diagram of $C_{16}EO_8$/water mixtures. However, it was envisaged that the addition of a second precursor salt at higher concentrations (>5 mM) may alter the phase boundaries. Previous work carried out by Stupp *et. al.* (*36-38*) investigated the effect of different cadmium salt concentrations on the synthesis of nanostructured CdS powders from hexagonal liquid crystal template mixtures created using 50 vol.% oligoethylene oxide (10) oleyl ether [$(EO)_{10}$-oleyl] and 50 vol.% of a cadmium salt solution. The results revealed a variation in the phase transition boundaries as a function of temperature. These transitions were dependent on; the type of cadmium precursor salt (e.g. sulfate or nitrate), its concentration in the liquid crystal template mixture and the number of EO (ethylene oxide) groups in the amphiphile. However, the following section (section 4.2) will examine the effect of the anion type and the concentration of the cadmium precursor salt as a function of temperature. The importance of the cadmium and tellurium precursor salt concentrations will be highlighted in section 4.3, where the electrodeposition of stoichiometric CdTe is shown to be controlled by the Cd:Te ratio at a given electrode potential.

4.2.1 The effect of cadmium precursor salts on the isotropisation temperatures of $C_{16}EO_8$ template mixtures

A study by Stupp *et. al.* (37) suggests that exceeding a concentration of 0.1 M, of a cadmium precursor salt (e.g. cadmium sulfate, perchlorate, acetate and nitrate) in a liquid crystal template mixture could cause serious degradation of a non-ionic mesophase structure at various concentrations, causing phase separation and a reduction in the isotropisation temperature. This is also described as a change from a birefringent liquid crystal material to a non-birefringent liquid crystal mixture. Figure 4.1 shows the isotropisation temperatures determined for the hexagonal to lamellar mesophase transition for liquid crystal template mixtures containing 50 wt.% $C_{16}EO_8$ and 50 wt.% of various solutions containing 0.01 M, 0.05 M or 0.1 M of cadmium acetate, cadmium nitrate, cadmium perchlorate and cadmium sulfate.

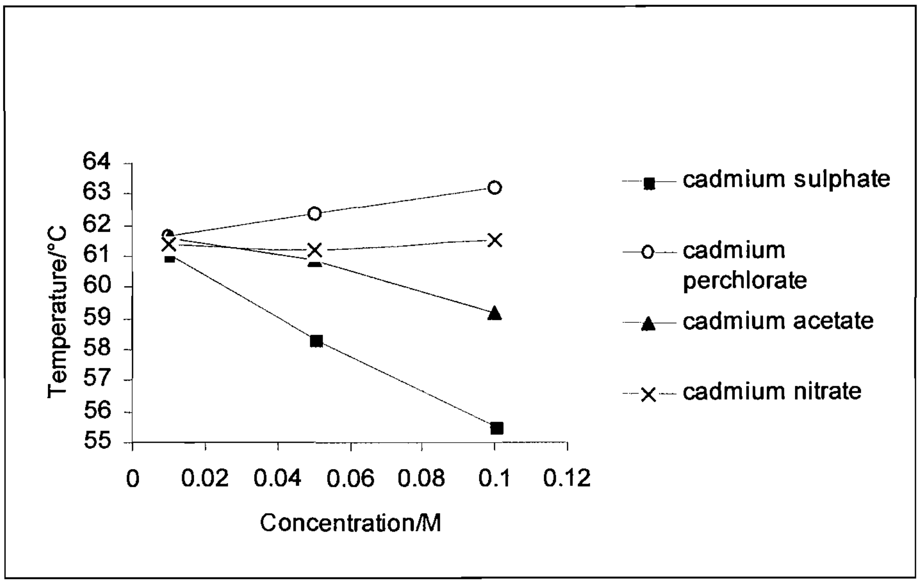

Figure 4.1: The isotropisation temperatures determined for hexagonal liquid crystal mesophases of 50 wt.% $C_{16}EO_8$ and 50 wt.% of solutions containing 0.01 M, 0.05 M and 0.1 M concentrations of various cadmium salts.

The addition of cadmium nitrate shows an almost negligible effect to the isotropisation temperatures over this concentration range. The isotropisation temperatures of liquid crystal mixtures in the presence of the various types of cadmium salts remained at an almost constant value of 61.5 °C, which is equivalent to that of the undoped mesophase. The isotropisation temperatures for cadmium acetate and sulfate based liquid crystal mesophases decreased by approximately 2 and 5 °C, respectively over the 0.01 to 0.1 M concentration range. When using cadmium perchlorate solutions and $C_{16}EO_8$ the isotropisation temperature increased by approximately 1 °C.

On the basis of these results one can infer that low concentrations (0.01 M) of sulfate, acetate, nitrate and perchlorate anions have little effect on the isotropisation temperatures for hexagonal template mixtures containing 50 wt.% $C_{16}EO_8$. All four of the cadmium salts showed less than a 1 °C deviation from the blank water and $C_{16}EO_8$ hexagonal mesophase. Increasing the concentrations to 0.1 M of the cadmium precursor salts causes a greater variation in the isotropisation temperature. The cadmium sulfate mesophase (at 0.1 M) showed a decrease of 5.5 °C over the concentration range, while the cadmium perchlorate increased by mesophase increased by 2.2 °C. (This is also noted by a difference of 7.7 °C between the perchlorate and the sulfate-doped mesophases). POM showed that even at a concentration of 0.1 M the addition of cadmium nitrate did not appear to disrupt the isotropisation temperature of the liquid crystal hexagonal phase. At 0.1 M, the cadmium acetate template mixture resulted in a slight reduction in the isotropisation temperature suggesting a slight destabilisation of the phase. Using 0.1 M cadmium perchlorate, the mesophases showed elevated isotropisation temperatures suggesting phase stabilization. Finally, a significant disruption of the mesophase occurs in the presence of the sulfate anion at 0.1 M. It does suggest that the sulfate anion acts as a phase destabilisation agent in liquid crystals. This is a less significant decrease (only 5.5 °C) than that observed with oligoethylene oxide (10) oleyl ether and the cadmium sulfate anion at the same concentration (7 °C) used by Stupp (*37*). The oligoethylene oxide (10) oleyl ether surfactant appears to be more susceptible to anion effects than $C_{16}EO_8$. This indicates that the degree of disruption is also dependant on the structure of the surfactant in terms of the EO chain length, however this is beyond the scope of this thesis. It can be concluded that the type of cadmium salt must be taken into consideration at concentrations >0.01 M.

4.2.2 The anion effect: conclusions and explanations

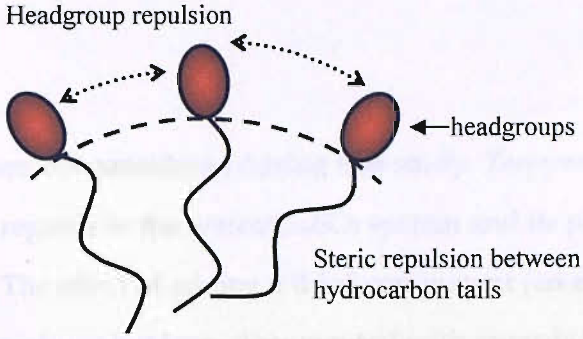

Diagram 4.1: Headgroup repulsion in ionic surfactant/water micellar systems

In order to explain the variation in isotropisation temperatures observed in section 4.2.1 we need to understand the various interactions that can occur between surfactant molecules as a function of the surfactant chain length and the type/size of the headgroup as illustrated in Diagram 4.1. Cetyl tetraammonium bromide CTAB, a cationic surfactant, is taken into consideration in the first instance. The positively charged ionic headgroups of the surfactant repel each other, resulting in surfactant aggregates with a high positive mean curvature where the headgroups become well-spaced in contrast to the hydrocarbon tails (diagram 4.1). Consequently, the hexagonal configuration of the surfactant molecules promote the curved (*39*), and not flatter structures.

Non-ionic surfactant systems such as $C_{16}EO_8$ possess no charged headgroups, and therefore have lower head group repulsion. Modifications to the structure by external factors pH and temperature are subtle by comparison. Therefore, the effect of the phase behaviour is less easily explained. It is clear that micellar formation is sensitive to external factors of:

(a). pH
(b). temperature
(c). pressure
(d). electrolyte

Pressure considerations are not considered during this study. Temperature effects have been clearly shown with regards to the water/$C_{16}EO_8$ system and its phase diagram (chapter 3, section 3.2.2). The effect of adding a third component (an electrolyte) to a binary water/surfactant mixtures has been documented with regards to the CMC and micellar formation (*40-42*), although research describing the effect of electrolytes on the lamellar, cubic and hexagonal phases of non-ionic surfactant is less documented. Small concentrations of added 'impurities' (electrolytes) are known to reduce the isotropisation temperature of the liquid crystal template mixture without altering the mesophase type (e.g. hexagonal, lamellar) (*43*). This was true for tellurium dioxide at a concentration of 5 mM, as was the case for concentrations of ≤0.01 M Cd^{2+}. It has been previously established (*44*) that when a parameter such as temperature, pH and the electrolyte within the system is modified the solvent-PEO interactions are affected. For example, an elevation in temperature at 50 wt.% of a surfactant in water causes a reduction in solubility, leading to dehydration at the headgroup-water interface and movement from the H_I to L_I mesophase. This was examined by means of a phase diagram in chapter 3. Also the addition of a salt/electrolyte can act as a dehydration or hydration agent to the micellar structures present at the micellar interface reducing the solubility of the micellar structures and leading to salting out (dehydration) or salting

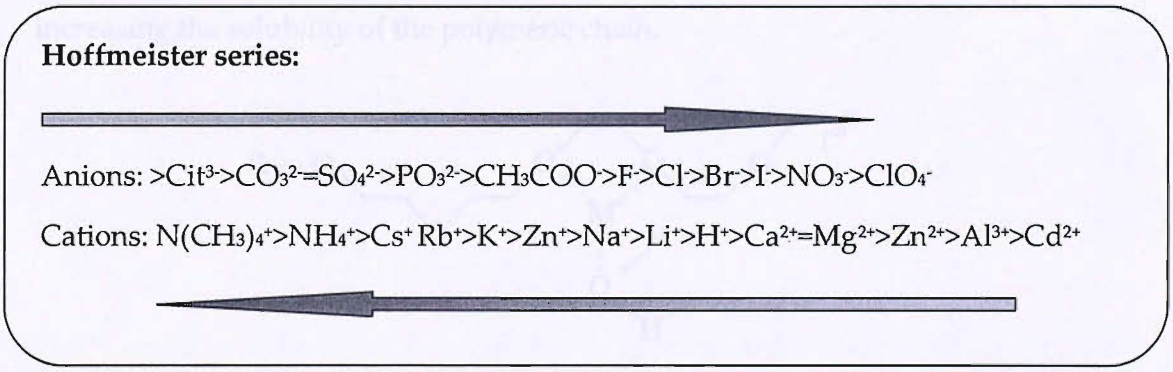

Hoffmeister series:

Anions: $>Cit^{3-}>CO_3^{2-}=SO_4^{2-}>PO_3^{2-}>CH_3COO^{-}>F^{-}>Cl^{-}>Br^{-}>I^{-}>NO_3^{-}>ClO_4^{-}$

Cations: $N(CH_3)_4^{+}>NH_4^{+}>Cs^{+}\ Rb^{+}>K^{+}>Zn^{+}>Na^{+}>Li^{+}>H^{+}>Ca^{2+}=Mg^{2+}>Zn^{2+}>Al^{3+}>Cd^{2+}$

Figure 4.12: Hoffmeister series: arrows indicate the direction of increasing the ions ability to act as dehydration agent.

in (hydration) (*40*). Again this can cause phase boundary modifications with the chain length increased or decreased, salting in/salting out respectively.

The effects of charged species from electrolyte solutions can be ranked according to their interactions with water and/or macromolecules. The ranking system is called the Hoffmeister series shown in figure 4.12. The ranking is the order for solutes at a constant ionic strength to act as a hydrating agent. The direction of the arrows indicates increasing hydration potential. H^+ is more strongly hydrating than either the Cd^{2+} or the Zn^{2+}. The effectiveness to act as a hydration (or dehydration) agent from the PEO head groups is associated with the ionic radius of the anion e.g. as the ionic radii increases the isotropisation temperature decreases. Despite the supporting confirmation for salting out/in by the Hoffmeister series, one should note that this cannot provide conclusive evidence.

The cation on the other hand forms complexes with the PEO head groups. Evidence for the interaction of ions (i.e. Co^{2+}, Cd^{2+}, Zn^{2+}) with non-ionic surfactant headgroups has been given in previous studies (*45*). The mechanism by which this occurs can be seen in diagram 4.2. The cation, in this case Cd^{2+} or Te^{4+}, may forms bonds with the oxygen atoms in the EO part of the chain. This raises the isotropisation temperatures by increasing the solubility of the polymeric chain.

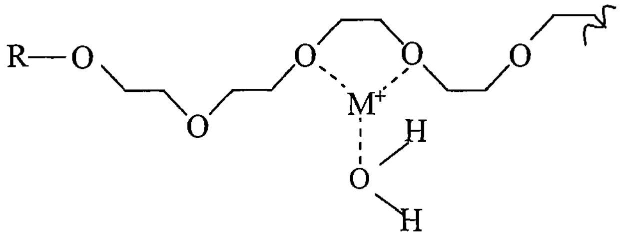

Diagram 4.2: One possible formation for the cation interations (complexation) in $C_{16}EO_8$.

There has been a noted effect of metal cations on PEO templates (*46*). Metal ions in the mixtures interact with the ethylene oxide functions. It has been previously shown that Na^+, K^+, NH_4^+, Ca^+, Li^+, Mg^{2+} and first row transition metal ions have also been known to strongly interact. This suggests that both Te and Cd have interactions with PEO headgroups, but this only becomes apparent at >0.01 M concentrations.

4.2.3 Cadmium salt induced $C_{16}EO_8$ mesophase disruption

Section 4.21 discussed the effect of various types of cadmium anions on the hexagonal phase boundaries of $C_{16}EO_8$. Assigning the identity of the micellar phase at 50 wt.% is possible by the observed POM textures, but it does not provide evidence for the extent of long range ordering within the liquid crystalline phase. Low angle XRD is used to identify the characteristic *d*-spacing of the amphiphiles. As well as being used to further corroborate the type of mesophase, it can also be used to indicate the extent of the ordering. Low angle XRD was used to examine the long range periodicity of the template mixtures. From crystallographic powder data the low angle XRD pattern for a p6mm hexagonal phase will reveal diffraction peaks for the hkl planes <100>, <110>, <200> and <210> in the ratio 1:√3:2:√7 (chapter 2). The presence of high order diffraction peaks (e.g. d_{200} and d_{210}) indicates long range ordering. Low angle XRD data from a hexagonally ordered mesoporous silica film clearly shows the 100, 110 and the 200 peaks (47) and hexagonal template mixtures containing metal and semiconductor salts like tellurium dioxide (section 3.5), cobalt acetate (7), and hexachloroplatinic acid (43) reveal at least the first two diffraction peaks.

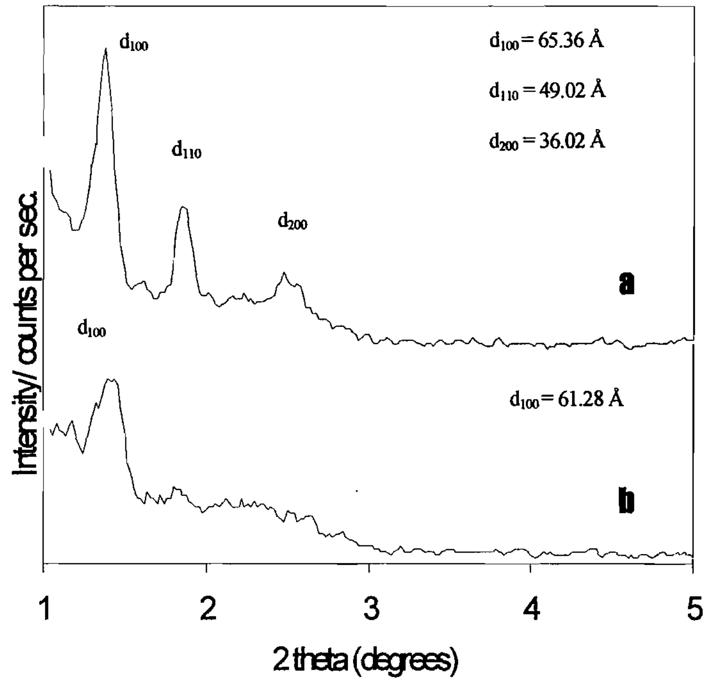

Figure 4.2: Low angle XRD for the hexagonal lyotropic liquid crystalline phase of mixtures consisting of 50 wt. % $C_{16}EO_8$ and a). 50 wt.% of a solution containing 0.01 M $CdSO_4$ and b). 50 wt.% of a solution containing 0.1 M $CdSO_4$.

The electrodeposition of $CdSO_4$ and TeO_2 has been well documented (*9, 10, 22, 23, 25, 34, 48, 49*) and this information can assist in understanding the deposition of CdTe from the domains of a liquid crystal template. The lowest isotropisation temperatures were produced by a hexagonal phase containing 50 wt.% of a 0.1 M solution of cadmium sulfate and 50 wt%. $C_{16}EO_8$. Figure 4.2 shows the low-angle XRD pattern for a hexagonal template mixture containing 50 wt.% 0.01 M cadmium sulfate and 50 wt.% $C_{16}EO_8$. Three distinct peaks can be observed at 1.35, 1.80 and 2.45 °(2θ), corresponding to a lattice parameter of 65.4, 49.0 and 36.0 Å, respectively. The peak positioning ratio is similar to the ratio of 1:√2:3 which is representative of hexagonal p6mm structuring (international tables of crystallography). The existence of the d_{200} peak suggests a high degree of structuring. In TLCT, the d_{100} peak and occasionally another high order peak (the d_{110} or the d_{200}) is observed in the liquid crystal template mixture, depending on the concentration of the precursor salt (*7*). The effect of increasing the $CdSO_4$ concentration from 0.01 M to 0.1 M can be seen in figure 4.2b.

The d_{100} peak appears at 1.44 ° (2θ) corresponding to a lattice parameter of 61.3 Å, however it is less clearly defined than in figure 4.2a. An unresolved area between 1.5 and 3 (2θ) is also observed, indicating the d_{110} and the d_{200} peaks. This observation is an effect of the increase in concentration from 0.01 M to 0.1 M cadmium sulfate. At 0.1 M the disruption of the hexagonal phase is so great that a collapse of the d_{110} and d_{200} diffraction peaks occurs (figure 4.2b). The observed XRD diffractions patterns is are in agreement with the result obtained from the isotropisation experiments (section 4.2.1) in that increasing the concentration of cadmium sulfate ions from 0.01 to 0.1 has a detrimental effect on the structure of the mesophase and on the long range periodicity of the mesophase.

4.2.4 Ionic doping summary

From the POM and XRD data it can be concluded that the mesophase is sensitive to the nature and the concentration of the cadmium precursor salt which can affect the stability and the long range ordering of the surfactant in the liquid crystalline mesophase. This poses a problem for the deposition of H_I-eCdTe using cadmium salts. Low concentrations (≤0.01 M) give long range ordering throughout the template mixture, but as will be shown later, will result in longer deposition times. High concentrations (<0.1 M) result in reduced mesophase ordering, but may provide higher deposition rates (*1*). Therefore there will be a trade-off between the cadmium salt concentrations that can be used for carrying out electrodeposition of CdTe from liquid crystal template mixtures and the deposition times.

Although cadmium sulfate has been proven to be detrimental to the mesoporous phase at higher concentrations, POM morphologies and XRD patterns provide evidence in the form of peak patterns indicative of hexagonal phase structuring at low concentrations. The perchlorate salt was also observed to have an elevated isotropisation temperature suggesting an improvement to the mesophase. However, previous research (*38*) suggests that certain cadmium salts do not form mesostructures and this will be taken into account in section 4.3.

4.3 Fabrication of mesoporous stoichiometric cadmium telluride on gold

4.3.1 Cyclic voltammetry

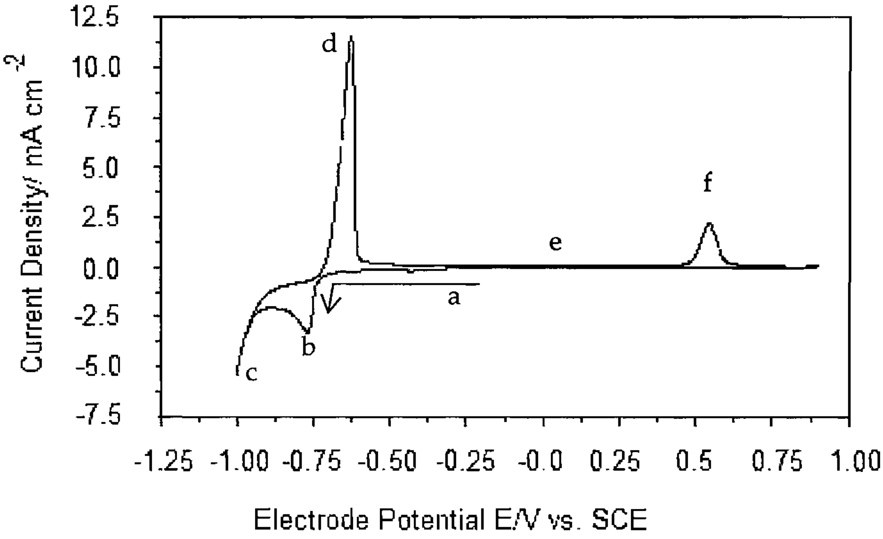

Figure 4.3a: Cyclic voltammogram for the deposition and dissolution of CdTe from hexagonal mesophase containing 50 wt.% of a solution containing 0.15 M cadmium sulfate, 0.005 M tellurium dioxide, 2 M sulphuric acid and 50 wt.% $C_{16}EO_8$. Sweep rate 10 mV s^{-1} and ambient temperature conditions used. The direction of the sweep is shown by the arrow.

For the reasons stated in previous sections, the concentration of the cadmium precursor salt solution was kept at <0.15 M, and the tellurium dioxide concentration remained at 0.005 M. As discussed in section 4.2.1, concentrations of cadmium precursor salts <0.1 M produce stable mesophases with well defined hexagonal phases. Initially, for the deposition of H_I-eCdTe from a liquid crystal have used a 30:1 Cd:Te concentration ratio.

The electrochemistry of a gold electrode immersed in a liquid crystal mixture composed of 50 wt. % of a solution containing 0.15 M $CdSO_4$, 0.005 M TeO_2 and 2 M H_2SO_4 and 50 wt.% $C_{16}EO_8$ is shown in figure 4.3. The cyclic voltammogram starts with a cathodic sweep from an initial potential of 0.0 V *vs.* SCE. There is a gentle increase in the current density at -0.3 V (point [a]). At -0.75 V *vs.* SCE it reaches a potential range which is characterised by a sharp increase in the cathodic current is observed reaching a maximum at -0.775 V *vs.* SCE (point [b]). The rate of deposition then decreases as can be seen by a reduction in the current density, until -0.875 V *vs.* SCE, where the current density rapidly increases (point [c]). The literature (*50*) suggests that the origin of this large increase in current density is due to the electrodeposition of metallic cadmium. However, it has been suggested (*10*) that this may be due to hydrogen evolution. On the reverse scan figure 4.3a (point [d]), the first anodic peak shows that a large amount of the deposited cadmium is oxidised. This may represent the stripping of free cadmium/cadmium oxide, where cadmium has not been deposited as cadmium telluride, or is buried under a layer of CdTe. The anodic peak is followed by a region where no reaction occurs. The selective dissolution of Cd from the CdTe deposit is inhibited by the formation of a Te rich overlayer. Finally, anodic dissolution of Te, and Te from CdTe occurs in the range of 0.4 V to 0.8 V *vs.* SCE.

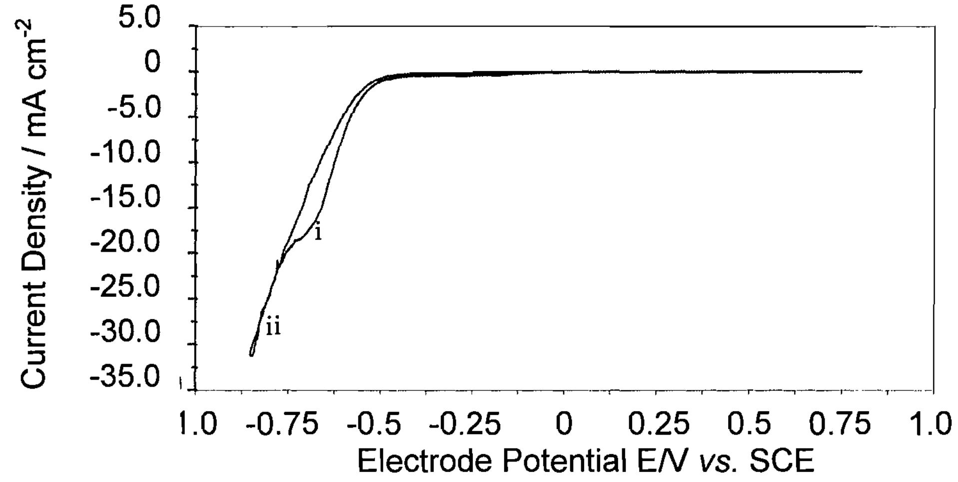

Figure 4.3b: Cyclic voltammograms of a gold electrode immersed in a liquid crystal template mixture containing 50 wt.% 2 M H_2SO_4 and 50wt.% $C_{16}EO_8$.

To assess the origin of the large cathodic increase in current density observed in the electrodeposition of CdTe (figure 4.3a), a subsequent cyclic voltammogram was acquired using a blank solution containing 50 wt.% 2 M sulfuric acid and 50 wt.% $C_{16}EO_8$ (figure 4.3b). There are no voltammetric features in the potential range from 0.8 to -0.4 V *vs.* SCE. On scanning to more negative potentials there is a rapid increase in the current density to -17 mA cm^{-2} at -0.75 V (figure 4.3bi). After a slight reduction in the current density it then increases again to -32.0 mA cm^{-2} at -0.8 V (figure 4.3bii). Due to the absence of cadmium or tellurium from the deposition mixtures it is clear that either O_2 reduction, H_2 evolution or SO_4^{2-} adsorption is responsible for the observed reactions (at i and ii) at the electrode. If this was hydrogen evolution occurs within the potential region of CdTe deposition and poses a problem as it forms bubbles on the electrode surface which results in the productions of pinholes within the CdTe film. In this case it represents a competing reaction to the electroplating of CdTe reducing the current efficiency of the deposition. To suppress H_2 evolution the pH of the solution is increased; however this will be further explored later in this chapter.

The importance of the cyclic voltammogram as a diagnostic tool becomes apparent when stoichiometric CdTe must be achieved. Careful choice of the electrodeposition potential is required to achieve this. Previous research shows that this can be achieved by the correct choice of substrate, potential and concentration ratio (Cd:Te), (*22, 23, 28, 51*) as will be discussed in the next section.

4.3.2 The concentration ratio

The effect of the concentration ratio, R for [Te]/[Cd] in electrolyte solutions containing cadmium sulfate and tellurium dioxide has been previously studied (*28*). High concentrations of cadmium in the electrolyte solution favour Te to CdTe conversion

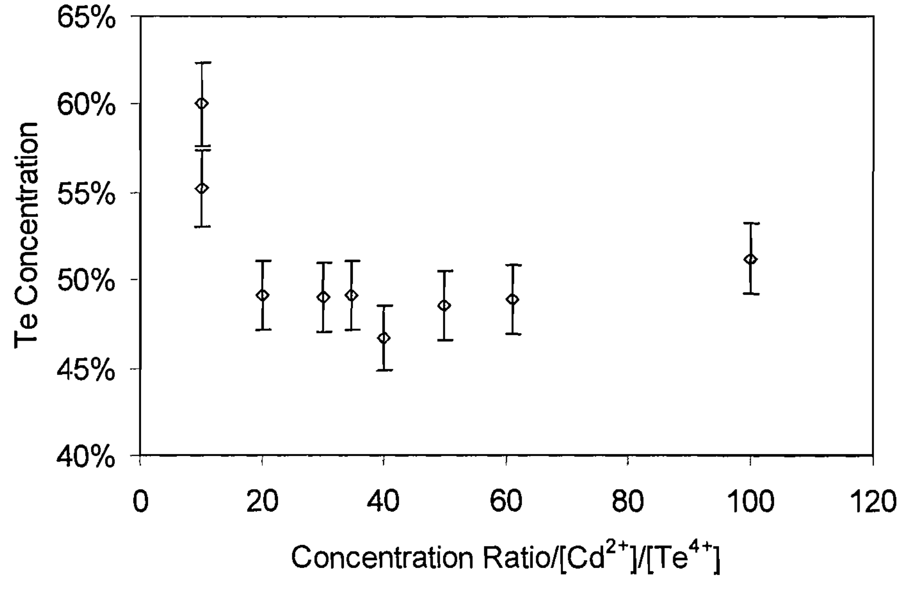

Figure 4.4: EDX measurements of H_I-eCdTe films electrodeposited for 5 hours at a potential of -0.58 V *vs.* SCE from various concentration ratios of precursor salts in the template mixtures.

rather than elemental Te deposition (*28*).

Figure 4.4 shows the EDX determination of the atomic percentages of Te in H_I-eCdTe films grown at -0.58 V *vs.* SCE over the concentration ratio range of R = 10 to 100. The data shows that the composition of the films is stoichiometric (47-49 % cadmium) when $20 \leq R \leq 60$. However, the production of flat, adherent films is considerably better at the lower end of this ratio range where R=30. For example, the electrodeposition of CdTe at R=1000, is not reproducible. The films are extremely non uniform and yield mixed CdTe compositions at various points on the surface throughout. It is interesting to speculate on the nature of this change in R due to the use of liquid crystals. An effect based purely on the diffusion coefficients of both cadmium and tellurium would have simply led to a reduction in the limiting current of CdTe electrodeposition. Instead the Te deposition rate is reduced by the presence of the liquid crystal mixture. This is corrected by effectively increasing the ratio of Te to Cd within the template mixture. The number of sites available for tellurium deposition may also be limited by the presence of $C_{16}EO_8$ surfactant molecules on the electrode surface. This however is speculative as individual surfactant molecules are already incorporated into the hexagonal micellar cylinders. Lincot *et. al.* (*31*) also suggest adsorption on surface sites is only effected at concentrations smaller than the CMC where individual surfactant molecules are free to move.

4.3.3 Electrodeposition potential effects

EDX was used to determine the ratios of Cd to Te in films of H_I-eCdTe electrodeposited at different potentials. Figure 4.5 shows the ratio of Te in H_I-eCdTe films electrodeposited using a concentration ratio of 30:1 Cd:Te in the potential range of -0.75 to -0.4 V *vs.* SCE. At potentials more negative than -0.65 V *vs.* SCE the films contain a mixture of CdTe and Cd and at -0.75 V the Te content is reduced to 9 %. While at potentials more positive than -0.55 V *vs.* SCE the films are only slightly tellurium rich, with an excess of 5-7 %. Therefore, stoichiometric (50±2.3%) deposition of H_I-eCdTe is obtained at potentials between -0.65 and -0.55 V *vs.* SCE. Confirmation for these results comes in the form of UV-Vis spectroscopy (section 4.6) where deviations from stoichiometric films would not produce the expected band gap of 853 nm for CdTe.

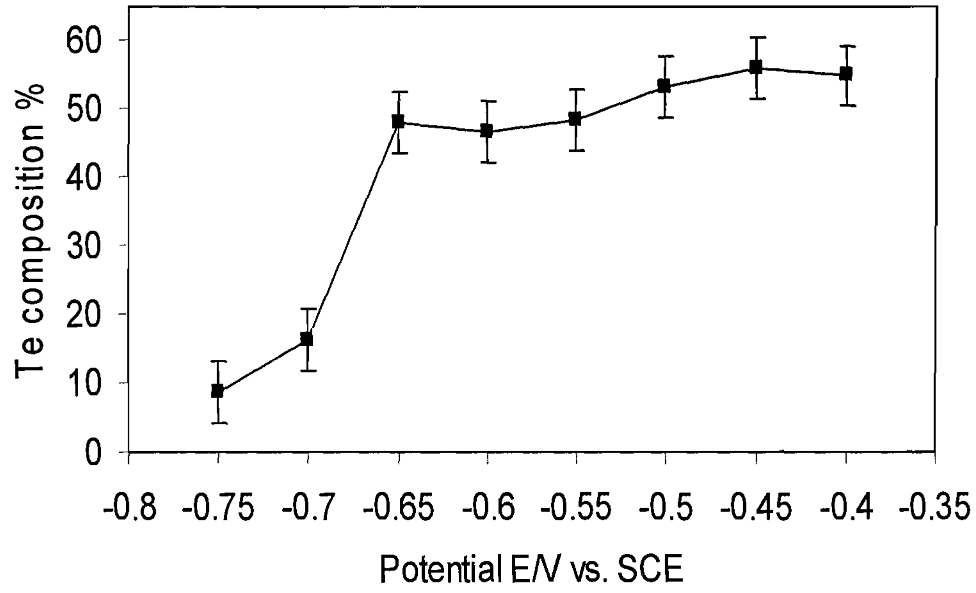

Figure 4.5: EDX measurements taken of a series of H_I-eCdTe films electrodeposited at different potentials using a 50 wt.% solution with a concentration ratio of Cd:Te of 1:30 and 50 wt.% $C_{16}EO_8$.

4.3.4 Deposition time effects

The electrodeposition of CdTe from an aqueous plating bath initially occurs with an underlying tellurium deposit (52). It is unclear how this is affected by the presence of a liquid crystal template mixture. The following results look at the effect of time on the stoichiometry for mesoporous CdTe films. Tellurium is used in low concentrations and its depletion from the plating bath may lead to non-stoichiometric CdTe films as the deposition progresses.

Figure 4.6 shows the tellurium content in H_I-eCdTe films electrodeposited at -0.58 V *vs.* SCE for various deposition times as determined from EDX measurements. The liquid crystal template mixture prepared for the depositions consisted of a 50 wt.% solution of 0.15 M cadmium sulfate, 0.005 M TeO_2 and 2 M H_2SO_4 and 50 wt.% $C_{16}EO_8$. The concentration ratio was 30:1 (cadmium excess). EDX measurements were taken for each H_I-eCdTe films deposited at 3600, 7200, 10800, 18000, 28800, 43200 and 57600 s. Each deposition was carried out using a new liquid crystal template mixture.

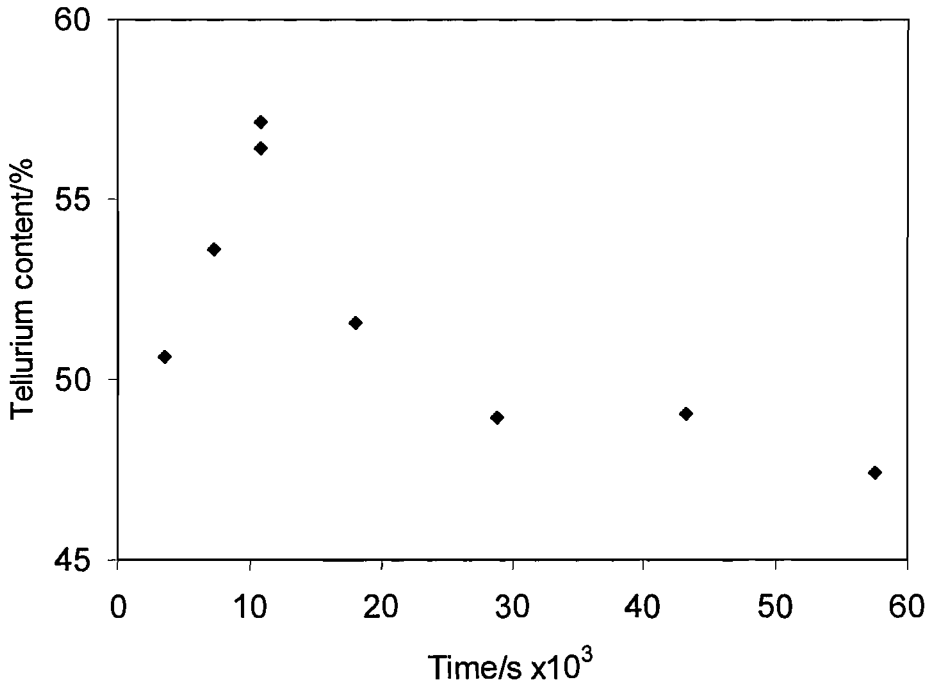

Figure 4.6: The tellurium content % acquired from EDX of H_I-eCdTe films deposited at -0.58 V *vs.* SCE for various times.

After a deposition of 3600 s the tellurium content in the films is 50.5 %. As the deposition time is lengthened the tellurium content increases to 56 % for a deposition of 10800 s. However this is an initial spike and the Te content decreases to a relatively stable value of 49 % before tailing off as expected at even longer deposition times of 57600 s.

The initial maximum in the Te content at 10800 s can be assigned to the formation of an underlying Te layer. In the final stages of deposition the slight decrease in Te content is due to the depletion of Te^{4+} ions from the template mixture over long periods of time (*26*). This may be due to an increase in the resistivity of the CdTe layer. EDX measurements suggest that deposition times between 18000 s and 43200 s can produce H_I-eCdTe films with 49-51 % stoichiometry. These results indicated that no correction to the deposition potential during deposition was required even for the thickest films produced.

4.3.5 Electrodeposition of H_I-eCdTe on gold summary

Attempts were also made to deposit mesoporous CdTe films using other cadmium salts; such as acetate, nitrate, perchlorate, however this was of limited success. Cadmium nitrate and the acetate based mesophases did not produce a film. In part, this is in agreement with previous studies, by Stupp *et. al.* (*36*) which did not produce CdS mesostructures from nitrate based liquid crystal precursor mixtures. Using a cadmium perchlorate electrolyte produced well-structured mesophases as well as adherent and uniform CdTe films, but lacked reproducibility. Therefore, cadmium sulfate based liquid crystal template mixtures were used. Although these templates produced the lowest isotropisation temperatures compared to the other salts, and there was significant disruption to the mesophase at concentrations >0.5 M, the deposition was reproducible under potential and concentration control. The optimum conditions were found to be a concentration ratio of 30:1 (cadmium excess) with a low cadmium sulphate concentration ~0.15 M, a deposition potential between -0.55 V and -0.65 V *vs.* SCE and a deposition duration from 18000 to 43200 seconds.

4.4 Structure and morphology of the electrodeposited film

4.4.1 Wide angle X-ray diffraction XRD

A wide angle XRD pattern for a H_I-eCdTe films electrodeposited at -0.58 V *vs.* SCE from a template mixture consisting of a cadmium and tellurium precursor salt in the ratio of 30:1, on gold electrodes is shown in figure 4.7. EDX showed a stoichiometric ratio of tellurium to cadmium in the film. The most intense peak at 39 ° (2θ) can be attributed to the polycrystalline gold substrate and a further gold peak is observed at 44.0 ° (2θ). The peak at 23.5 ° (2θ) shows that the reflection for CdTe is preferentially oriented along the <111> direction and therefore has a cubic structure. This is in agreement with previous studies reported in the literature (*3, 10, 14, 24, 27, 53*). The position of the <111> CdTe peak in the pattern also matches that of powder diffractograms obtained for CdTe (JCPDS 15-77). Estimates of the grain sizes were obtained from the <111> peak broadening and by applying the Debye-Scherrer equation (chapter 3, equation 3.9). The as-deposited mesoporous CdTe film has a grain

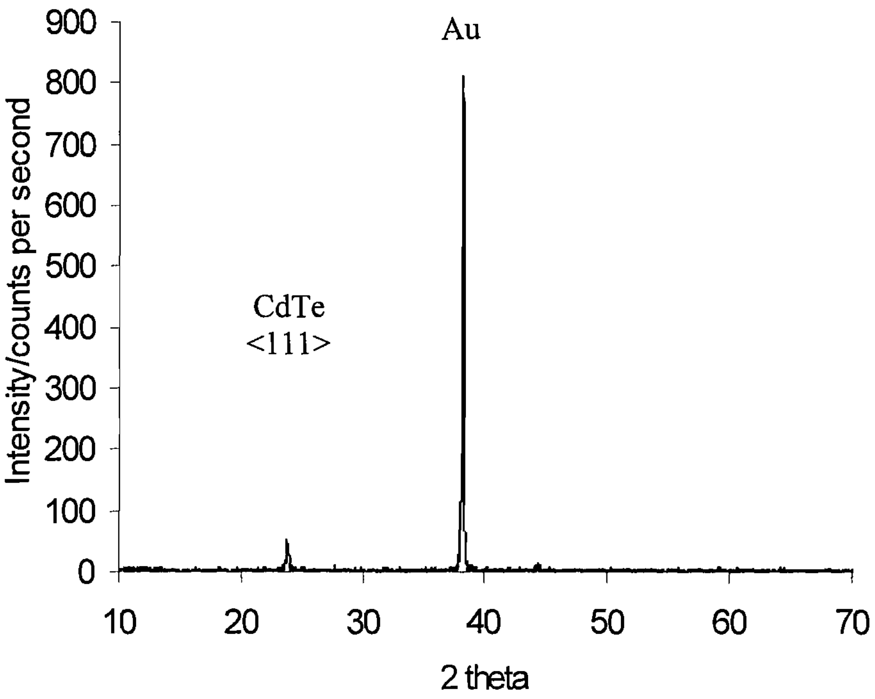

Figure 4.7a: Wide angle XRD for a). a H_I-eCdTe film on Au, electrodeposited using a plating bath containing 50wt.% of a solution containing 0.15 M $CdSO_4$, 0.005 M TeO_2 and 2 M H_2SO_4, and 50wt.% $C_{16}EO_8$.

size of ~5.6 nm. Panicker *et. al.* reported CdTe crystallite sizes in the range of 50 to 1000 nm crystallites is a result of the nanostructuring in the films. Average grain sizes can be expected to be similar in size to the wall thickness of the pores within the films which was determined by TEM. This was determined to be 3.0±0.2 nm (section 3.5.2). Finally, the XRD diffraction measurements did not give rise to peaks which can be assigned to elemental for Cd or Te, suggesting that all the Cd and Te is deposited in the form of CdTe.

The efficiency of photovoltaic cells is improved by smaller grain sizes of CdTe (*10*). These results highlight the possibility of embedding mesoporosity in to CdTe films for photovoltaic cells.

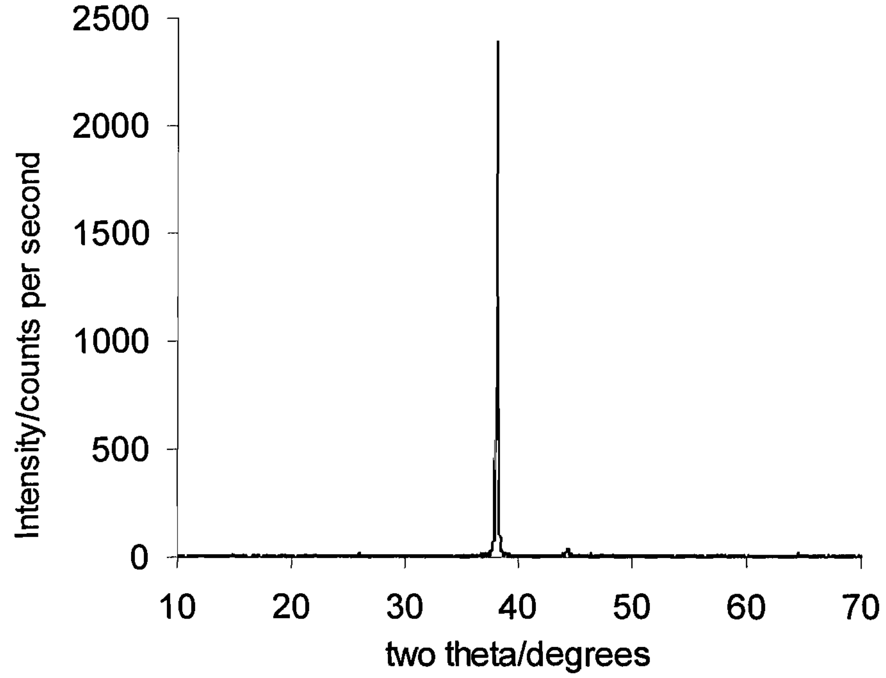

Figure 4.7b: Wide angle XRD for a 250 nm gold electrode.

4.4.2 Annealing H_I-eCdTe on gold

Figure 4.8 shows the X-ray diffraction patterns for the H_I-eCdTe films deposited at -0.58 V *vs.* SCE under ambient temperature conditions. Annealing is a common post deposition process for improving the crystallinity of the film, and the optoelectronic properties of the material (54). The as-deposited film (figure 4.7) underwent thermal treatment in oxygen at 400 °C for one hour. The wide angle XRD results can be seen in figure 4.8. The wide-angle XRD pattern of the original as-deposited CdTe film has also been included for comparison (figure 4.8a). The film failed to recrystallise during the one hour annealing process (figure 4.8b), therefore another H_I-eCdTe film was annealed for 6 hours under the same conditions (figure 4.8c). There is a slight difference in the peak height ratio. The peak height ratio between the CdTe <111> peak at 23.8 °, and the gold at 38.8°was 1:4.3, respectively, however after for six hours annealing the film the ratio increased to 1:6.44 and then to 1:7.9. This may suggests a

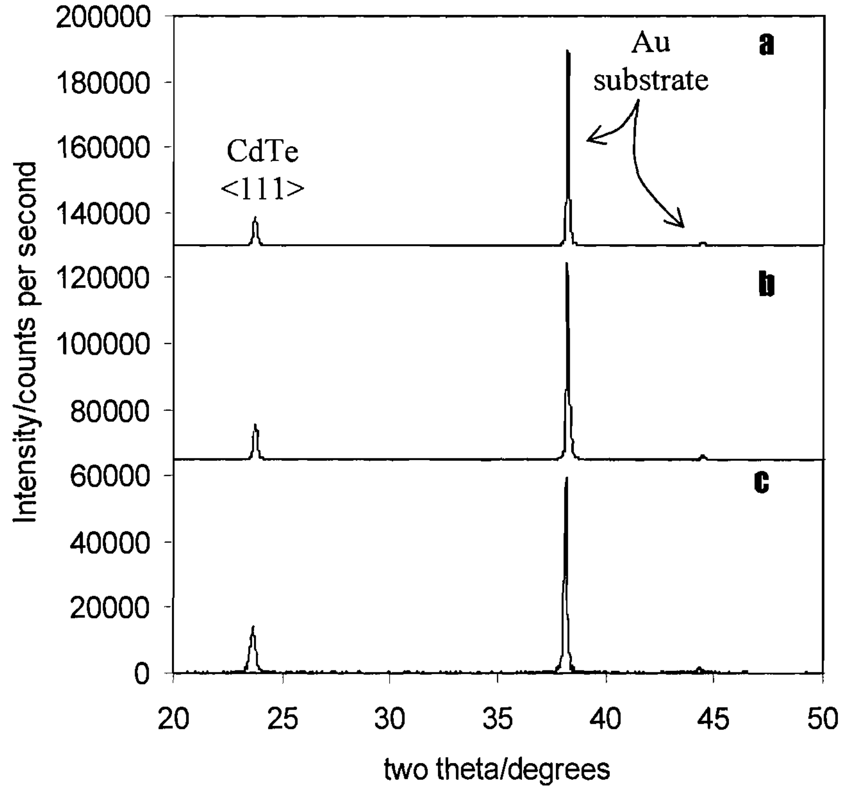

Figure 4.8: X-ray diffraction patterns of films deposited on Au electrodes from hexagonal mesophases containing 50 wt.% of a solution containing 0.15 M cadmium sulfate, 0.005 M tellurium dioxide, 2 M sulphuric acid and 50 wt.% $C_{16}EO_8$ deposited at -0.58 V *vs.* SCE (a). as-deposited film and (b). CdTe film annealed in an oxygen atmosphere at 400 °C for 1 hour (c). 6 hours.

decrease in the H_I-eCdTe present while the Au remains intact. As no other CdTe peaks exist a change in the crystal orientation in the film through annealing cannot be ascertained. The measured crystallite size also changed from 5.6 nm for the as-deposited film to 7.9 nm after subsequent annealing for one hour, but remained the same after 6 hours. Annealing the a different mesoporous CdTe film in Argon was attempted for periods of 1 hour followed by 6 hours, but failed to produce any differences in the wide angle XRD.

The production of a film that retained its mesoporosity after annealing was also unsuccessful. Low angle XRD failed to suggest any mesoporosity, as there were no peaks visible in the spectra. Mesoporous CdTe films electrodeposited on Au exhibit none of the same recrystallisation features as bulk CdTe films on CdS (*30*), or on Au following annealing.

4.4.3 Scanning electron microscopy (SEM)

H_I-eCdTe films electrodeposited on gold on glass substrates at ambient temperatures and a potential of -0.58 V *vs.* SCE were examined by SEM. This technique provides information on the surface morphology of the films. The morphologies of the electrodeposited CdTe films formed by increasing the concentrations of cadmium sulfate and tellurium dioxide with R remaining constant at 30 are shown in figure 4.9. All films were stoichiometric to within ±5%. The SEM images (figure 4.9a-d) show that the surface morphology of the H_I-eCdTe deposits on Au becomes less smooth as the concentration of cadmium sulfate and tellurium dioxide in the template mixture is increased. There is an increase in the nucleation on the surface of the films. What is also apparent is the plateau and craters formed in the films at cadmium sulfate concentrations >0.15 M (figure 4.10a). It has been proposed that the difference in height of these growth areas correlates to the differing orientations of the surfactant micelles in the template mixture. The plateaux and crater edges (indicated by the arrows in figure 4.10c) are where the hexagonal (or vertical) micellar orientations changes as growth around vertically or horizontally positioned micelles may occur at different rates. These results show that using a concentration ratio of R=30 resulted in H_I-eCdTe films that were nearly stoichiometric and that the increased concentration of the cadmium precursor salt reduces the featureless morphology and metallic appearance of the films. The preparation of flat adherent film required a concentration of ≤ 0.15 M $CdSO_4$ and 0.005 M TeO_2.

Concentrations	0.15 M $CdSO_4$/ 0.005 M TeO_2/ 2 M H_2SO_4	0.60 M $CdSO_4$/ 0.02 M TeO_2/ 2 M H_2SO_4	0.90 M $CdSO_4$/ 0.03 M TeO_2/ 2 M H_2SO_4	1.50 M $CdSO_4$/ 0.05 M TeO_2/ 2 M H_2SO_4
Film Thickness/nm	232	350	444	700

Table 4.1: Film thickness measured by SEM of H_I-e CdTe grown using 50wt.% of a electrolyte solution and 50wt.% $C_{16}EO_8$.

Cross-sectional SEM measurements of the film thickness showed that as the concentration of cadmium sulfate and tellurium dioxide increases (R is constant) as did

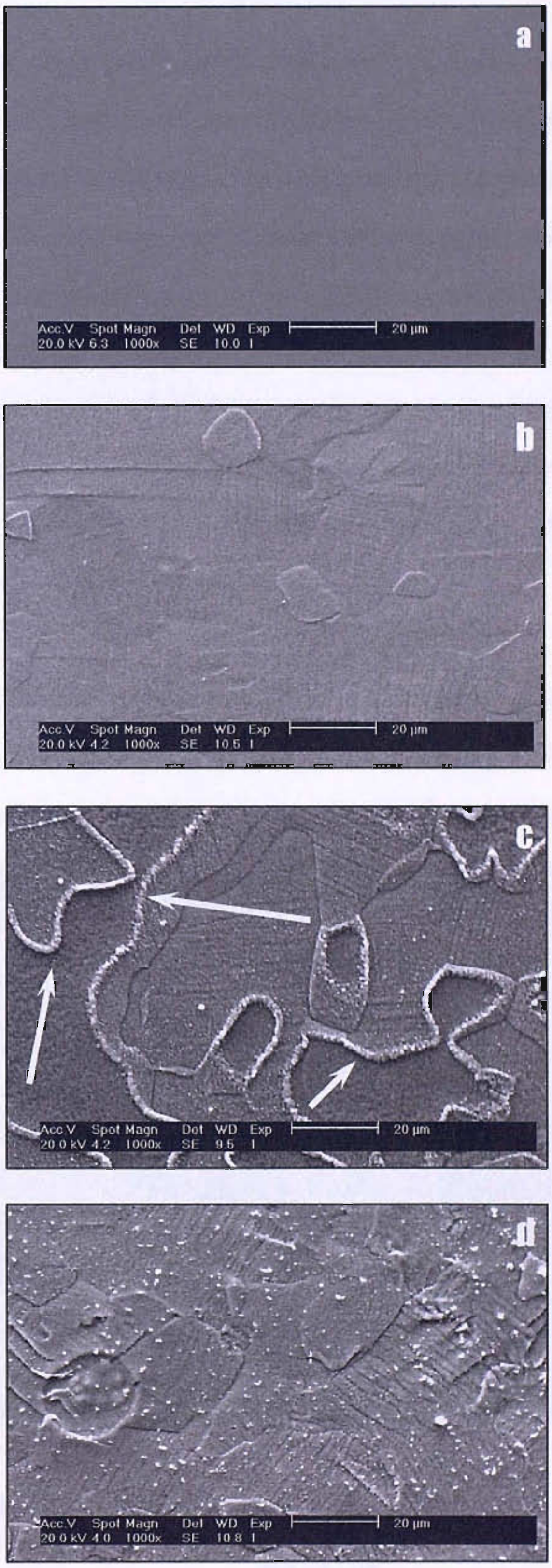

Figure 4.9: SEM images of H_I-e CdTe films electrodeposited on evaporated gold substrate using a hexagonal template mixture containing a concentration ratio R=30 (Cd:Te) with a). 0.15 M, b). 0.6 M, c). 0.9 M and d). 1.5 M cadmium sulphate.

the film thickness for films grown for a duration of 16 hours (table 4.1). The data shows that there is a distinct increase in the growth rate of CdTe at higher concentrations.

Figure 4.9e shows the cross sectional view of a mesoporous CdTe film taken at an angle of 90 °. The film is dense and continuous and can be described as being almost flat and featureless. The observed thickness of the layer was measured to be approximately 250±10 nm (figure 4.8b). The theoretical thickness of the film was calculated to be 1.54 nm. This gave a current efficiency of 17 %. According to Faraday's law, the amount of chemical change produced by electrolysis is proportional to the total amount charge passed in the cell. Faraday's law allows us to determine the thickness of deposited CdTe films. The effective density of H_I-eCdTe is estimated to be 4.68 g cm^{-3} since H_I-eCdTe with a perfect hexagonal nanostructure containing 77.3 % (by volume) CdTe and 22.7 % (by volume) voids.

The film thickness calculated from charge for an ideal hexagonal nanostructure can be compared with the observed film thickness as measured by SEM. It was found that the actual thickness was lower than that the calculated value, and electrodeposition of

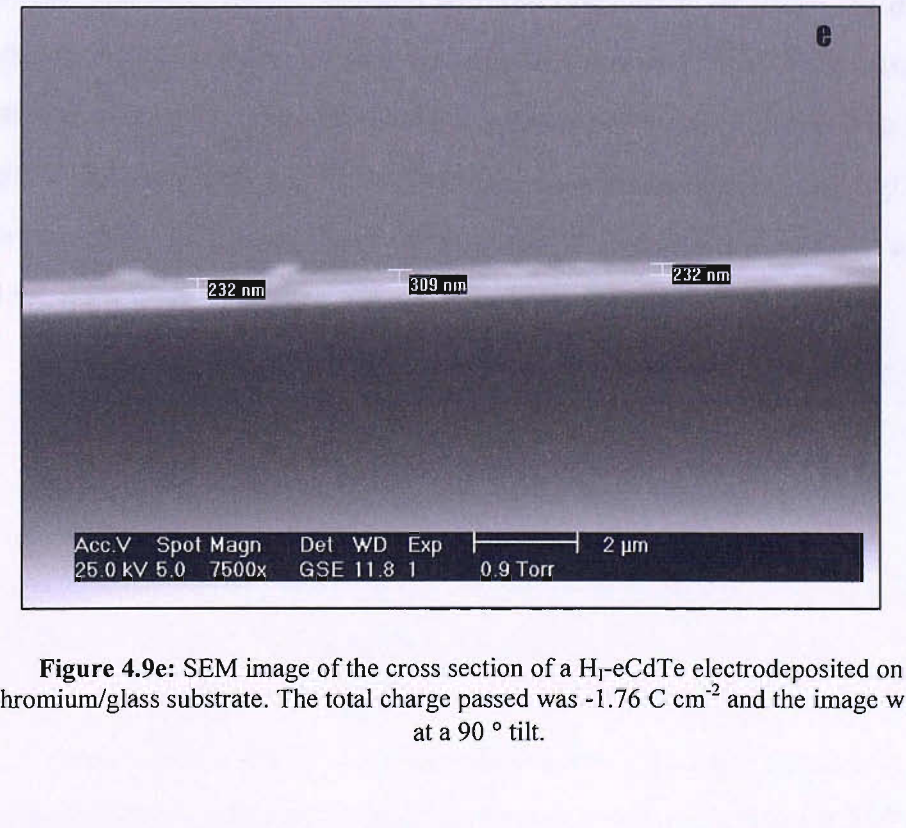

Figure 4.9e: SEM image of the cross section of a H_I-eCdTe electrodeposited on a gold/chromium/glass substrate. The total charge passed was -1.76 C cm^{-2} and the image was obtained at a 90 ° tilt.

CdTe in our system occurred with an efficiency of 16.7 %. This indicated that the efficiency of the CdTe electrodeposition process from a liquid crystal template mixture is extremely low. This may be due to competing reactions such as, cadmium oxide and bulk cadmium formation or hydrogen evolution. Section 4.3 has already highlighted the possibility of hydrogen evolution. In order to minimize the reduction of hydrogen, either a higher pH value electrolyte solution should be employed or electrodeposition should be conducted at more positive potentials. However, increasing the pH limits the solubility of Te species. Recently it has been shown that the solubility of Te species can be increased by the use of a citric acid bath (*55*). Using a citric acid bath, a pH of 4 is the lowest pH reported so far for reasonable deposition rates of tellurium. Prior to this Te deposition was carried out at ~2.5 or less (*28, 51, 56*). Factors affecting the solubility of tellurium will be investigated in section 4.6

4.4.4 Selected area electron diffraction (SAED) and the CdTe lattice using Transmission electron microscopy (TEM)

Figure 4.10a shows a high resolution transmission electron microscope image of a H1-eCdTe lattice. The individual lattice atoms can be discerned with an atom to atom spacing of 0.48±0.04 nm. This is consistent with the zinc blende structure of CdTe The film was grown on an Au substrate and subsequently scraped off for TEM analysis. The high structural quality of the material is confirmed by the lack of stacking faults and microtwin defects which appear as kinks and disruptions in the lattice (*17*). Further confirmation of this comes from wide angle XRD diffraction patterns as shown in figure 4.8.

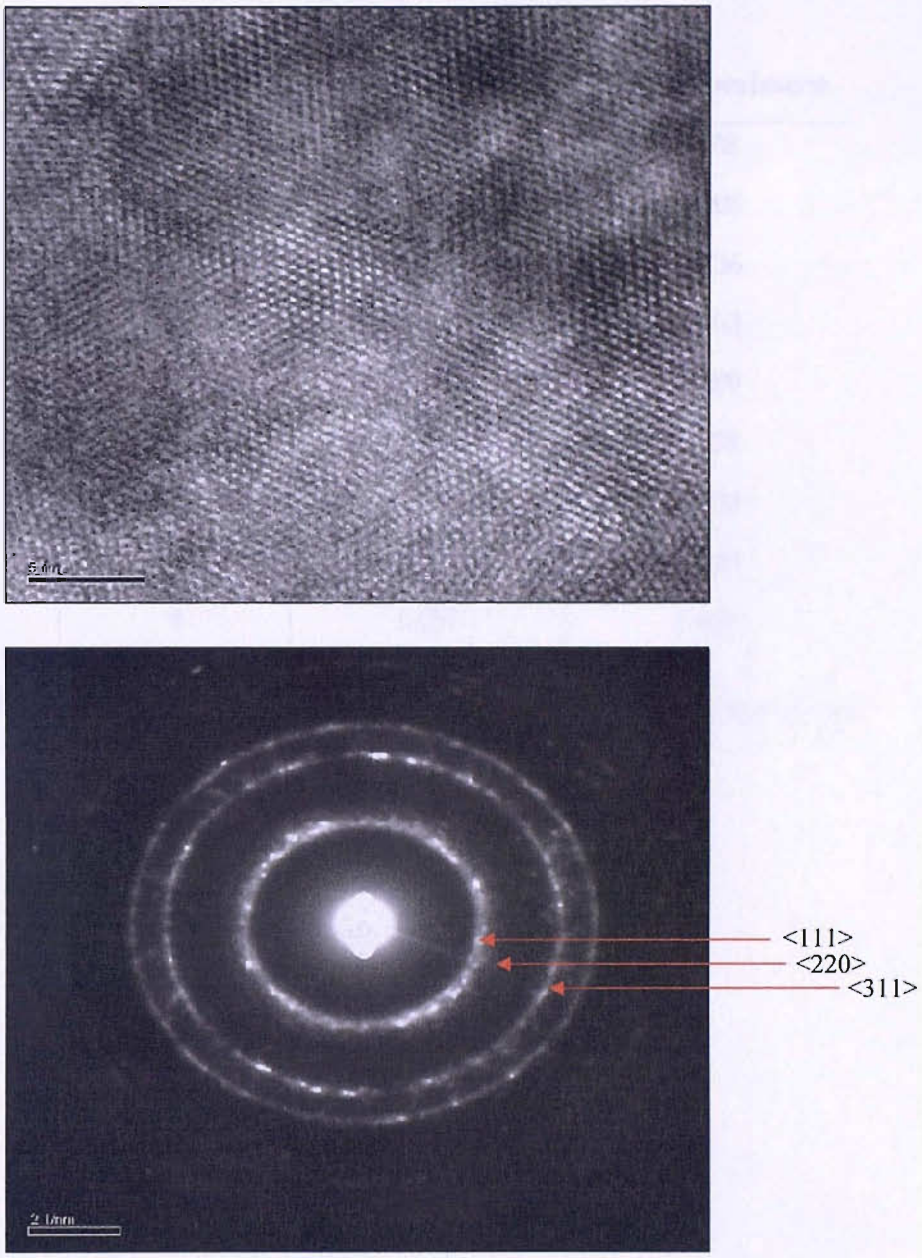

Figure 4.10: a). Transmission electron micrograph of H_I-eCdTe showing the CdTe lattice and b). the SAED patterns for the same H_I-eCdTe electrodeposited at -0.58 V *vs.* SCE.

Selected area electron diffraction (SAED) measurements were employed determine the crystal structure of the deposits. Figure 4.9b depicts a series of rings which imply a polycrystalline deposit. The *d*-spacings for a stoichiometric H_I-eCdTe film are assigned in table 4.1. These values can be compared with the *d*-spacings associated with CdTe powder diffraction patterns (also Table 4.1). There is excellent correlation between both sets of data, however this is not conclusive, as the <200> reflection of the diffraction pattern could not be attributed to a pattern in the H_I-eCdTe film.

Table (hkl)	Rel. intensity	d (Å) Reference	d (Å) Experiment
111	100	3.742	3.78
200	-	-	3.205
220	60	2.29	2.236
311	30	1.954	1.903
400	6	1.619	1.589
331	10	1.488	1.458
422	10	1.323	1.303
511	4	1.247	1.237
531	4	1.095	1.907

Table 4.1: Shows the d-spacing and relative intensity for a H_I-eCdTe film (experiment) and CdTe powder (reference).

4.5 Characterisation of mesoporous H_I-eCdTe on gold

4.5.1 Low angle X-Ray diffraction (XRD)

Initial evidence for the presence of a regular pore structure in the CdTe films is given by low angle XRD. Figure 4.11 shows low angle XRD patterns for both the CdTe liquid crystal template mixture (inset) and the electrodeposited film H_I-eCdTe from this template mixture. The template mixture consisted of the standard 50 wt.% of a solution containing 0.005 M TeO_2, 0.15 M $CdSO_4$ and 2 M H_2SO_4 and 50 wt.% $C_{16}EO_8$.

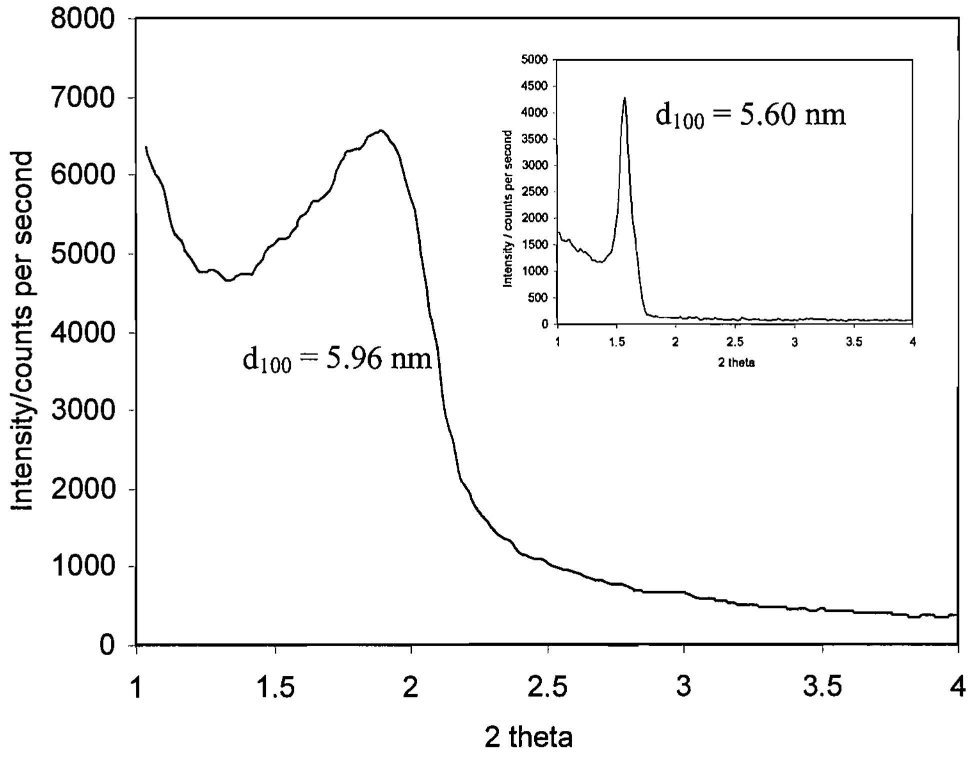

Figure 4.11: Low angle X-ray diffraction pattern of a H_I-e CdTe film deposited at -0.58 V on gold from a liquid crystal template mixture containing 50 wt.% $C_{16}EO_8$ and a 50 wt.% of a solution containing 0.15 M $CdSO_4$, 0.005 M TeO_2 and 2 M H_2SO_4. Inset: template mixture alone.

The diffraction pattern for the liquid crystal (inset) shows a single primary d_{100} reflection with a *d*-spacing of 5.6 nm. This value was calculated by using the Bragg equation given in chapter 2.4.1.2 (equation 2.1). The figure also shows a d_{100} peak for a hexagonal mesoporous CdTe film with a *d*-spacing of 6.0 nm which corresponds to a pore-to-pore distance 6.9 nm. The existence of a d_{100} peak confirms the presence of a hexagonal mesostructure. The peak is broad and suggests that long range periodicity is poor. These results are in good agreement with other electrochemically deposited mesoporous materials. Table 4.2 summarises the lattice parameters and pore-to-pore distances for recently published results on mesoporous materials prepared by true liquid crystal templating.

Table 4.2: Summary of Low angle XRD data obtained using CuK radiation for electrochemically deposited H_I-eSe, H_I-eTe, H_I-e CdTe, H_I-ePb, H_I-eSn, H_I-ePt/Rh, H_I-eCo (*4-8*).

Element/Compound	Lattice parameter/d_{100}-spacing (Å)	Pore-to-pore distance (Å)
H_I-ePt/Rh	60.3	69.6
H_I-ePb	59.0	68.1
H_I-eCo	64.0	73.4
H_I-eSe	58.1	67.1
H_I-e Sn	60.0	69.3
H_I-eTe	55.9	64.5
H_I-eCdTe	59.6	68.9

4.5.2 Transmission electron microscopy (TEM)

Transmission electron microscopy was employed to visualise the mesopores in the H_I-eCdTe films. As shown in figure 4.12, the material prepared exhibits a nanostructure consisting of a hexagonal array of cylindrical pores of uniform diameter which are disposed on a hexagonal lattice. This image shows the TEM image of H_I-eCdTe scraped from the electrode surface with the pores in the end on orientation. Measurements taken from the micrographs indicate an average pore-to-pore distance of 7.0 ±0.2 nm. These values are in good agreement with the low angle XRD results which give a pore to pore distance of 6.9±0.1 nm. These values are also comparable with H_I-ePt (*43*), H_I-eSe (*6*), H_I-eCo (*7*), H_I-eSn (*4*) prepared using a $C_{16}EO_8$ liquid crystal template mixtures.

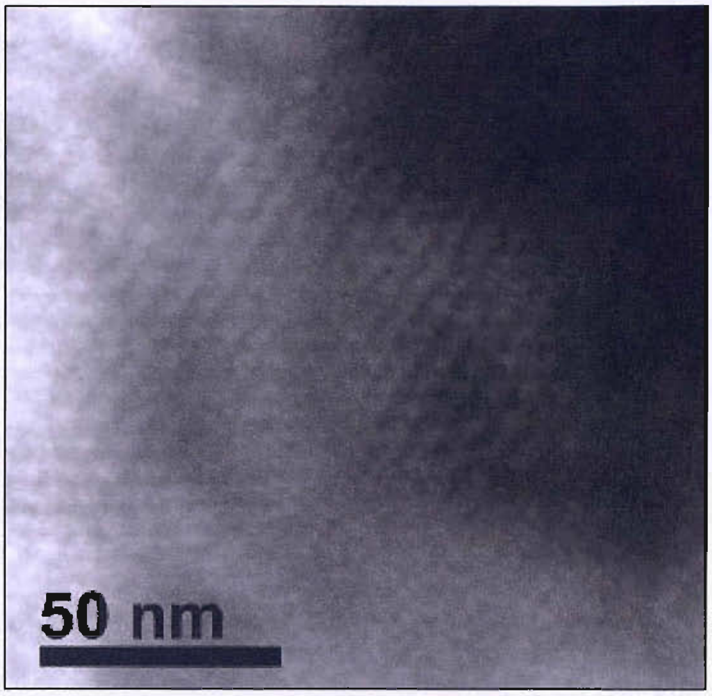

Figure 4.12: Transmission electron micrograph of cadmium tellurium electrodeposited from a mixture containing 50 wt.% of $C_{16}EO_8$ and 50 wt.% of a solution 0.005 M TeO_2, 0.15 M $CdSO_4$ and 2 M H_2SO_4. An end on view of the pore structure is shown.

4.6 Fabrication of mesoporous stoichiometric cadmium telluride on cadmium sulfide using citric acid

The previous chapter has shown that CdTe can be successfully electrodeposited onto Au substrates. Studies have shown that the electrodeposition of CdTe on optically transparent electrodes is important due to their potential use in photovoltaics. CdS provides a wide band gap window layer for solar cells with efficiencies of ~14 % (*57*). Kampmann *et. al.* produced CdTe thin films on chemically bath deposited CdS layers with excellent optical and structural properties and high quantum efficiencies (*30*).

The electrodeposition of CdTe from liquid crystal templates on CdS requires further modification to the deposition conditions found for of CdTe on Au. The strongly acidic nature of the electrolyte solution initially destroyed the CdS surface but the use of a low pH was essential to increase the solubility of Te. Using low concentrations of Te in a liquid crystal solution made deposition difficult and resulted in cadmium rich films, even after modifying the concentration ratio. Therefore this was not an option. The poor solubility of TeO_2 has been a common problem for the electrodeposition of Te species. Recently researchers have found that tellurium can form complexes with citric acid in order to improve its solubility in high pH solutions. The following sections show a possible route to the fabrication of CdTe on CdS from liquid crystal templates using citric acid to improve the solubility of Te in solution.

4.6.1 Phase characterisation

The phase structure of the hexagonal liquid crystalline mixture containing 0.15 M $CdSO_4$, 0.005 M TeO_2, 0.5 M Cit was examined by low angle XRD. Figure 4.13 shows that the liquid crystalline templating mixture exhibits three well-resolved diffraction peaks with *d*-spacings of 5.73, 3.53 and 3.0 nm, respectively. These *d*-spacings are close to the ratio 1: 1/√3:1/2, and are consistent with the (100), (110) and (200) diffraction planes of the hexagonal structure. The result for the d_{100} peak is similar to the peak obtained for the 2 M sulfuric acid template mixture used section 4.1.

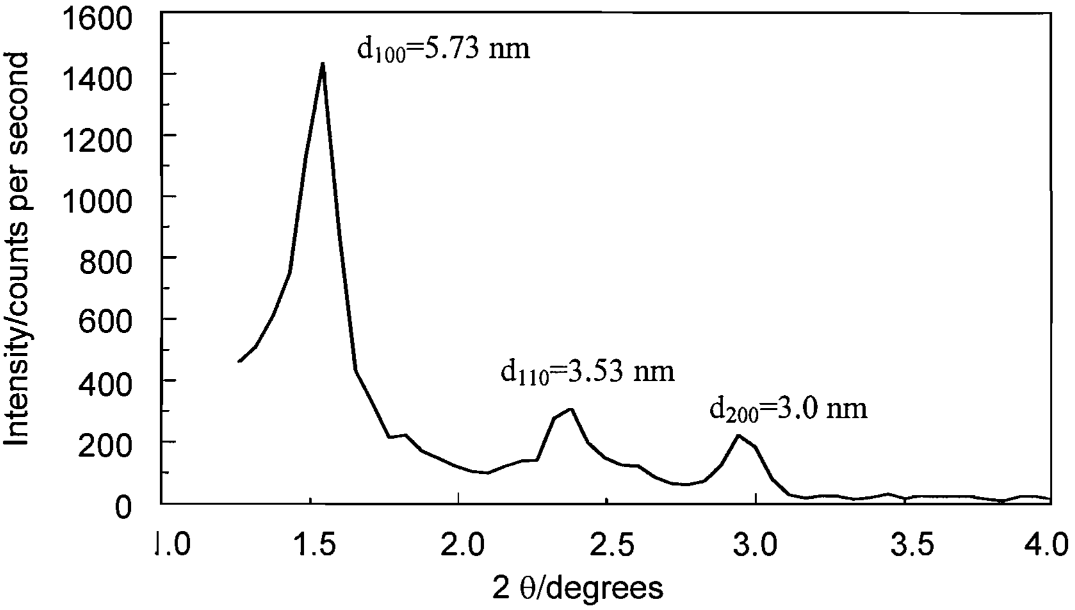

Figure 4.13: Low angle XRD for the hexagonal lyotropic liquid crystalline phase of a mixture consisting of 50 wt.% $C_{16}EO_8$ and 50 wt.% of a solution containing 0.15 M $CdSO_4$/0.005 M TeO_2/0.5 M citric acid

4.6.1 Cyclic voltammetry

Figure 4.14 shows cyclic voltammograms for the CdS electrode in various liquid crystalline templating mixtures of 50 wt. % $C_{16}EO_8$ and 50 wt. % of various electrolyte solutions containing citric acid. The cathodic scan started from an initial potential of 0.85 V *vs.* SCE. In figure 4.14a, using a solution containing 0.5 M citric acid and 0.005 M TeO_2 the potential was scanned negatively towards –0.1 V *vs.* SCE and the cathodic current density begins to increase. This can be assigned to the reductive underpotential deposition of Te from $HTeO_2^+$. The onset of a second cathodic peak at around –0.6 V *vs.* SCE accounts for bulk Te deposition which can be represented by equation 4.5.

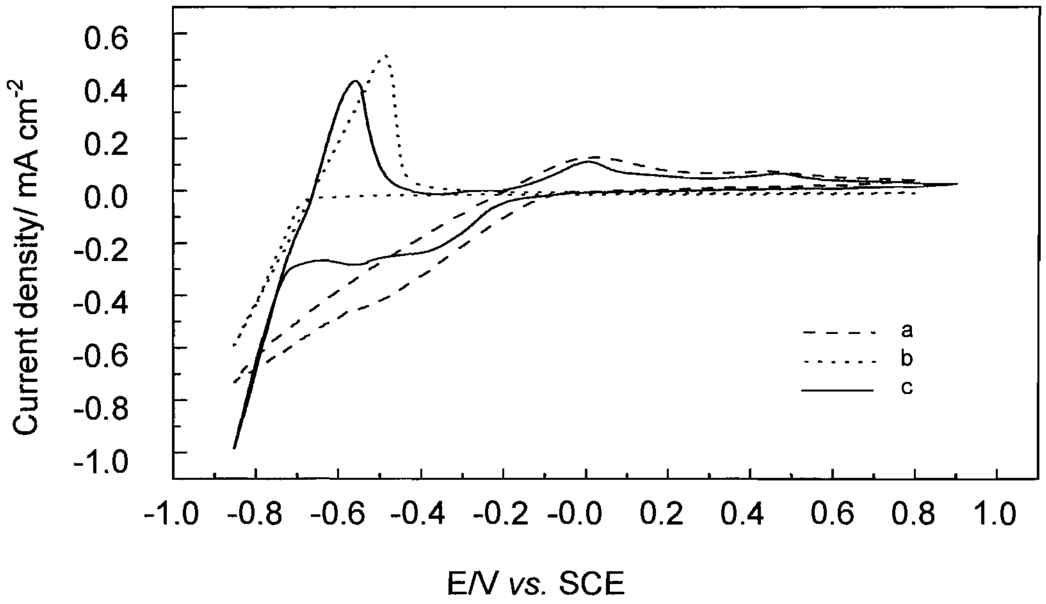

Figure 4.14: Cyclic voltammograms of CdS electrode in various liquid crystalline templating mixtures of 50 wt. % $C_{16}EO_8$ and 50 wt. % electrolyte solutions containing (a) 0.005 M TeO_2 + 0.5 M citric acid, (b) 0.15 M $CdSO_4$ + 0.5 M citric acid, and (c) 0.15 M $CdSO_4$ + 0.005 M TeO_2 + 0.5 M citric acid. All voltammograms were recorded at 50 °C at a scan rate of 10 mV s^{-1}.

$$HTeO_2^+ + 3H^+ + 4e^- \xrightarrow{\qquad} Te + 2H_2O \qquad [4.5]$$

The anodic peaks at 0 V and 0.45 V *vs.* SCE can be ascribed to the stripping of both bulk Te and UPD Te, respectively. Adding $CdSO_4$ to the mixture shifts the deposition potential of Te slightly towards more negative potentials (figure 4.14c) compared with the TeO_2-citrate electrolyte voltammogram (figure 4.14a). A noticeable decrease in the current density is also observed and several theories have been proposed concerning this. Rajeshwar *et. al.* (*9*) suggested an iR drop induced effect , whereby the formation of a CdTe layer increases the resistivity to further deposition. This is also supported by studies carried out by Kroger (*10*) and Wan (*26*). However, Kroger and Wan attributed this to the blocking of the initial Te adsorption sites by the presence of Cd^{2+} ions. Other suggestions for this reduction in current density were SO_4^{2-} (from $CdSO_4$) interactions with $HTeO_2^+$, forming a complex in the bulk solution reducing the number of available Te^{4+} ions (*29*). A direct comparison however cannot be made as different electrolyte conditions (i.e. an electrolytic liquid crystal template mixture was used), and working electrodes were also different in all cases.

$$Cd(Cit)_2^{4-} + Te + 4H^+ + 2e^- \longrightarrow CdTe + 2H_2Cit^-$$

When using a plating bath containing 0.5 M citric acid and 0.15 M cadmium sulfate deposition of elemental Cd begins at a potential of –0.7 V *vs.* SCE, figure 4,14b shown by a cathodic current density rapidly increases, expressed as equation 4.7:

It is known (*58*) that Cd and citric acid ions form the complexes CdH_2Cit^+, CdHCit,

$$Cd(Cit)_2^{4-} + 4H^+ + 2e^- \longrightarrow Cd + 2H_2Cit^-$$

$CdCit^-$, and $Cd(Cit)_2^{4-}$. In these ion species, $Cd(Cit)_2^{4-}$ is shown to be the most stable ion species in electrolytic solutions from complex equilibrium calculation.

The reverse scan shows a sharp anodic peak at –0.0 V *vs.* SCE and represents the stripping of electrodeposited Cd as with the stripping observed with the cyclic voltammogram of CdTe/citric acid on CdS in figure 4.14c.

Finally the cyclic voltammogram of 0.5 M citric acid, 0.15 M cadmium sulfate and 0.005 M tellurium dioxide is shown in figure 14.4c. The cathodic wave commences at –0.2 V and reaches a plateau at -0.4 V corresponding to UPD of tellurium. The following cathodic peak occurs at -0.575 V relating to bulk Te deposition comparable to that observed in figure 4.14b. The third cathodic current density increase (at -0.675 V) is likely to correspond to cadmium deposition by comparison to (equation 4.7). Two subsequent anodic peaks are observed at 0 V and 0.49 V *vs.* SCE, are due to the oxidation of the electrodeposited Te as these also appear in figure 14.4a. Such a behavior can be explained according to the CdTe electrodeposition mechanism proposed by Kröger *et. al.* (*10*). On the basis of these cyclic voltammetry results it can be concluded that mesoporous CdTe can be deposited at potentials more positive than the deposition potential of bulk Cd, i.e. –0.675 V *vs*. SCE, and below the potential where bulk Te reduction begins, i.e., –0.5 V *vs*. SCE.

4.6.2 Characterisation of H_I-eCdTe films

The surface morphology of the electrodeposited bulk CdTe mesoporous and CdTe films grown from citric acid plating baths was characterized by SEM (figure 4.15a and b). Figure 4.15a exhibits a smooth surface which is covered by a layer of closely packed fine crystallites with a diameter of less than 175 nm. The bulk CdTe film deposited in

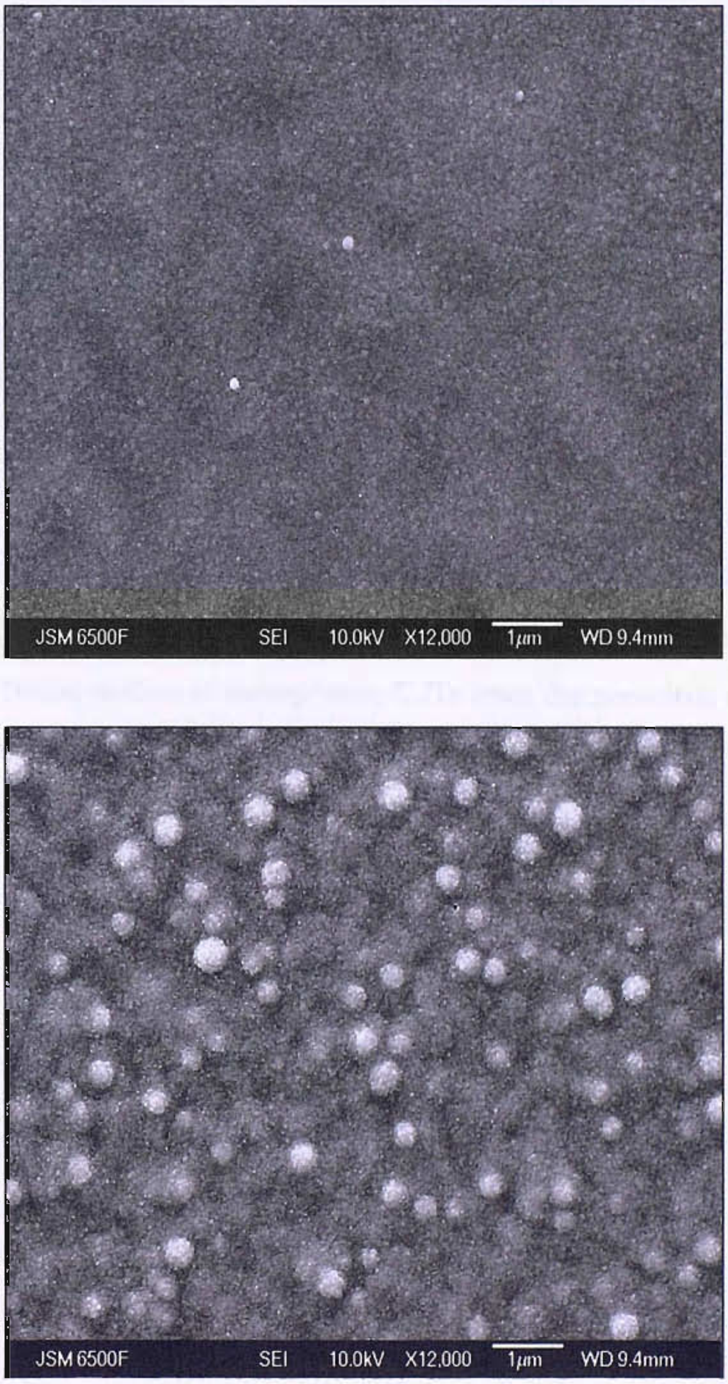

Figure 4.15: SEM images of CdTe films deposited at –0.6 V *vs.* SCE at 50 °C on CdS substrates from a). a liquid crystalline templating mixture and b). an aqueous solution, both containing citric acid.

the absence of the liquid crystalline templating mixture exhibits a lot of aggregates of larger feature sizes up to 450 nm, as shown in Figure 4.15b. The morphology difference between mesoporous and bulk films may be attributed to the liquid crystalline mesophase, which acts as a levelling agent encouraging CdTe growth that is more uniform and compact. The mechanism for this however is unclear According to an EDX analysis, stoichiometric mesoporous CdTe films can be deposited at potentials of –0.58 V to –0.65 V *vs.* SCE.

In order to examine the effect of citric acid on the current efficiency for the deposition of mesoporous CdTe, the film thickness was measured from cleaved cross-sections by SEM and compared with that calculated from charge passed during the deposition. The effective density of the film was estimated to be 4.68 g cm^{-3} since a mesoporous film with a perfect hexagonal nanostructure contains 77.3% (by volume) CdTe and 22.7% (by volume) voids. A CdTe film deposited at –0.6 V *vs.* SCE with a charge density of 0.331 C cm^{-2} would be expected to be 290 nm thick assuming 100% current efficiency. The film thickness measured by SEM was found to be 200 nm, which corresponds to a current efficiency of about 68 %. By comparison to the result obtained for the electrodeposition of mesoporous CdTe from the non-citric acid based electrolyte there was a 400 % increase from 17 % in the current density. This clearly shows an improvement to the current efficiency using citric acid.

4.6.3 Wide angle XRD and annealing of H$_I$e-CdTe on cadmium sulfide deposited from a citric acid bath

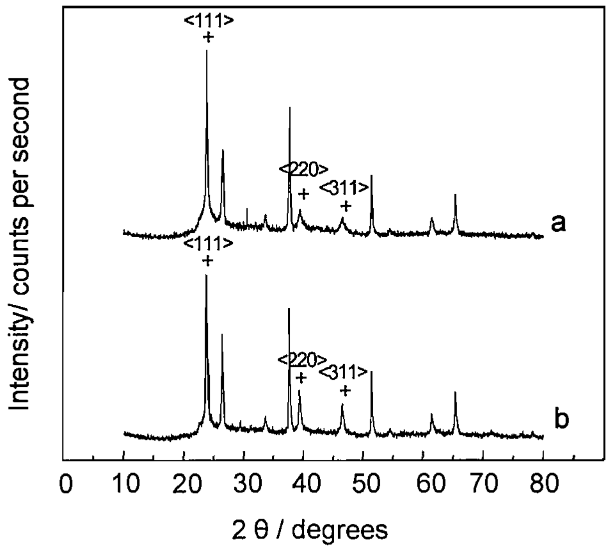

Figure 4.16: Wide-angle XRD patterns for (a) as-deposited and (b) annealed mesoporous CdTe films. The films were deposited at –0.6 V *vs.* SCE at 50 °C on CdS substrates from liquid crystalline templating mixtures containing 50 wt.% $C_{16}EO_8$ and 50 wt.% of a solution containing 0.5 M citric acid, 0.15 M cadmium sulfate and 0.005 M tellurium dioxide. The peaks labelled with cross symbols refer to CdTe, whereas all the other peaks can be attributed to the CdS substrate.

The wide-angle XRD patterns for the as-deposited and annealed mesoporous CdTe on CdS films are shown in figure 4.16. The as-deposited mesoporous CdTe are well crystallized with a preferential orientation along the cubic zinc blend <111> direction, which is characteristic of the usual spontaneous texture axis of electrodeposited CdTe (figure 4.16a). Figure 4.16b shows that after annealing for 1 hour at 400 °C in an argon atmosphere recrystallization takes place, which can be characterized by a change of the preferential orientation, with a substantial increase of the <220> and <311> peak intensity relatively to the <111> one. The change in the intensity of these peaks can be attributed to the annealing process carried out in Argon. The mesoporous CdTe films prepared without citrate did not recrystallise in an oxygen or Argon environment. Using the Debye-Scherrer (DS) formula gives grain sizes of 27 nm and 35 nm, before and after the annealing treatment, respectively.

4.6.4 Characterisation of the mesoporosity

The nanostructure of the mesoporous CdTe films deposited from liquid crystalline templating mixtures was studied by low angle XRD. As shown in figure 4.17 the low angle XRD pattern reveals a single diffraction peak at 1.54 °, which corresponds to diffraction from the d_{100} plane of the hexagonal structure with a *d*-spacing of 5.73 nm. The order length scale determined from the Debye-Scherrer formula is 24 nm. The presence of a d_{100} diffraction peak indicates that the ordered mesophase structure in the liquid crystalline template is preserved in the deposited CdTe film. The broadening of the peak compared with that of liquid crystalline mixture (see figure 4.17) indicates an increase in the degree of disorder. The presence of only one diffraction peak is probably due to a low degree of long-range order, which could be caused by a non-uniform wall thickness (*19*). Conversely, a peak was not observed for the reference CdTe films deposited in the absence of liquid crystalline mixture.

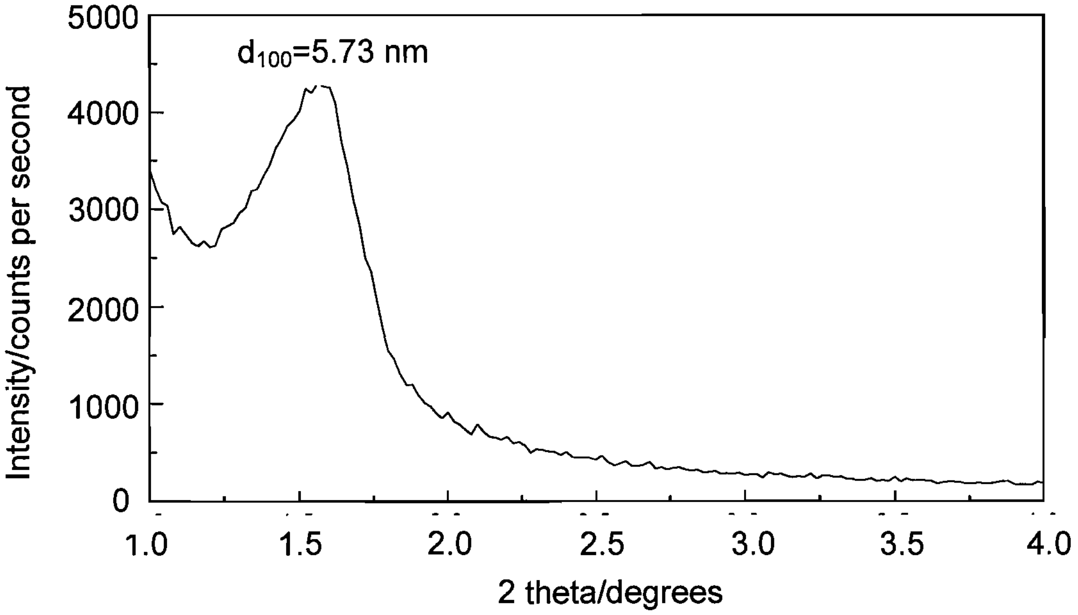

Figure 4.17: Low-angle XRD pattern for mesoporous CdTe films deposited at –0.6 V *vs.* SCE at 50 °C on CdS substrates from liquid crystalline templating mixtures.

4.7 Optical characterisation of H_Ie-CdTe on gold and cadmium sulfide

In this section we will present the results of measurements on the optical properties of two mesoporous CdTe films using UV-Vis spectroscopy. In order to characterise the suitability of the films for optical/optoelectronic applications the optical reflectance spectra was taken for a CdTe film electrodeposited at -0.58 V *vs.* SCE (figure 4.18). These measurements show strong interference fringes and together with a uniform, 'mirror-like' surface the optical flatness of the films was confirmed. In addition the optical measurements indicate that the onset of absorption in the films is strongly dependant on their composition, with the onset of absorption for stoichiometric mesoporous films occurring at 830 nm, close to the accepted room temperature band gap of 858 nm for CdTe.

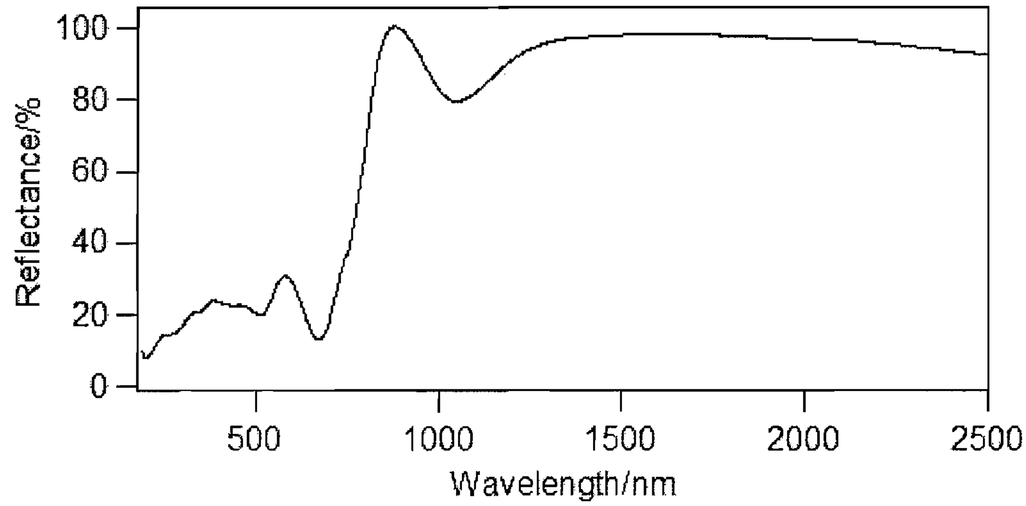

Figure 4.18a: Reflectance spectra of 1.3 μm H_I-eCdTe film deposited at -0.58 V *vs.* SCE on a gold electrode. Dotted line represents the value of the room temperature bandgap, 830 nm of non-mesostructured CdTe.

These results are consistent with bulk CdTe films obtained by Lincot *et al.* (*30*) for CdTe on CdS. The reflection spectrum of stoichiometric films CdTe have an inflection point at 830 nm, which is higher in energy than the bandgap of bulk CdTe (which is attributed to the onset of absorption within the thin films. The slight blue shift in the absorption edge of the mesoporous material relative to non-mesoporous CdTe may be due to quantum confinement, however confirmation of this would require further experimental investigations.

The reflectance spectra for films with an excess of tellurium resulted in absorption at noticeably longer wavelengths than 858 nm. This is because non-stiochiometry in the CdTe films (due to tellurium excess) can lead to electron-hole recombination centres. For example, figure 4.18b shows that films grown using a concentration ratio of ≤10:1 at deposition potentials of –0.58 V *vs.* SCE are not stoichiometric giving rise to Te-rich films (with approximately 60 % tellurium). UV-Vis spectra show that these films begin to absorb light at approximately 1250 nm. This is a huge shift in absorption to longer wavelengths compared to stoichiometric HI-eCdTe films. This can be explained by a decrease in the observed back face reflection (BFR) from that of the film compared with that of the front face reflection (FFR) and therefore by a reduction in the total reflectivity. The decrease in BFR is a consequence of the adsorption of light within the CdTe film. Changing the concentration ratio (R) to 30:1 (where $CdSO_4$ = 0.15 M) and electrodeposition at -0.58 V led to a shift in the reflectance spectra to a position 830 nm within 28 nm of the band gap of CdTe (858 nm).

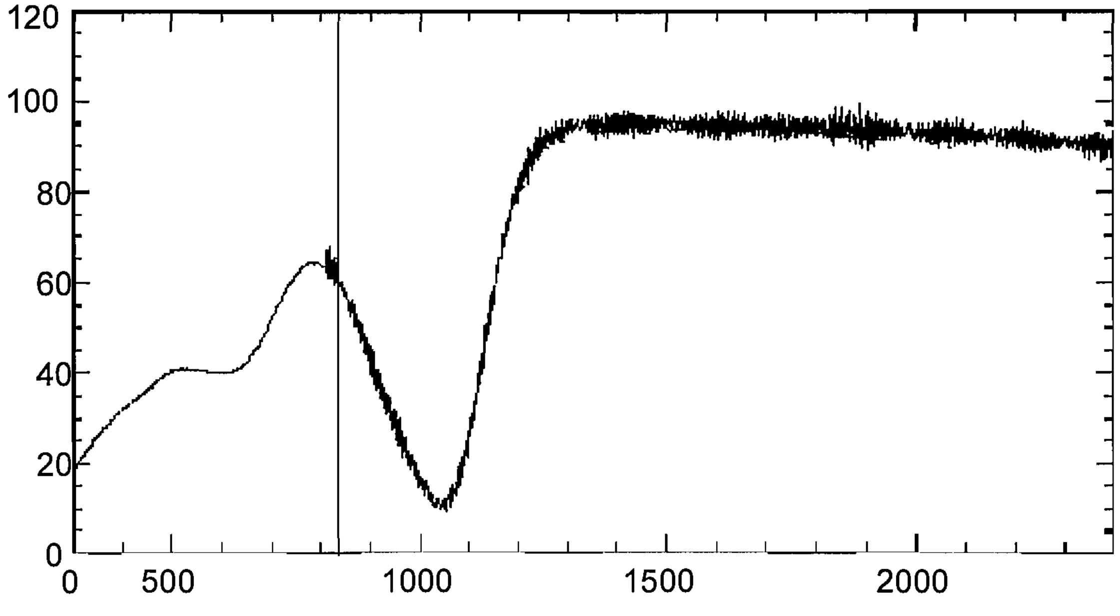

Figure 4.18b: UV/Vis reflectance spectra of a mesoporous Te-rich (60%) CdTe film electrodeposited forma 50wt.% $C_{16}EO_8$ and 50wt.% of a solution containing 0.05 M $CdSO_4$ and 0.005 M TeO_2. The vertical line at 853 nm is at the band gap for non-mesoporous CdTe.

Depositions at -0.58 V *vs.* SCE and R=30 give near perfect stoichiometry and the shift in the absorption to longer wavelengths has disappeared. The importance of controlling the composition of the films is important for producing photoconductivity measurements.

4.7.1 Form Birefringence of H_I-eCdTe on Au

The results obtained from UV-Vis reflection spectra cannot only give information regarding the bandgap of the material, but provide valuable information concerning nanostructuring effects and film thickness.

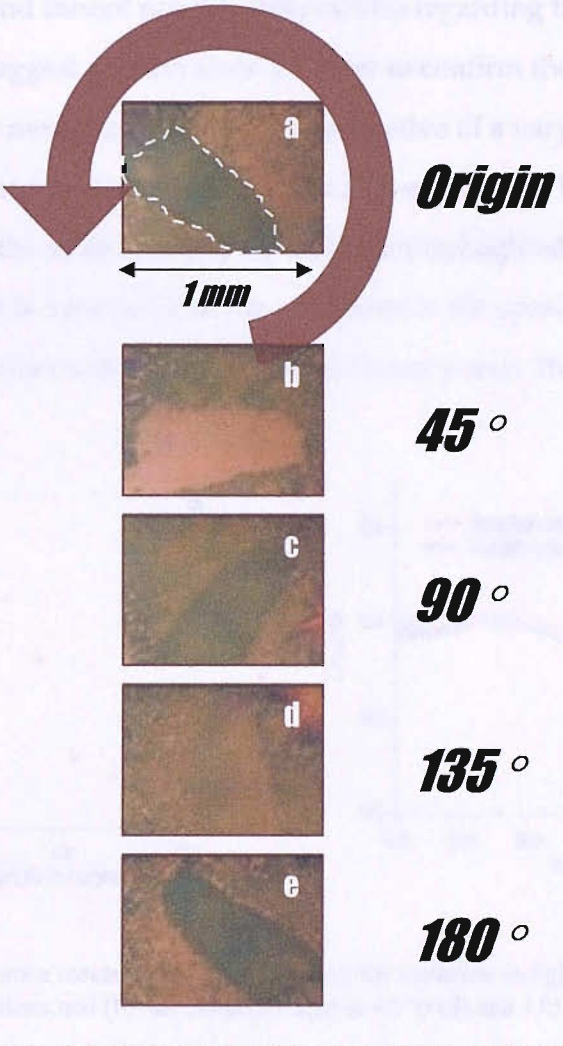

Figure 4.19: Images (a-e) depicting the birefringence of a H_I-eCdTe sample observed using a metallurgical microscope and crossed polarisors on rotation through 45° periods. The arrow shows the rotation direction of the sample (anticlockwise) and the number of degrees rotation are given. The dotted line indicates pore alignment with a common director.

Using a metallurgical microscope with crossed polarisers the birefringence of certain materials can be measured. A beam of light was shone through a polariser onto the sample reflecting the light through the crossed analyser. The sample was then rotated and images of 1 mm were taken from between 0-180°, figures 4.19a-e. A bulk cadmium telluride film was prepared by electrodeposition using 0.15 M $CdSO_4$, 0.005 M TeO_2 and 2 M H_2SO_4. Variation in reflectance spectra and micrographs upon rotation was not observed for this film although it was grown at the same potentials and using the same chemical plating bath, but in the absence of $C_{16}EO_8$.

Figure 4.19, images a-e, clearly depict the anisotropic nature of the pores i.e. the fact that the pores are aligned with different directors in a H_I-eCdTe film. However, it is unclear in which direction the pores are aligned and techniques such as TEM are sample destructive and cannot provide information regarding this. TEM does offer images, which can suggest domain sizes. In order to confirm the form birefringence effects caused by the mesoporosity, which is indicative of a varying refractive index, reflectance measurements were carried out on a H_I-eCdTe film by observing areas reflecting light with the same intensity i.e. all black (highlighted by the dotted white line in figure 4.19a. It is expected that the variations in the speed of light passing within the material will be observed due to the orientation of pores. The variation of reflected

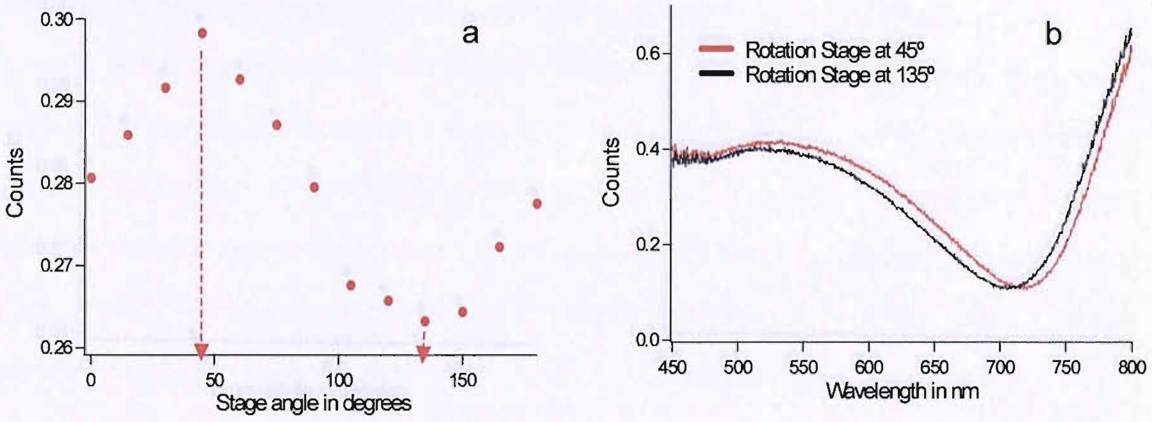

Figure 4.20: Reflectance measurements showing (a). the variation in light reflected after 15 degree rotations.and (b). the reflected light at 45 °(red) and 135 ° (black).

light should be observed with a variation in pore alignment with the incident light. Figure 4.20a clearly shows a sinusoidal wave for the intensity of light reflected which varies as the film rotates. In this experiment the sample was placed under a microscope on a rotation stage and a large domain was found (an area which reflects the incident light with the same magnitude-the sample shows the same colour), that exhibits strong birefringence, figure 4.19. The birefringent area was placed at the centre of rotation of a 25 μm beam of linear polarised light. The light reflected from the sample was measured between 250 nm to 2000 nm wavelengths for 15° sample

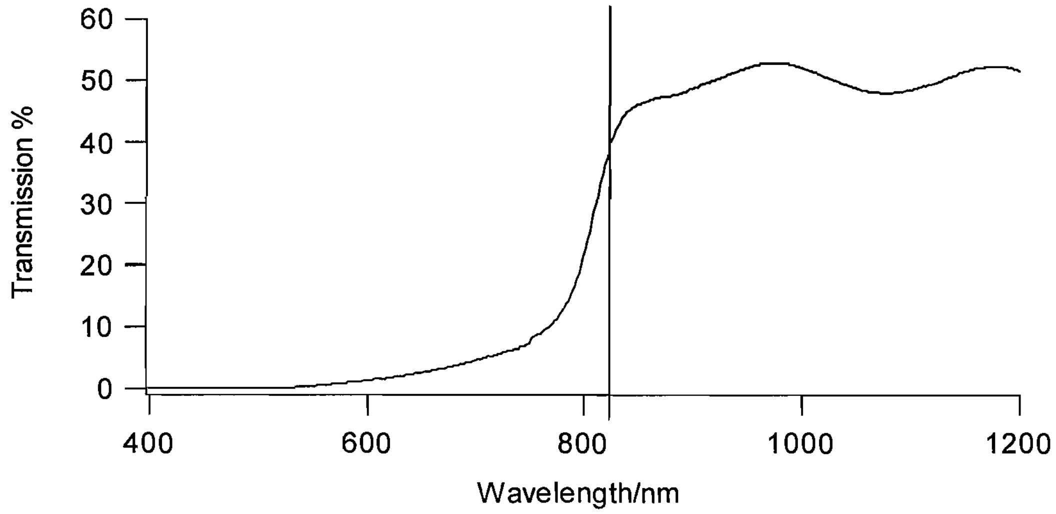

Figure 4.21: Optical transmission spectra for a bulk CdTe film grown on CdS at 85 °C and 0.005 V *vs.* CdRE.

rotations. The spectra were normalised using a silver mirror and a graph of counts against the rotation stage angle was created for the arbitrary value of 628 nm wavelengths. A maximum at ~45 ° and minimum at 135 ° was observed and the reflectance spectra for these films are shown in figure 4.20b. The reflectance spectra for the film rotations at 45 ° and 135 ° are similar however the spectra are not identical and indicate that the refractive indices are not identical at different rotations of the films. The variation in the reflected light by the sample rotation is 90 %. This variation in light for reflectance can be attributed to the difference in the two refractive index of perpendicular and parallel pore alignment.

4.7.2 Birefringence of H_I-eCdTe on CdS

Figure 4.21 shows the transmission spectra of a CdTe film deposited at +0.005 V *vs.* CdRE at 85 °C. The onset of the transmission is abrupt therefore indicating a well-defined bandgap within the region of CdTe. A series of troughs and peaks, interference fringes, at longer wavelengths were observed for all the stoichiometric films and are indicative of flat, good quality CdTe films. All films deposited at +0.005 V and temperatures of 50 °C and 85 °C *vs.* CdRE produced transmission spectra with these features. These were directly comparable to the films prepared by Lincot *et. al.* (*30*).

Figure 4.22 shows reflectance and transmission spectra for the mesoporous CdTe film deposited on CdS substrates. The spectra show clear inference fringes, which confirm the optical flatness and homogeneity of the film.

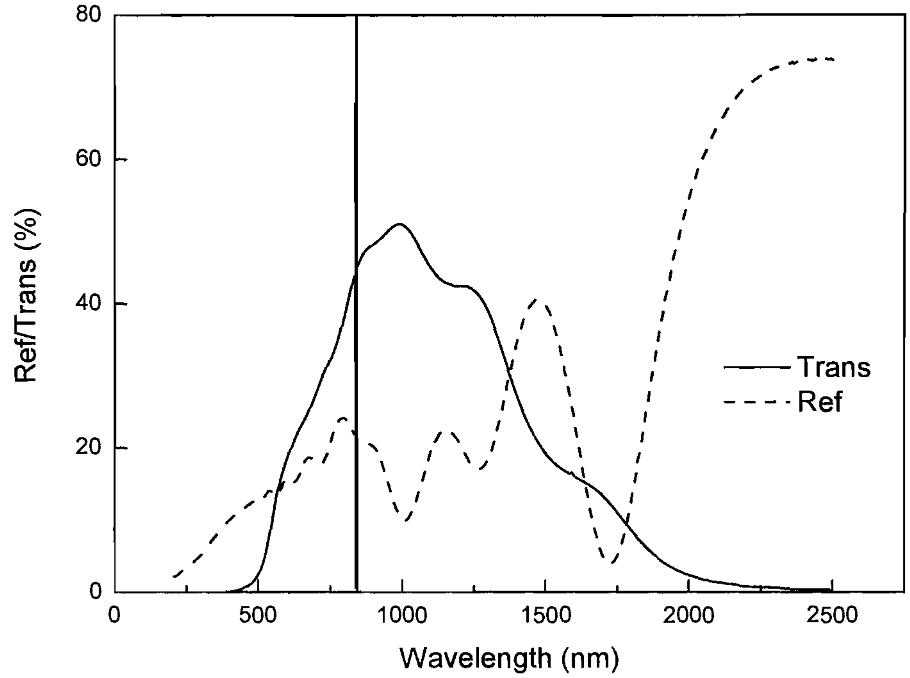

Figure 4.22: Reflectance (dotted line) and transmission (solid line) spectra for the mesoporous CdTe films deposited at –0.6 V *vs.* SCE at 50 °C on CdS substrates from liquid crystalline templating mixtures. The vertical solid line indicates the value of bandgap, 830 nm, of bulk CdTe.

4.7.3 Form Birefringence theory

Mesoporous semiconductor films are promising candidates for photovoltaic, light emitting and various optoelectronic applications. Since mesoporous diameters and topology of nanostructures are under direct control, the novel approach to creating nano-semiconductors could prove to be successful for the analysis of relationships between nanoarchitectures and quantum size effects (27).

The reflection of light provides a method of characterising mesoporous films due to their unique structure. This can be best understood in terms of the wavelike properties

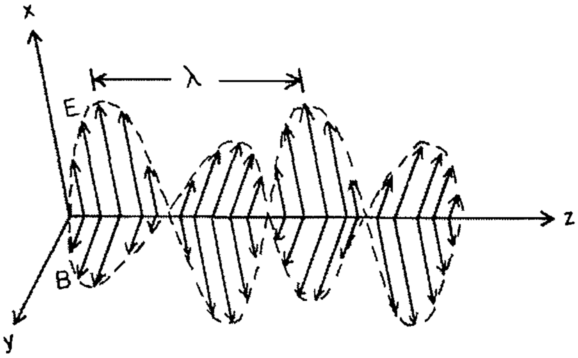

Figure 4.23: Representation of an electromagnetic wave travelling along the z-axis. Where E is the electric field and B is the magnetic field. The wavelength is denoted by lambda.

of light in which the light wave is represented as propagating electric and magnetic fields, with the electric field (E) and the magnetic field (B) perpendicular to each other. Figure 4.23 shows the electromagnetic wave travelling in the z-axis and the E wave parallel to the x-axis and B wave parallel to the y-axis. When both the electric and magnetic fields are perpendicular to each other the light is linearly polarised. Figure 4.23 shows the light to be polarised in the x-axis. The wavelength of light is given by the distance between the maximum reached by the wave at two similar points and is indicated by lambda. The interaction of light with matter, in particular anisotropic materials, can affect electromagnetic waves and give rise to phenomenon such as birefringence. Birefringence is observed when a beam of light is incident on an anisotropic material such as a liquid crystal, due to different refractive indices of the material (*59*). Molecules in a material which are positioned along different axis possess different refractive indices cause light to travel at different rates, the reason behind this effect is illustrated in figure 4.24a.

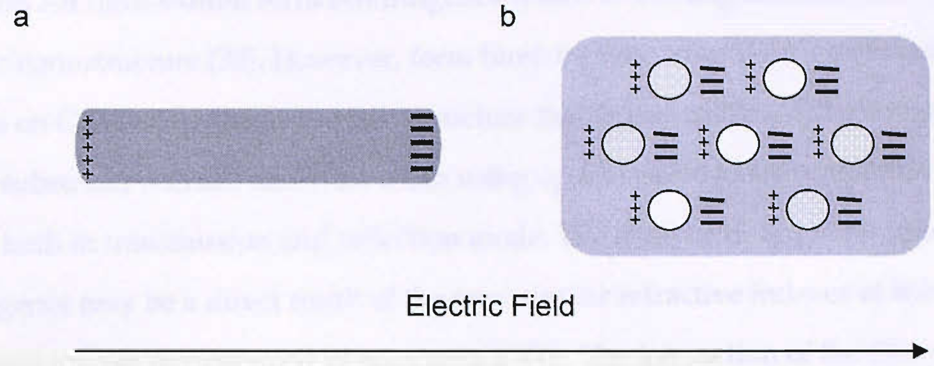

Figure 4.24 : Diagram depicting the aggregation of charges around pores due to the application of an external electric field.

Form birefringence is very much similar to birefringence, however it does not use the anisotropy created by the molecules in materials such as in liquid crystals in the plating mixtures (figure 1.8a). Birefringence is observed due to the molecules oriented along a particular director, however in the form birefringence it is the pores that are oriented along a specific director and responsible for the variation in the speed of light. The characterisation of a mesoporous film's birefringence by polarized light depends on the pores sizes being smaller than that of the incident wavelength of light (*60*). The explanation for form birefringence can be explained by figure 4.24. As an electric wave is directed at a mesoporous material it interacts with the charges present. These charges move, predominately around the pore holes in the material therefore modifying the field. However, this is further changed if for example the electromagnetic field is varied or the sample is then rotated to allow the field to lie parallel or perpendicular with the pores. The same theory can be applied with light. The charge aggregation at the pore boundaries alters the interactions of the light with the material. The velocity of the light will therefore suffer different interactions depending whether or not the charge build up is located at the ends of the pores and therefore the light travelling along the pores will interact less and thus give a shifted phase different to that of the incident beam and of light travelling perpendicular to the pores.

The CdTe on Au films exhibit form birefringence which is a strong characteristic of an anisotropic nanostructure (32). However, form birefringence from the mesoporous CdTe films on CdS (which has a wurtzite structure that is also uniformly birefringent across the substrate) was not observed when using optical microscopy with cross polarizers both in transmission and reflection mode. The absence or apparent absence of birefringence may be a direct result of the very similar refractive indexes of the CdS substrate and the electrodeposited mesoporous CdTe. The interaction of the film with the substrate becomes minimal and is not detectable visually. CdTe films deposited on Au substrates using citric acid from liquid crystalline template mixtures exhibited strong form birefringence as expected. Some of the CdTe films deposited on Au substrates exhibited characteristic fanlike textures of the hexagonal liquid crystalline phase as shown in figure 4.25. This is consistent with the electrodeposition of a H_I-eCdTe film with a hexagonal nanostructure which is derived from the structure of the liquid crystalline template mixture shown in the inset to figure 4.25. The birefringence theory is explained using H_I-eCdTe films prepared on Au as seen in section 4.7.2.

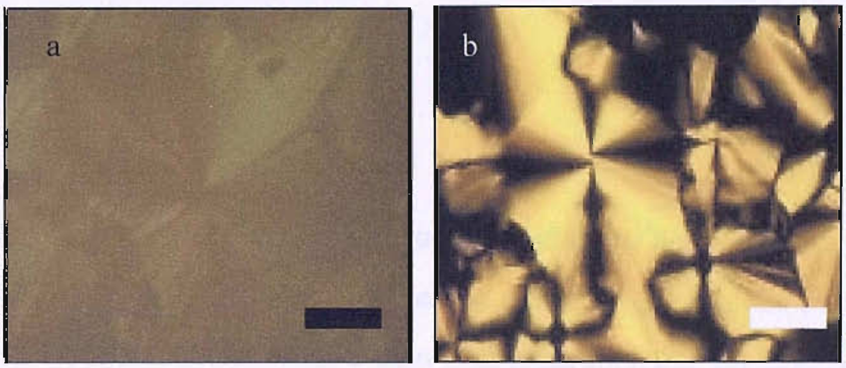

Figure 4.25: Polarised optical micrograph of (a) mesoporous CdTe film deposited at -0.58 V *vs.* SCE at 50 °C on Au and (b). liquid crystalline template mixture from which the film was deposited. Scale bar is 0.1 mm.

A comparison of the reflectance spectra for stoichiometric mesoporous CdTe films and their two principle directions shows a clear wavelength shift of the fringes as expected for an anisotropic material with a birefringence of 4.3% for light traveling parallel to the film normal. This figure varies from domain to domain in the range 4.3% to 1.7%.

Therefore H_I-eCdTe has birefringence in excess of that of KDP and approximately six times greater than Quartz (*61*).

To better quantify the measurements and determine if the observed birefringence could be explained solely by the nanostructuring of the films, the dielectric response expected for a mesoporous material in the long wavelength limit was modeled by the department of Physics and Astronomy at Southampton University.

The dielectric coefficient for light polarized parallel to the cylindrical pores is given by the volume average of the dielectric coefficients of CdTe and air (equation 4.6).

$$\varepsilon_{//} = f\varepsilon_{CdTe} + (1-f) \qquad [4.6]$$

where f is the volume fraction of CdTe. For light polarized perpendicular to the cylindrical pores the result is more complicated, with a simple analytic formula for pores whose diameter is much smaller than their separation (*62, 63*). The perpendicular dielectric coefficient was modeled using two conceptually different methods; direct numerical solution of Laplace's equation (*64*) and a Boundary Integral model (*65*). The three solutions obtained are in full agreement that the dilute limit formula applies for a hexagonal arrangement of cylinders, i.e.

$$\varepsilon_{\perp} = 1 + 2f(\varepsilon_{CdTe} - 1)/(2 + (1-f)(\varepsilon_{CdTe} - 1)) \qquad [4.7]$$

Reflectance spectra (figure 4.20) are calculated from the modeled ordinary,

$$n^{o} = \sqrt{\varepsilon_{\perp}}\ , \qquad [4.8]$$

and extraordinary, $n^{e} = \sqrt{\varepsilon_{\perp}\varepsilon_{//}/(\varepsilon_{\perp}\cos^{2}\theta + \varepsilon_{//}\sin^{2}\theta)}$, [4.9]

refractive indexes for normally incident light using a standard transmission matrix approach (*60*). The separately determined bulk CdTe (*66*) and Au dielectric coefficients

(67) are not counted and, the fit contains three free parameters; the volume fraction of CdTe, which controls the fringe modulation depth, the thickness of the film, which controls the spectral position of the fringe maxima and minima, and the angle of the cylinders relative to the film normal (θ), which controls the birefringence. As can be seen in fig. 4.22 the agreement between theory and experiments is extremely good. The fitting strongly constrains the fitting parameters. The sample thickness obtained from the best fit is 317±5 nm. The best fit volume fraction, 0.63±0.07, corresponds to 4.2±0.4 nm diameter pores for an interpore distance of 6.5 nm, which is well within the limits which can be placed on this parameter from the TEM data. As varying the pore angle allows the predicted birefringence to vary from zero for $\theta = 90^\circ$ to a maximum for $\theta = 0^\circ$ it is possible to fit the full range of birefringences observed for different domains using this parameter alone.

4.8 CONCLUSIONS

In conclusion we have produced a CdTe based metamaterial, containing a hexagonal array of ~4 nm pores with a separation of ~6.5 nm. The pore structure has been visually evidenced by transmission electron microscopy, and XRD has provided corroborative results for the existence of the hexagonal mesophase.

The choice of precursor salt has been shown to be an important factor in the stability of the mesophase at higher temperatures. Liquid crystal templating mixtures containing a cadmium perchlorate precursor salt have indicated interactions between perchlorate ions and the surfactants head groups allowing the hexagonal mesophase retention at temperatures beyond that of the blank liquid crystal template. The surfactant structure but more importantly its interactions with anions and cations present in the electrolyte are paramount the structure of the surfactant template.

In all cases careful control must be exercised in order to ensure stoichiometry. The following experimental factors have been shown to be important in producing highly reflective, adherent, stoichiometric mesoporous CdTe films; a concentration ratio $R \geq 20$, a deposition potential of $-0.65 \text{ V} \geq x \geq -0.55 \text{ V}$ and a deposition duration of between 18000 s and 43200 s.

The cathodic deposition of mesoporous CdTe from a citric acid bath was carried out producing stoichiometric adherent, flat, shiny films. The surface morphology was dense and SEM showed almost no surface features unlike the bulk CdTe films deposited from the aqueous citrate based CdTe template mixtures. The mesoporous CdTe films deposited in a citrate based electrolyte were produced at a potential 0.02 V more negative than that of the mesoporous not citrate based template mixtures and yielded an approximately 400% increase in the current efficiency of the electrodeposition. This gives a strong indication in that using citric acid can greatly improve the deposition rate of mesoporous CdTe.

The information in this chapter, from TEM data, has shown that the films contain regular arrangement of cylindrical pores with a pore diameter of approximately 7.0 nm. Some conclusive evidence was provided by XRD results which suggest that the pore size is slightly larger at 6.9 nm.

The aim of the UV-Vis measurements provided a new method of examination of form birefringence within mesoporous materials with the critical dimension in the nanometer region. The results showed that at high concentrations of Te within the film leads to Te recombination centres. This in turn shows produces a band gap above that of CdTe at 853 nm.

This metamaterial has strong optical birefringence at energies above and below the band gap energy. The optical properties of films have been modeled using first principles electromagnetic simulations and have been shown to be entirely explicable in terms of the nanoporosity within the films.

4.9 REFERENCES

1. N. W. Duffy, L. M. Peter, R. L. Wang, D. W. Lane, K. D. Rogers, *Electrochimica Acta* **45**, 3355 (2000).
2. M. D. Lay, J. L. Stickney, *Journal of the Electrochemical Society* **151**, C431 (2004).
3. C. Lepiller, P. Cowache,J. F. Guillemoles,N. Gibson,E. Ozsan, D. Lincot, *This Solid Films* **361-362**, 118 (2000).
4. A. H. Whitehead, J. M. Elliot, J. R. Owen, G. S. Attard, *Chemical Communications*, 331 (1999).
5. T. Gabriel, I. S. Nandhakumar, G. S. Attard, *Electrochemical Communications* **4**, 610 (2002).
6. I. Nandhakumar, J. M. Elliot, G. S. Attard, *Chemical Materials* **13**, 3840 (2001).
7. N. B. Bartlett, P. N. Birkin, A. M. Ganhem, P. de Groot, M. Sawicki, *Journal of the Electrochemical Society* **148**, C119 (2001).
8. G. S. Attard, S. A. A. Leclerc, S. Maniguet,A. E. Russell, I. Nandhakumar, R. B. Gollas, N. B. Bartlett, *Microporous and Mesoporous Materials* **44-45**, 159 (2001).
9. K. Rajeshwar, R. N. Bhattacharya, *Journal of the Electrochemical Society* **131**, 2032 (1984).
10. M. P. R. Panicker, M. Knaster, F. A. Kroger, *Journal of the Electrochemical Society* **125**, 566 (1978).
11. N. R. B. Coleman, PhD, Southampton University (1997).
12. D. Lincot, J. Vedel, *Journal of Physical Chemistry* **92**, 4103 (1988).
13. Y. Sugimoto, PhD, Southampton University (1991).
14. M. Takahashi, K. Uosaki, H. Kita, *Journal of Electrochemical Society* **131**, 2304 (1984).
15. J. Touskova, D. Kinl, J. Tousek, *Thin Solid Films* **293**, 272 (1997).
16. R. K. Sharma, G. Singh, A. C. Rastogi, *Solar Energy Materials and Solar Cells* **82**, 201 (2004).
17. K. Murase, H. Watanabe, S. Mori, T. Hirato, Y. Awakura, *Journal of the Electrochemical Society* **146**, 4477 (1999).
18. K. Murase, T. Honda, M. Yamamoto, T. Hirato, Y. Awakura, *Journal of the Electrochemical Society* **148**, C203 (2001).
19. K. Murase, M. Matsui, M. Miyake, T. Hirato, Y. Awakura, *Journal of the Electrochemical Society* **150**, C44 (2003).
20. S. I. Hsiu, I. W. Sun, *Journal of Applied Electrochemistry* **34**, 1057 (2004).
21. S. J. Lade, M. D. Uplane, Lokhande, *Materials Chemistry and Physics* **63**, 99 (2000).
22. C. Sella, P. Boncorps, J. Vedel, *Journal of Electrochemical Society* **133**, 2043 (1986).
23. J. W. Danaher, L. E. Lyons, *Australian Journal of Chemistry* **36**, 1011 (1983).
24. N. W. Duffy, D. W. Lane, E. Ozsan, L. M. Peter, K. D. Rogers,R. L. Wang, *Thin Solid Films* **361-362**, 314 (2000).
25. A. Kampmann, P. Cowache, J. Vedel, D. Lincot, *Journal of Electroanalytical Chemistry* **387**, 53 (1995).
26. J. H. Chen, C. C. Wan, *Journal of Electroanalytical Chemistry* **365**, 87 (1994).
27. R. Sathyamoorthy, Narayandass, K. Sa, Mangalaraj, *Solar Energy Materials and Solar Cells* **76** (2003).

28. E. A. Meulenkamp, L. M. Peter, *Journal of the Chemical Society, Faraday Trans.* **92** (1996).
29. S. Dennison, S. Webster, *Journal of Electroanalytical Chemistry* **333**, 287 (1992).
30. A. Kampmann, P. Cowache, B. Mokili, D. Lincot, J. Vedel, *Journal of Crystal Growth* **146**, 256 (1995).
31. L. Ndiaye, P. Cowache, M. Cadene, D. Lincot, J. Vedel, *Thin Solid Films* **224**, 227 (1993).
32. M. L. Markham, J. J. Baumberg, D. C. Smith, X. Li, T. Gabriel,I. Nandhakumar, G. S. Attard, *Applied Physics Letters* **86**, 11912 (2005).
33. I. S. Nandhakumar, T. Gabriel, X. Li, M. L. Markham, D. C. Smith, J. J. Baumberg, G. S. Attard, G. S, *Chemical Communications* **12**, 1374 (2004).
34. A. W. Zhao, G. W. Meng, L. D. Zhang, T. Gao, S. H. Sun, Y. T. Pang, *Applied Physics A* **76**, 537 (2003).
35. M. Nogami, K. Nagasaka, S. Toshiharu, *Journal of the American Ceramic Society* **75**, 220 (1992).
36. B. M. Rabatic, M. U. Pralle, G. N. Tew, S. I. Stupp, *Chemical Materials* **15**, 1249 (2003).
37. V. Tohver, P. V. Braun, M. U. Pralle, S. I. Stupp, *Chemistry of Materials* **9** (1997).
38. V. P. Braun, P. Osenar, V. Tohver, S. B. Kennedy, S. I. Stupp, *Journal of the American Chemical Society* **121**, 7302 (1999).
39. X. Auvray, L. Petipas, R. Anthore, I. Rico, A. Lattes, *Journal of Physical Chemistry* **93**, 7458 (1989).
40. J. W. Mcbain, A. J. Burnett, *Journal of the Chemical Society* **121**, 1320 (1922).
41. A. J. Bard, *Analytical chemistry* **35**, 340 (1963).
42. D. J. Mitchell, G. J. T. Tiddy, L. Waring, T. Bostock, M. P. McDonald, *J. Chem. Soc. Faraday Trans. I* **79**, 975 (1983).
43. G. S. Attard, P. N. Bartlett, N. R. B. Coleman, J. M. Elliot, J. R. Owen, J. H. Wang, *Science* **278**, 838 (1997).
44. I. W. Hamley, *Introduction to soft matter polymers, colloids, amphiphiles and liquid crystals* (Wiley, 2000), pp. 134-147.
45. O. Dag, S. Alayoglu, I. Uysal, *Journal of physcial chemistry B* **108**, 8439 (April 9 2004, 2004).
46. B. A. Bagshaw, *Journal of Materials Chemistry* **11**, 831 (2001).
47. H. W. Hillhouse, J. W. van Egmond, M. Tsapatsis, J. C. Hanson, J. Z. Larese, *Microporous and Mesoporous Materials* **44-45**, 639 (2001).
48. C. Lepiller, D. Lincot, *Journal of the Electrochemical Society* **151**, C348 (2004).
49. I. Nandhakumar, PhD, Southampton University (1999).
50. L. Montes, F. Muller, F. Gaspard, R. Herino, *Thin Solid Films* **297**, 35 (1997).
51. A. Saraby-Reintjes, L. M. Peter, E. Ozsan, S. Dennison, S. Webster, *Journal of Electrochemical Society* **140**, 2880 (1993).
52. G. Maurin, D. Pottier, *Journal of Materials Science Letters* **6**, 817 (1987).
53. S. K. Das, *Solar Energy Materials and Solar Cells* **29**, 277 (1992).
54. T. Pauporte, D. Lincot, *Electrochemica Acta* **45**, 3345 (2000).
55. X. Li, I. S. Nandhakumar, T. Gabriel, G. S. Attard, M. L. Markham, D. C. Smith, J. J. Baumberg, *Journal of Material Chemical*, **16**, 320, (2006)
56. L. M. Peter, Y. Sugimoto, *Journal of Electrochemical Communications* **381** (1995).

57. J. M. Woodcock, A. K. Turner, E. M. Ozsan, J. G. Summers, paper presented at the Proceedings 22nd IEEE Photovoltaic Specialists Conference, New York 1993.
58. S. U. M. Khan, S. Zhang, *Journal of the Electrochemical Society* **142**, 2539 (1995).
59. P. J. Collings, *Liquid Crystals* (Princeton, 1990).
60. M. Born, E. Wolf, *Principles of Optics* (Pergamon Press, ed. 2nd, 1964), pp. 51.
61. G. W. C. Kaye, T. H. Laby, *Tables of Physical and Chemical Constants* (Longman, ed. 16th, 1995).
62. W. L. Bragg, A. B. Pippard, *Acta Crystallograpica* **6**, 865 (1953).
63. J. B. Keller, *Journal of Mathematical Physics* **5**, 548 (1964).
64. M. V. K. Chai, S. J. Salon, *Numerical Methods in Electromagnitism* (Academic Press, 2000).
65. M. Bonnet, *Boundary Intergral Equation Methos for Solids and Fluids* (John Wiley and Sons, 1999).
66. S. Adachi, T. Kimura, N. Suzuki, *Journal of Applied Physics* **74**, 3435 (1993).
67. D. W. Lynch, W. R. Hunter, *in Handbook of Optical Constants of Solids*. E. D. Palik, Ed. (Academic Press, 1984).

CHAPTER FIVE:

FABRICATION AND CHARACTERISATION OF NANOSTRUCTURED ZINC OXIDE

5.1 INTRODUCTION

Thin films of ZnO attract much attention due to its possible use as transparent conducting surfaces in industrial applications, such as flat panel electroluminescence displays. They can also be used as a transparent conducting window layer (*1*) in thin film solar cells based on $CuInS_2$ (*2*) and amorphous silica (*3*) adsorbers. ZnO is a type II-VI compound semiconductor with a band gap of 3.2-3.7 eV and because of this may possess unusual characteristics when in the nanometer range.

Several methods have been reported for preparing ZnO films; sputtering (*4*), pulsed laser deposition (PLD) (*5*), chemical vapour deposition (CVD) (*6*), molecular beam epitaxy (MBE) (*7*), atomic layer epitaxy (ALE) and spray pyrolysis (SP) (*8*). However, more recently electrodeposition techniques have been used to prepare uniformly structured thin films of ZnO films. Electrodeposition provides the basis for a cost effective , low pressure and temperature fabrication route with greater control over the films morphology, thickness and deposition rate (*9, 10*).

Over the last decade, much of the research on the electrodeposition of ZnO focuses on the fabrication of ZnO in the form of uniquely structured films, such as nanopillars (*11*), nano-rods (*12*), nanostructured electrodes (*13-15*) and nanocolumnar crystals (*16*) and in 2003 the fabrication of mesoporous ZnO films from a hexagonal liquid crystal temperature was been reported (*17*).

In general, the electrodeposition of ZnO is carried out cathodically according to the overall reaction:

$$Zn^{2+} + \tfrac{1}{2} O_2 + 2e^- \longrightarrow ZnO \qquad [5.1]$$

However, there are some inconsistencies concerning the origin of the oxygen for the formation of zinc oxide. Most of the studies suggest that the reduction of an oxygen precursor in the presence of metallic zinc ions is an overall two-electron reduction process. Lincot and Izaki suggest that the precursor oxygen originates from molecular oxygen bubbled into the solution, (equation 5.1) (*9*, *10*), while Switzer and Gal-Or report that oxygen is obtained from nitrate ions (equations 5.2-5.5) (*18*, *19*). However in general, literature suggests the origin of the oxygen to come from either, oxygen (bubbled), nitrate (from the anion) or hydrogen peroxide. The mechanism for zinc oxide formation in aqueous solution shown in reactions 5.2 – 5.5, is given by the following explanation; as the current is passed, the diffusing nitrate ions are electrochemically reduced to hydroxide ions an increase in the pH occurs near the surface of the electrode. The diffusion of the Zn $^{2+}$ ions allows precipitation of both the hydroxide ions and zinc ions and subsequently spontaneous dehydration into zinc oxide.

$$Zn(NO_3)_2 \longrightarrow Zn^{2+} + 2\,NO_3^- \qquad [5.2]$$

$$NO_3^- + H_2O + 2e^- \longrightarrow NO_2^- + 2\,OH^- \qquad [5.3]$$

$$Zn^{2+} + 2\,OH^- \rightleftharpoons Zn(OH)_2 \qquad [5.4]$$

$$Zn(OH)_2{}^{+} \longrightarrow ZnO + H_2O \qquad [5.5]$$

The formation of the film on the electrode surface has also come under particular debate and has yet to be clearly defined. Nucleation of the film requires the formation system to be metastable. The metastability is created by an overpotential, which in turn produces nuclei on the electrode surface. The formation of these nuclei is dependant on the available activation sites on the electrode surface. The electrode surface is one of a number of significant parameters which can effect electrodeposition of ZnO such as; the pre-activation treatment of the electrode surface (*20*), the type of precursor salt and its concentration (*21*), the temperature (*22*), the electrode potential (*23*) and the dissolved oxygen concentration (*21*, *24*). For example, high temperatures are essential for the crystalline ordering of the ZnO films on Au (*20*), and in general, temperatures of 65 °C are used for the deposition. Numerous researchers have shown evidence for this. For example, Lincot *et. al.* have previously used temperatures >34°C to facilitate the formation of hexagonally shaped platelets, whereas temperatures of 25 °C result in amorphous ZnO films on Au (*14*).

All these parameters go alongside the standard electrochemical parameters such as time and experimental set up (including the shape and geometry of the electrodes and volume of solutions). As with all liquid crystal template deposition, outlined in this thesis, stirring is not an issue. Using electrochemical deposition processes to obtain ZnO films with optoelectronic properties (luminescence properties) is also known to depend on the choice of substrate and post annealing treatment (*25, 26*). Other mesoporous semiconductor films (*9, 19, 27*) have shown that the introduction of high concentrations of a surfactant (acting as a template) for the electrodeposition of mesoporous ZnO will require different growth conditions and parameters compared with bulk ZnO deposition.

The aim of this chapter is to prepare mesoporous nanostructured zinc oxide films on metallic (Au) and transparent substrates (ITO) using liquid crystal templates of non-ionic polyoxyethtylene surfactants (Brij®56 and $C_{16}EO_8$). Initially, the films will be characterized by SEM and wide angle XRD to assess the surface morphology, and by low angle XRD to describe the nanostructuring within the film. The ZnO mesoporous depositions will be carried out under a number of different experimental conditions to assess the optimum conditions for fabricating reproducible, adherent, homogenously nanostructured structured films

The mesoporous zinc oxide films fabricated in the following sections are novel materials which may posses unusual optical properties, and given the high importance of these materials as optical materials, this will provide interesting fundamental data.

5.2 ELECTRODEPOSITION OF BULK ZINC OXIDE

5.2.1 Electrochemistry

Figure 5.1 shows a typical cyclic voltammogram for a polycrystalline gold electrode in a 0.1 M zinc nitrate solution at 65 °C, recorded at a scan rate of 20 mV s^{-1}. Essentially, there are no Faradaic processes at potentials less than -0.35 V *vs.* SCE. The scan shows an increase in the cathodic current commencing at –0.55 V which continues to increase until –1.15 V *vs.* SCE where it reaches a maximum of -5.4 mA cm^{-2} as indicated by the asterisk. According to previous research, the potential of the cathodic peak can be attributed to the formation of ZnO (*9, 20, 27*). On the reverse scan, no anodic stripping peaks are observed indicating the high stability of the electrodeposited ZnO. Similar cyclic voltammetric features were observed when the Au electrode was substituted by an ITO electrode (figure 5.1b).

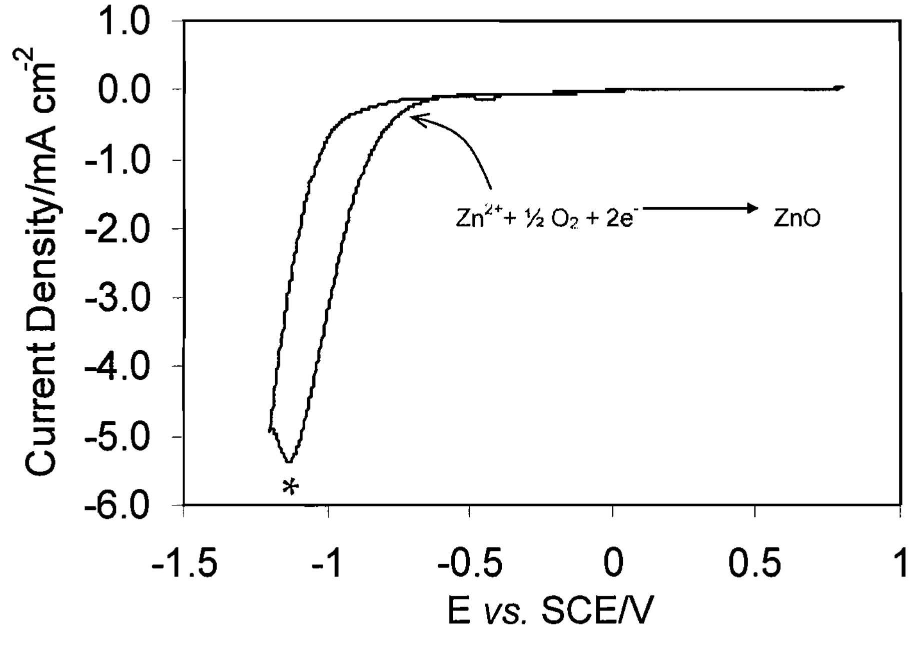

Figure 5.1a: Cyclic voltammogram for an Au electrode in a solution containing 0.1 M $Zn(NO_3)_2$. The temperature was 65 °C and a scan rate of 20 mV s^{-1} was employed. Electrode area: 1.36 cm^2.

Figure 5.1b shows the cyclic voltammogram for an ITO electrode in a solution of 0.1 M zinc nitrate solution at 65 °C at a scan rate of 20 mV s^{-1}. With a scan origin of 0.0 V *vs.* SCE, the potential was negatively scanned to -1.55 V. No electrochemical processes were observed until a very gradual increase in the cathodic current density at -0.34 V. At -0.75 V the current density then increases again at a higher rate until -1.21 V (-0.46 mA cm^{-2}) where it reaches a plateau. The potential region between -1.21 V and -1.27 V (indicated by the asterix) is attributed to the reduction of Zn^{2+} to Zn according to equation [5.5]. Comparing the cyclic voltammograms shown in Figures 5.1a and b,

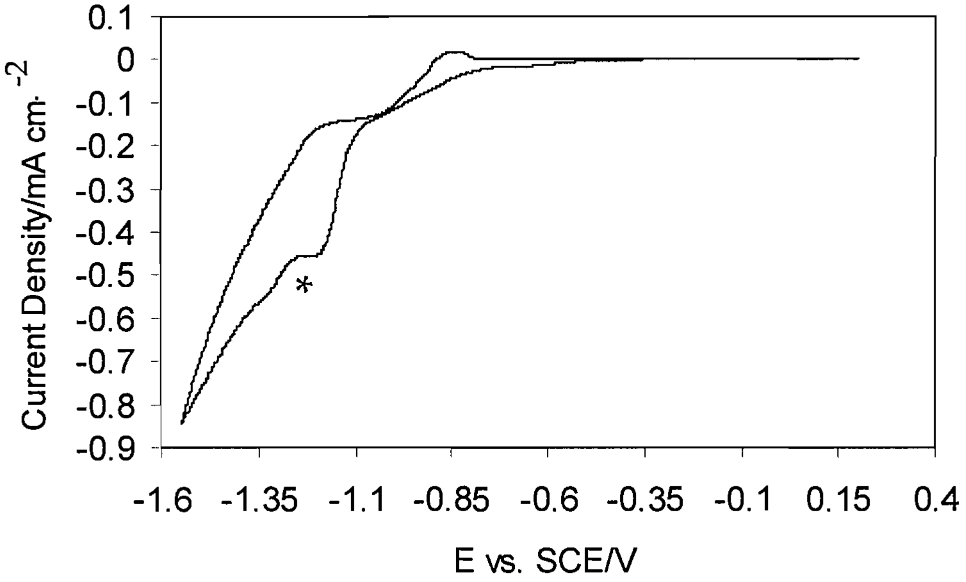

Figure 5.1b: Cyclic voltammogram for an ITO electrode in a solution containing 0.1 M $Zn(NO_3)_2$. The temperature was 65 °C and a scan rate of 20 mV s^{-1} was employed. Electrode area: 1.24 cm^2.

ZnO depositions on Au and ITO exhibit very similar voltammetric features which are in accordance with other studies (*9*). Figure 5.1b shows that at -1.27 V a further increase in the cathodic current density is observed and according to Lincot *et. al.* (*28*) this is caused by the reduction of the solvent according to the equation 5.6:

$H_2O + e^- \longrightarrow OH^- + ½ H_2$ [5.6]

or the reduction of Sn^{2+},

$Sn^{2+} \longrightarrow Sn + 2e^-$ [5.7]

In the reverse scan, the only anodic peak is observed at -0.85 V indicating the reoxidation of metallic Sn, which in close agreement with the redox potential of the SnO_2/Sn couple at -0.71 V *vs.* SCE evidenced by Pourbaix (*11, 29*).

5.2.2 X-Ray Diffraction (XRD)

Using the cyclic voltammetry (figure 5.1) to ascertain the electrodeposition potential, a film was electrodeposited at a potential of -1.145 V *vs.* SCE and a temperature of 65 °C. The crystallinity of the electrodeposited ZnO films on gold substrates was investigated by wide angle XRD and a representative diffractogram is shown in figure 5.2. The XRD pattern reveals the polycrystalline nature of the as-deposited ZnO film, with a

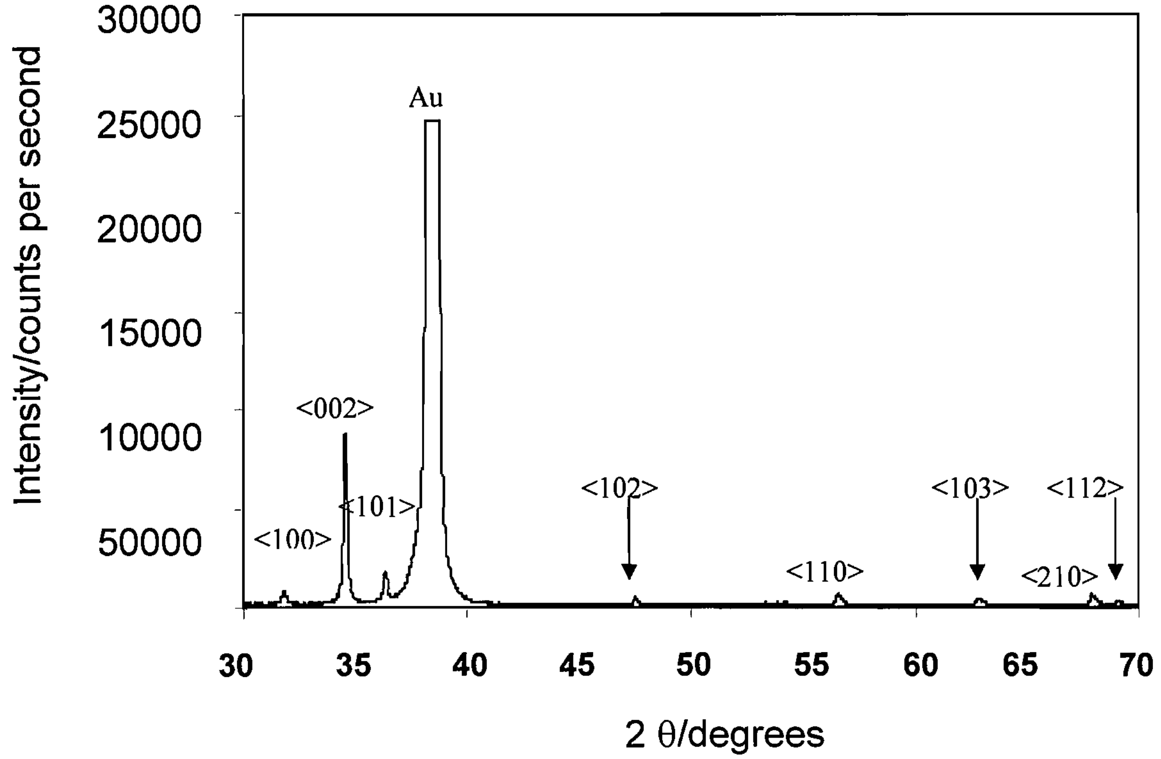

Figure 5.2: X-ray diffractogram for a bulk ZnO film electrodeposited at -1.145 V on Au at 65 °C.

preferred <002> orientation. This specific crystallographic orientation of <002> is perpendicular to the substrate plane and the orientation may be directly attributed to the Au substrate (*11, 20, 24, 30*). This preferential orientation of ZnO, along the *c-axis*, on polycrystalline substrates (Au and Si) is common and consistent with previous findings (*21*). Comparing electrodeposited ZnO films with XRD patterns of powdered ZnO from JPCDS, shows that these peaks are in close agreement with the *d*-spacings given for the orientations labeled <100>, <002> and <101> and higher orders <102>, <110>, <103>, <210> and <112> shown in figure 5.2. The peaks in figure 5.2 were labeled according to the findings in JPCDS.

5.2.3 Scanning electron microscopy (SEM)

Figures 5.3a and b show images of a bulk ZnO film deposited onto a gold substrate at a temperature of 65 °C using an electrolyte solution containing 0.1 M $Zn(NO_3)_2$ at a deposition potential of -1.145 V *vs.* SCE. The film is compact with large hexagonally shaped crystals covering the entire electrode surface (Figure 5.3a). Total coverage of ZnO film over the electrode surface and the lack of voids or cracks suggests the formation of a high density of nucleation sites across the electrode during initial stages of deposition which coalesce as the deposition proceeds (i.e. at longer deposition times).

Figure 5.3b shows the SEM cross section of a ZnO layer electrodeposited onto Au at -1.145 V. The ZnO layer was polycrystalline without visible oriented growth direction perpendicular to the substrate surface as described by and in section 5.2.1 by XRD diffractograms. Lincot *et. al.* states that a strong affinity between gold and zinc generally leads to a compact and covering layer (*31*, 32), as evidenced in figure 5.3a.

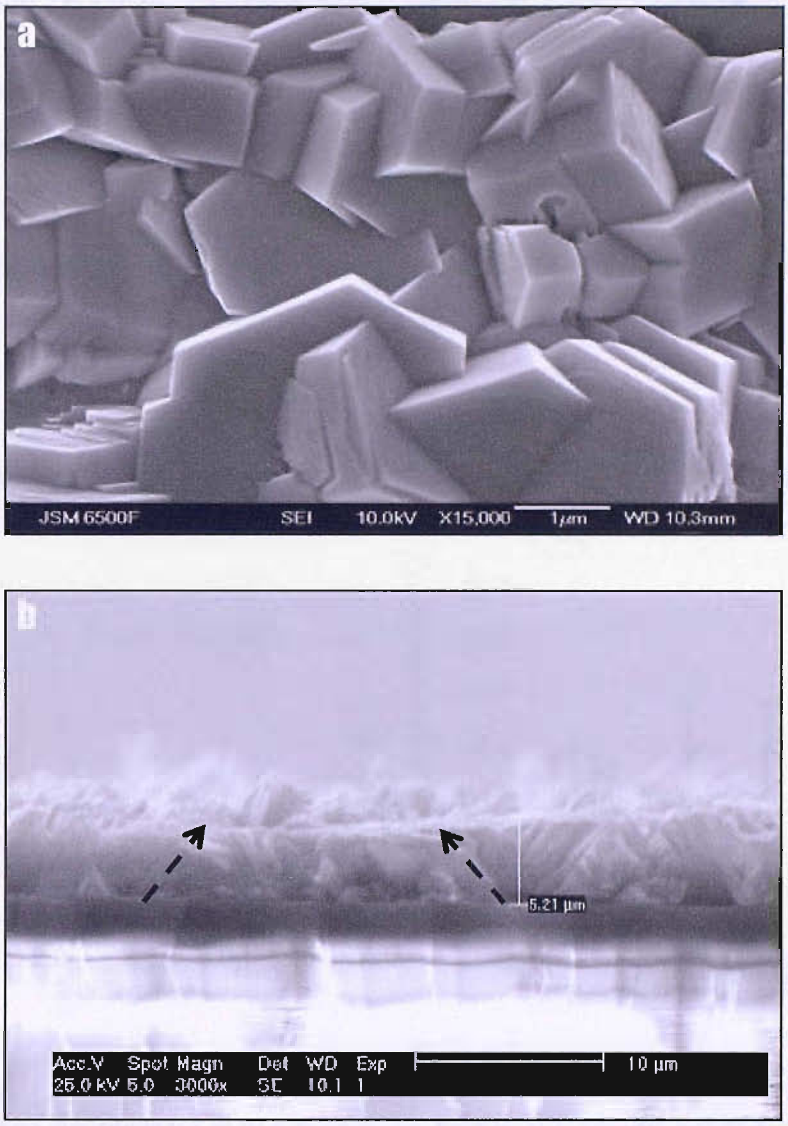

Figure 5.3: SEM micrographs for a ZnO film deposited from 0.1 M $Zn(NO_3)_2$ at 65 °C onto a polycrystalline gold substrate. a). image taken of the surface of the ZnO film. (b). cross sectional SEM image of the same film taken at a rotational angle of 90 °. The dotted lines indicate the orientation of the platelets.

The growth directions have been indicated by the black dotted lines in figure 5.3b. The surface of the ZnO film is not flat and defects (in the form of film thickness and cracks) were located throughout the film. However, although the preferred orientation is in the <002> direction from wide angle XRD although the <100> and <101> orientations are noticeable. The SEM images can only suggest that the growth orientation is not entirely perpendicular to the surface. This agrees with the XRD results, which also show several different growth orientations.

5.3 FABRICATION OF MESOPOROUS ZINC OXIDE

It has been shown that the incorporation of an electrolyte solution into a liquid crystal template mixture can affect the stability of the liquid crystalline phase as discussed in chapters 4, section 4.2. In this section we aim to obtain the necessary conditions for the electrodeposition of mesoporous ZnO from the domains of a liquid crystal template mixture.

5.3.1 Influence of the electrolyte concentration on the template

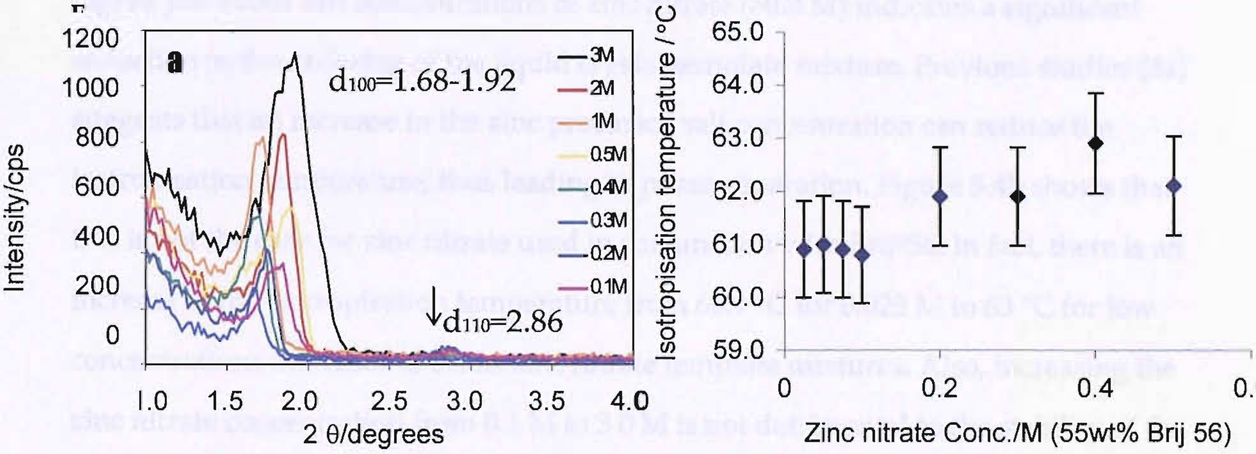

Figure 5.4: (a). Low angle XRD for a series of template mixtures containing 55 wt.% Brij®56 and 45 wt.% of solutions containing 0.1 M to 3 M $Zn(NO_3)_2$ and (b). isotropisation temperatures for template mixtures containing 0.01 M to 0.5 M $Zn(NO_3)_2$.

Chapters 3 and 4 both highlighted the effect of the type and concentration of the electrolyte components on the stability of the liquid crystal template mixture. In the following experiments Brij®56 (which is a mixture of polyoxoethylene ethers with $C_{16}EO_8$ being the most abundant) is used as an inexpensive alternative to $C_{16}EO_8$. Brij®56 was used due to the large amount of surfactant required for the deposition. No direct comparisons will be made between $C_{16}EO_8$ and Brij®56 ($C_{16}EO_8$) and their surfactant template mixtures during this research.

Figure 5.4a shows the low angle XRD patterns obtained for liquid crystal template mixtures containing 45 wt.% of 0.1 to 3.0 M zinc nitrate solutions and 55 wt.% Brij®56.

55 wt.% Brij®56 provides a well-defined hexagonal phase with this electrolyte. This was also the only mesophase examined during the course of this research.

Using zinc nitrate precursor salt solutions with concentrations from 0.1 M to 3.0 M, their low angle XRD patterns show d_{100} peaks in the range of 1.68 to 1.92 (2θ), corresponding to lattice parameters in the range of 5.25 to 4.60 nm. This is consistent with previous findings for Brij®56 (33). At concentrations >0.3 M the existence of long range ordering throughout the template mixture is revealed (figure 5.4a). This is evidenced by the existence of a second peak, with a d_{110} value, at ~2.86 (2θ), corresponding to a lattice parameter of 3.09 nm. The broadening of the d_{100} peak at higher precursor salt concentrations of zinc nitrate (>0.3 M) indicates a significant reduction in the ordering of the liquid crystal template mixture. Previous studies (34) suggests that an increase in the zinc precursor salt concentration can reduce the isotropisation temperature, thus leading to phase separation. Figure 5.4b shows that this is not the case for zinc nitrate used in conjunction with Brij®56. In fact, there is an increase in the isotropisation temperature from 60.9 °C for 0.025 M to 63 °C for low concentrations increases to 0.4 M zinc nitrate template mixtures. Also, increasing the zinc nitrate concentration from 0.1 M to 3.0 M is not detrimental to the stability of the hexagonal phase created by Brij®56, and this is supported by an increase in the isotropisation temperature from 60.9 °C at 0.025 M to 62.1 °C at 0.5 M (figure 5.4b). The effect of adding zinc nitrate to the liquid crystal mixture increases the phase stability at higher temperatures

Birefringent optical textures for all the liquid crystal mixtures investigated were investigated using POM. The long range ordering is better at lower concentrations <0.3 M evidenced by the existence of the higher order d_{110} peak in the XRD pattern, whereas the phase temperature stability range improves at higher concentrations. This can be explained by the hydration effect outlined in chapter 4, section 4.2.2. Previously (chapter 4, section 4.2.2), it was shown that a decrease in the isotropisation temperature occurs due to hydration of the mixture by the precursor salt solution, thus reducing surfactant solubility. This is known as 'salting out'. In this case, it seems that the cation

(Zn^{2+}) may act as a bridging ion between the headgroups, providing more stable micellar structures at temperatures where the phase is normally disrupted. The hydration effect caused by the NO_3^{2-} ions is negligible as it is a weakly hydrating anion and may give rise to 'salting in' (increasing the surfactant solubility and therefore the isotropisation temperature of the mixture). This is consistent with the observations made for cadmium nitrate based liquid crystal template mixtures where no significant changes in the isotropisation temperature were observed for concentrations between 0.01 and 0.1 M (chapter, section 4.2).

In chapter 4 the stabilizing effect of the nitrate ion has already been discussed with regards to the cadmium nitrate containing liquid crystal template mixtures. The size/charge ratio of the Zn^{2+} ion and the Cd^{2+} ion are similar suggesting the hydration sphere radius is also similar, therefore the effect of the nitrate ions may be the same in both mixtures, when the concentration of the salts is also equal.

5.3.2 Cyclic voltammetry of H_I-eZnO on indium tin oxide and gold

Figure 5.5a and b show cyclic voltammograms for Au and ITO electrodes in a liquid crystal template mixture consisting of 55 wt. % Brij®56 and 45 wt.% of a solution containing 0.1 M $Zn(NO_3)_2$. The cyclic voltammograms were acquired at 50 °C, using a scan rate of 20 mV s^{-1}.

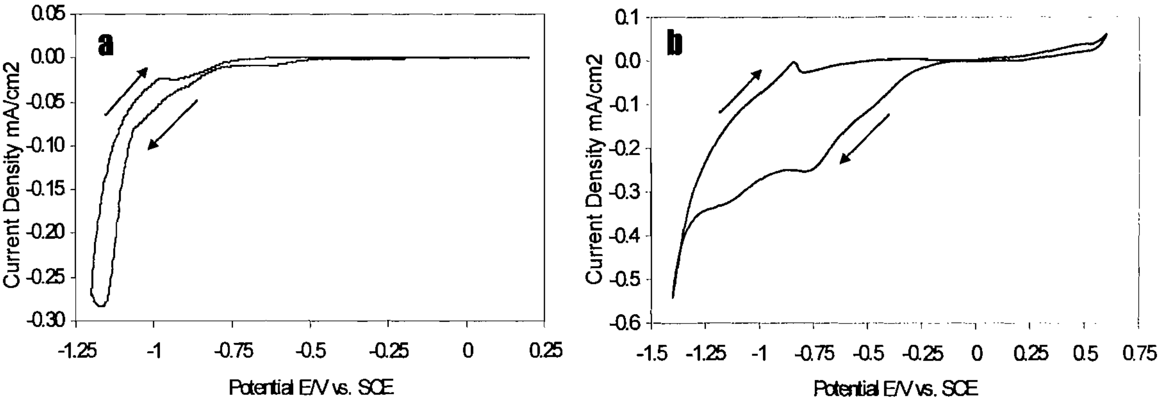

Figure 5.5: Cyclic voltammogram in the hexagonal lyotropic liquid crystalline phase of a template mixture consisting of 55 wt. % Brij®56 and 45 wt.% of a solution containing 0.1 M $Zn(NO_3)_2$ on (a). a gold electrode and (b). an indium tin oxide electrode at a scan rate of 20 mV s^{-1}.

Figure 5.5a shows that there are no voltammetric features when the potential is swept from 0.0 V to –0.5 V *vs.* SCE. At –0.5 V *vs.* SCE there is a gradual increase in the cathodic current for zinc nitrate indicating the growth of ZnO under the mechanism for zinc nitrate outlined by equations 5.3-5.6. On scanning to more negative potentials a sharp increase in the cathodic current is observed at -1.08 V *vs.* SCE. The cyclic voltammograms are comparable to those produced on SnO_2 electrodes in the production of non-mesoporous ZnO films by Gu *et. al.* (*20*). However, the presence of the surfactant in the deposition bath creates lower measured current densities than with the surfactant free solution (figure 5.1a). This is a direct result of the increased viscosity and therefore a reduction in the diffusion rate of zinc ions induced by the liquid crystal template mixture.

Figure 5.5b shows the cyclic voltammetry obtained for an ITO electrode immersed in the same zinc nitrate liquid crystal template mixture. Starting at a potential of 0.0 V *vs.* SCE and scanning to more negative potentials the onset of the cathodic peak is observed at –0.25 V. The current density increases to –0.26 mA cm^{-2} before reaching a plateau at -0.745 V compared with –0.01 mA cm^{-2} at the same potential on ITO. Lower observed current densities, by comparison to gold, have already been observed with Te on ITO in chapter 3 and can be attributed to the lower conductivity. The current continues to increase from -1.0 V *vs.* SCE. Finally there is a sharp increase at -1.3 V from a current density of -0.4 mA cm^{-2} *vs.* SCE. This increase in the current density corresponds to hydrogen evolution according to equation 5.7:

$$H_2O + e^- \xrightarrow{\qquad\qquad} OH^- + \tfrac{1}{2} H_2 \qquad [5.7]$$

At potentials >-1.3 V *vs.* SCE the electrode also turned dark grey suggesting the deposition of metallic Zn, by the reduction of Zn^{2+} at the ITO surface. This was observed by Lincot *et. al.* with SnO_2 electrodes and a blackening of the surface. As with the cyclic voltammogram recorded for an Au electrode in 0.1 M ZnO a small anodic peak is observed at -0.875 V *vs.* SCE and, as before, this maybe attributed to the oxidation of Sn (*28*). Due to the stability of the electrodeposited zinc oxide, the stripping of the film is not expected. The cyclic voltammogram is then featureless until -0.13 V *vs.* SCE where a gradual increase in the current density is shown.

5.3.3 TLCT using low temperature conditions

Previous research acquired during the electrodeposition of CdTe (and to a lesser extent Te) suggested that the electrodeposition of mesoporous semiconductors (and metalloids) could be carried out at significantly lower temperatures (ambient as appose to 75 °C) by comparison to the bulk deposition, owing to the reduction in the diffusion rate of the reactants to the electrode surface.

Initially, ZnO electrodeposition experiments were conducted at room temperature as elevated temperatures can lead to the evaporation of water from the liquid crystal template mixture resulting in phase changes.

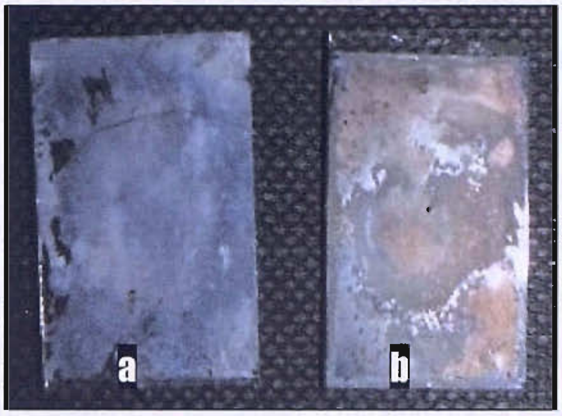

Figure 5.6: Digital images of thin films electrodeposited on ITO substrates at (a). -1.2 V and (b). -1.4 V *vs.* SCE from mixtures containing 45 wt. % of a 0.1 M zinc nitrate solution and 55 wt.% Brij®56 .

Attempts to electrodeposit H_I-e ZnO film were carried out using three different potentials, -1.0, -1.2 and -1.4 V *vs.* SCE and using a plating bath containing 45 wt. % of a 0.1 M zinc nitrate solution and 55 wt.% Brij®56, at a temperature of 25 °C. Figures 5.6a and b show H_I-e ZnO films electrodeposited at -1.2 and -1.4 V *vs.* SCE on ITO, at room temperature, respectively. The images show the inhomogeneous nature of the films, with areas of the ITO still visible. Films deposited at -1.0 V *vs.* SCE from mixtures containing 55 wt. % Brij®56 of a 0.1 M zinc nitrate solution and 55 wt.% Brij®56 did produce any deposition films when viewed using SEM or by EDX analysis. Although, more negative potentials (-1.2 V and -1.4 V) were used in an attempt to electrodeposit mesoporous ZnO this was not successful.

Potential, E/V *vs.* SCE	Charge density/Ccm^{-2}	Film Thickness Estimation from Charge/μm
-1.0	0.16	0.147±0.027
-1.2	0.58	0.527±0.035
-1.4	2.16	1.122±0.043

Table 5.1: ZnO film thickness dependence on electrodeposition potential at 25 °C.

The films were inhomogenous, non transparent, grey, adherent films were deposited onto the ITO surface (figure 5.6a and b). Table 5.1 shows the estimated film thickness for the films deposited at 25 °C. Also, the images show that at room temperature the films did not deposit uniformly. Grey films are an indication of the electrodeposition of zinc, zinc hydroxide or zinc oxyhydroxide occurs as opposed to zinc oxide (22), and the EDX results for electrodepositions at potentials of –1.2 and -1.4 *vs.* SCE showed high levels of Zn only. Higher temperatures (>28 °C) have been used previously used to improve the film thickness (24). Films grown at 28 °C have been shown to saturate at a thickness of 30 nm and Lincot *et. al.* described this as blocking behaviour on current evolution (22, 24). However, it must be noted that these films were grown using surfactant free solutions and concentration. This may have been an effect at deposition potentials of -1.0 V *vs.* SCE, where temperature, as well as the electrode potential, was not sufficient to allow nucleation to be sustained. The critical effect of temperature has already been observed by Lincot *et. al.* (22, 24). They suggest that temperatures greater than 34 °C are required for nucleation and growth of ZnO and 40 °C for the production of transparent ZnO films of good crystallinity. Much of the supporting literature states temperatures of ≥65 °C for the growth of ZnO films. Although, Zhang (35), Li (36) and Mei (37) have shown that ZnO films can be produced at <20 °C, but this is usually followed by a method of annealing.

Attempts to electrodeposit mesoporous ZnO films, at a potential of 1.0 V *vs.* SCE and room temperature, from liquid crystal template mixtures were unsuccessful. While at more negative potentials of –1.2 to –1.4 V *vs.* SCE the films produced were grey, non-uniform in morphology and metallic. This suggest that the successful deposition of ZnO required higher temperatures to promote both zinc and oxygen deposition and to increase the reaction rate. The following sections will utilize higher temperatures in order to facilitate the electrodeposition of mesoporous ZnO.

5.3.4 Influence of deposition potential

Figure 5.7 shows the current density as a function of the deposition potential for the electrodeposition of mesoporous ZnO. The current density is directly related to the rate of film deposition. The current density was measured 1000 seconds after the initial potential step had taken place. In general, the current density increased as the deposition potential became more negative. At potentials between -0.9 and -1.045 V *vs.* SCE the current density remained almost constant at -0.5 C cm^{-2}. At potentials between -1.045 V and -1.145 V *vs.* SCE the charge density increases almost linearly from -0.4 C cm^{-2} to a value of 9.0 C cm^{-2}. Previous studies have claimed that a charge density of -1.0 C cm^{-2} provided the most successful depositions in terms of crystallographic orientation and uniformity of ZnO deposition (*9, 11, 21, 24, 30, 38, 39*).

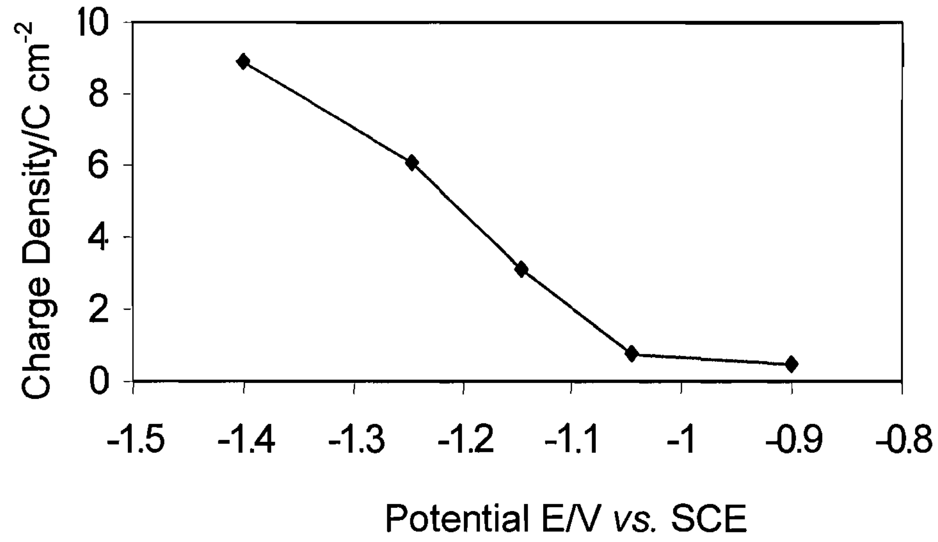

Figure 5.7: Current density as a function of deposition potential at 50 °C for the electrodeposition of ZnO from a template mixture containing 0.1 M $Zn(NO_3)_2$ (45wt.%) and Brij®56 (55 wt.%).

The optimum conditions for the current density can also be seen by SEM images showing the effect of current density on the electrode surface. Figure 5.8 shows the surface morphologies of three H$_I$-eZnO films deposited as a function of electrodeposition potential. Section 5.3.2 showed that the electrodeposition of bulk ZnO results in the formation of hexagonal platelets. Here we see that at -0.945 V *vs.* SCE the film is thin and the ZnO deposit is predominately concentrated in the centre of the electrode. The corresponding SEM image shows an uneven film. As the deposition potential becomes more negative the coverage of the film increases.

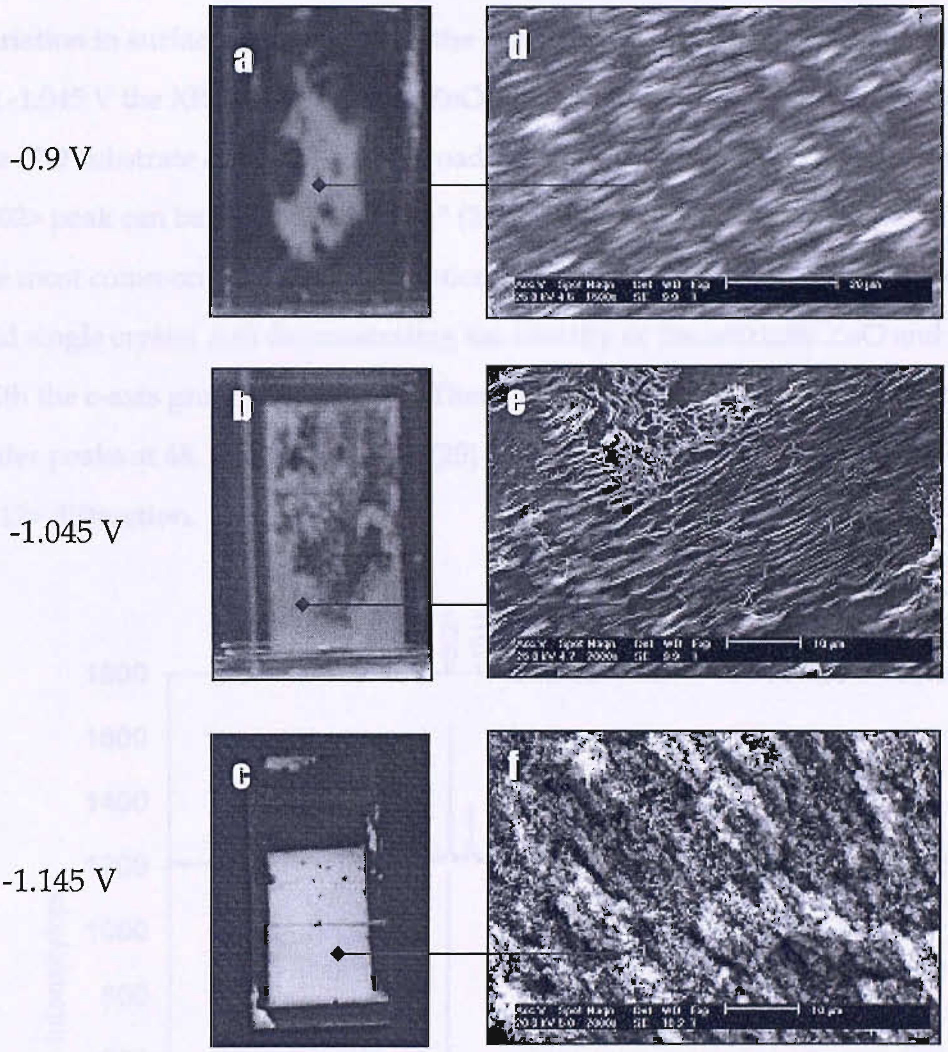

Figure 5.8: Digital images (a-c) and SEM images (d-f) of H_I-eZnO films electrodeposited on ITO at -0.945 V, -1.045 V and 1.145 V *vs.* SCE at a temperature of 50 °C.

It appears that the overall thickness and also that the overall coverage improved at a potential of -1.045 V *vs.* SCE. None of the SEM images seen in figure 5.8 exhibited any of the characteristic hexagonal phase morphologies observed with the electrodeposition of bulk ZnO (section 5.3). From the graph in figure 5.7, the desired charge density should be ~3 C cm^{-2}, which would provide entire coverage of the electrode surface.

The crystal structure of the H_I-e ZnO films, electrodeposited as a function of the electrode potential was verified by wide angle XRD. Three films were analysed at -1.245, -1.145 and -1.045 V *vs.* SCE, 50 °C deposited for a duration of 18000s. The variation in surface morphology in the ZnO films as a function of potential is evident. At -1.045 V the XRD pattern of the ZnO film is slightly hidden by the background of the ITO substrate and shows as a broad peak between 20 and 30° (2θ). However, the <002> peak can be identified at 33.4 ° (2θ). From previous studies (*39*), the <002> peak is the most common crystallite orientation (on a number of different substrate e.g. ITO and single crystal Au) demonstrating the identity of the wurtzite ZnO and associated with the c-axis growth orientation. There are also a number of other significant higher order peaks at 48, 57.5, 63 and 68.5 (2θ) corresponding to the <102>, <110>, <103> and <112> diffraction.

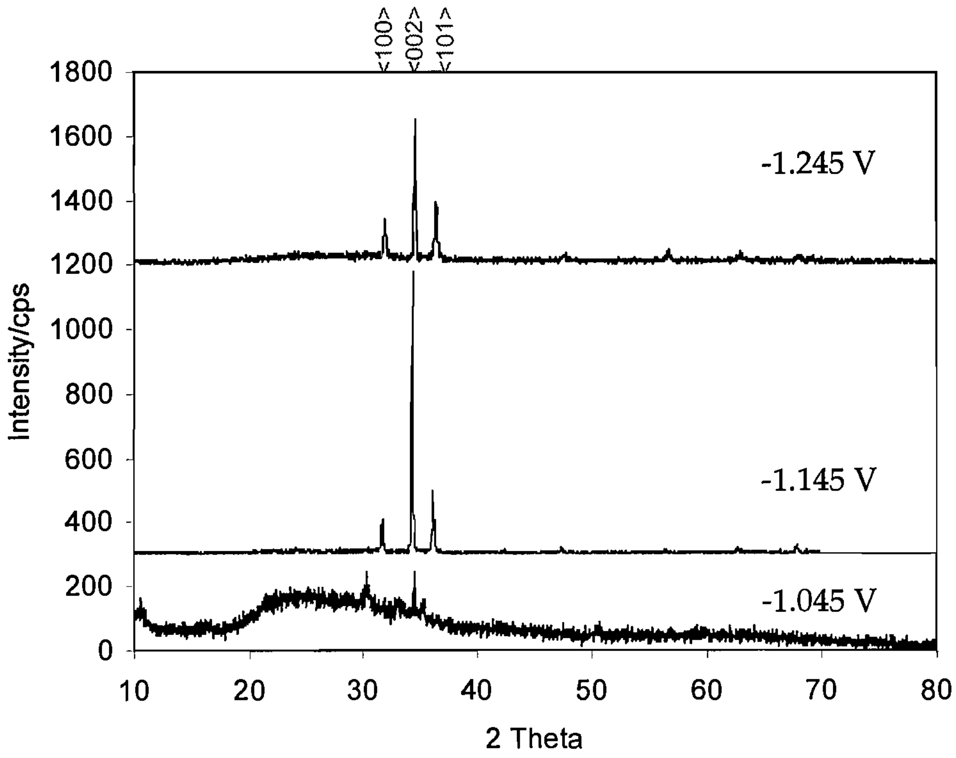

Figure 5.9a: Wide angle XRD pattern of H_I-eZnO on ITO deposited at -1.045 V, -1.145 V, -1.245 V *vs.* SCE from a mixture comprised of 55 wt. % Brij®56 and 45 wt. % of a solution containing 0.1 M Zn $(NO_3)_2$ at a temperature of 50 °C.

Figure 5.9b shows a wide angle XRD diffraction pattern for the ZnO film deposited at – 1.145 V *vs.* SCE, using a concentration of 0.1 M zinc nitrate. This is identical to the one shown in figure 5.9a and it was possible to assign all the peaks for this ZnO film using a ZnO powder reference (table 5.2). Figure 5.9b shows the wide angle XRD pattern over the range of 20 to 70° (2θ) again for which film and which substrate shows a very intense <002> peak indicating preferential ordering and also confirms the existence of zinc oxide on ITO (*9, 23*). The existence of other peaks (e.g. <101> and <100>) does suggest the polycrystalline nature of the film, but is in line with previously reported results obtained on a variety of different substrates (*10*). Higher order peaks <102>, <110>, <103>, <203>, <112> and <210> is observed and are consistent with previous findings. The results shown here suggests the dependence of the preferential orientation of ZnO film growth on the deposition potential (*9, 11, 21, 24, 30, 38, 39*).

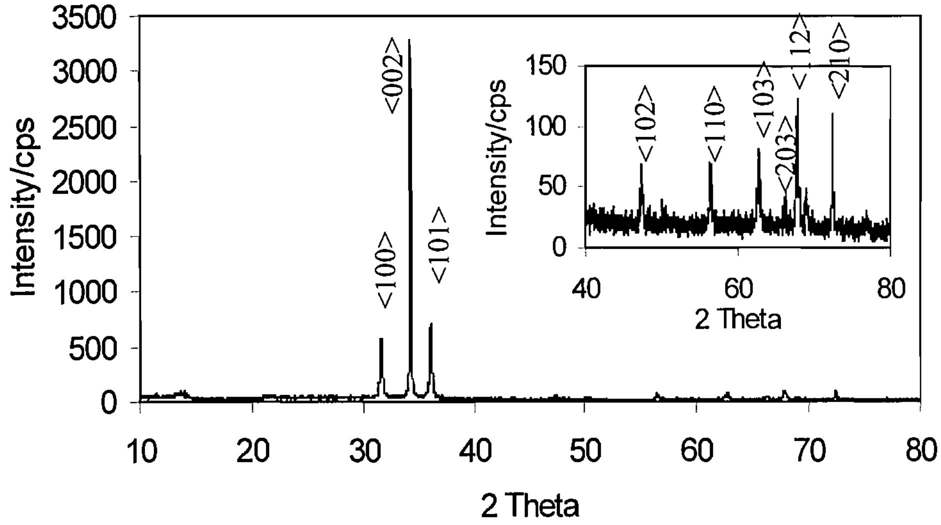

Figure 5.9b: Wide angle XRD pattern of a H_I-eZnO deposited on indium tin oxide coated glass from a hexagonal phase template mixture consisting of 55 wt.% Brij®56 and 45 wt.% of a 0.1 M solution containing $Zn(NO_3)_2$ at 50 °C and at a potential of -1.145 V *vs.* SCE. Inset: shows 40 to 60 (2θ) and higher order diffraction peaks.

Table 5.2 shows that the results are comparable to those of bulk ZnO on ITO grown previously by (*28*). These results fully confirm the XRD results in figure 5.9a and b for the ZnO film deposited at -1.045 V *vs.* SCE.

hkl	d-spacing (Å) Zinc oxide powder	d-spacing (Å) Zinc oxide film	d-spacing (Å) Zinc oxide mesoporous film
(100)	2.81	2.81	2.83
(002)	2.60	2.61	2.62
(101)	2.48	2.48	2.49
(102)	1.91	1.91	1.91
(110)	1.62	1.62	1.63
(103)	1.48	1.48	1.48
(203)	1.41	-	1.41
(112)	1.38	1.38	1.38
(210)	1.35	1.35	1.36

Table 5.2: d-*spacings* for hkl groups of various zinc oxide materials: (a). powder, (b). electrodeposited bulk film and (c). electrodeposited mesoporous film.

5.3.5 Influence of zinc nitrate concentration on ZnO film quality

The results of the SEM images of H_I-eZnO films grown on ITO from liquid crystal template mixtures containing concentrations of 0.1 to 1.0 M zinc nitrate are shown in figure 5.10. Electrodeposition of H_I-eZnO was carried out at –1.145 V *vs.* SCE for 15 hrs at 50 °C. The film thickness as determined the charged passed was 14, 23 and 5.7 μm for 0.1, 0.2 and 0.3 M concentration solutions, respectively. The films are uniform in appearance. At concentrations $\leq$0.3 M the films were white, with a granular appearance, and light scattering. At 1.0 M the deposited film is grey and suggestive of

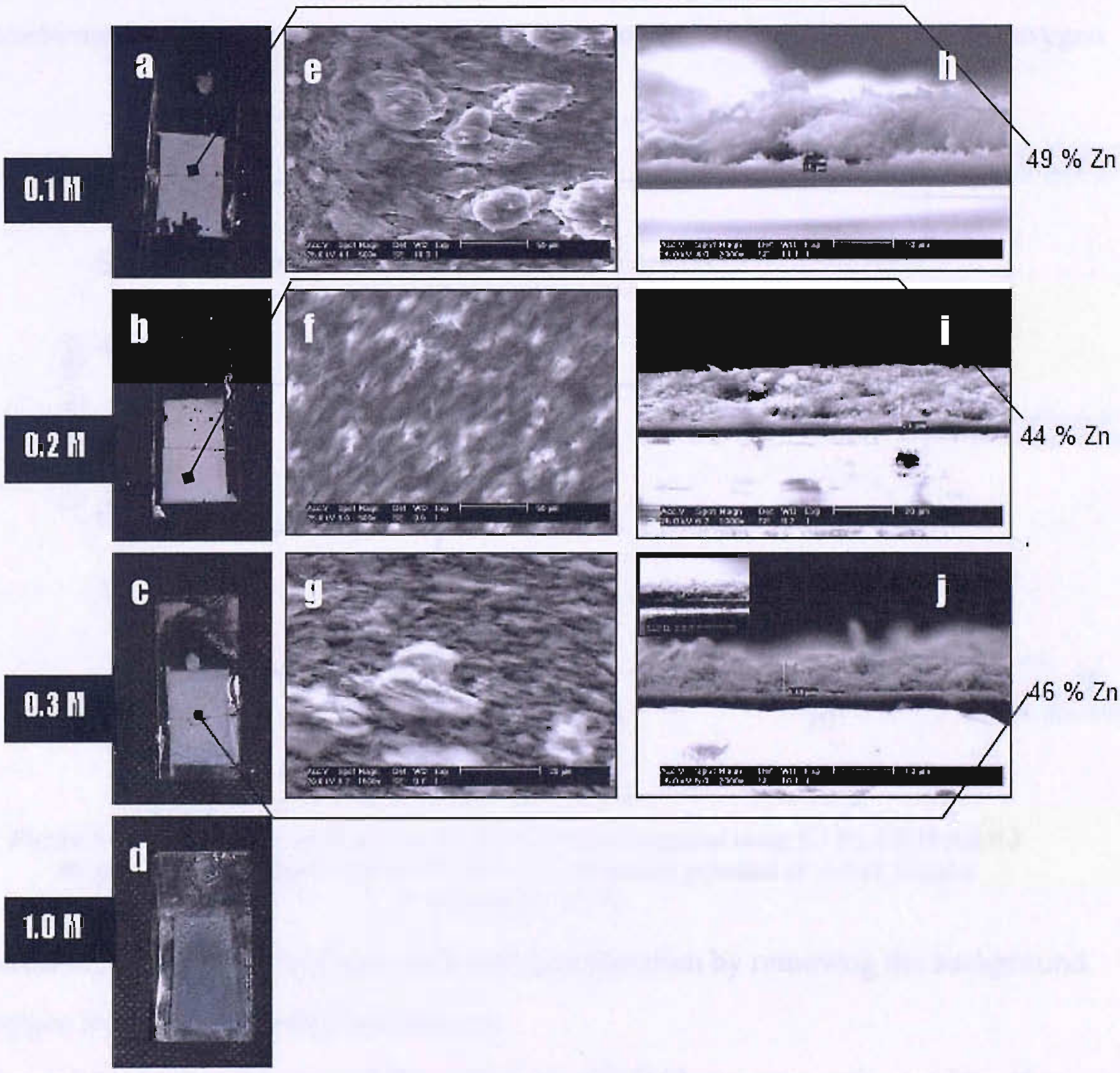

Figure 5.10: Digital images of H_I-eZnO films (a-d) and SEM images showing the variation in surface morphology (e-g) and the cross section (h-j) as a function of the zinc nitrate concentration in the liquid crystal template mixture containing 55wt.% Brij®56 and 45wt.% of a solution containing various concentrations zinc nitrate. Films were deposited for 15 hrs at 50 °C at a potential of –1.145 V *vs.* SCE on ITO glass. The approximate zinc content for various positions on the film is given from EDX analysis.

metallic zinc (*40*). The appearance of a grey film has been noted in previous papers all suggesting the deposition of metallic zinc through reaction 5.8.

$$Zn^{2+} + 2e^- \longrightarrow Zn \qquad [5.8]$$

Cross sectional SEM images reveal the dendritic and porous nature of the films. None of the films presented in figures 5.10h-j are flat. EDX measurements were taken at various points on the film's surface (as indicated by the arrow) revealing the percentages of zinc present by comparison to oxygen. The results are close to being stoichiometric. Errors can occur as the oxygen from the ITO could influence the oxygen percentage results, but this was taken into consideration by removing the background oxygen from the ITO before calculations.

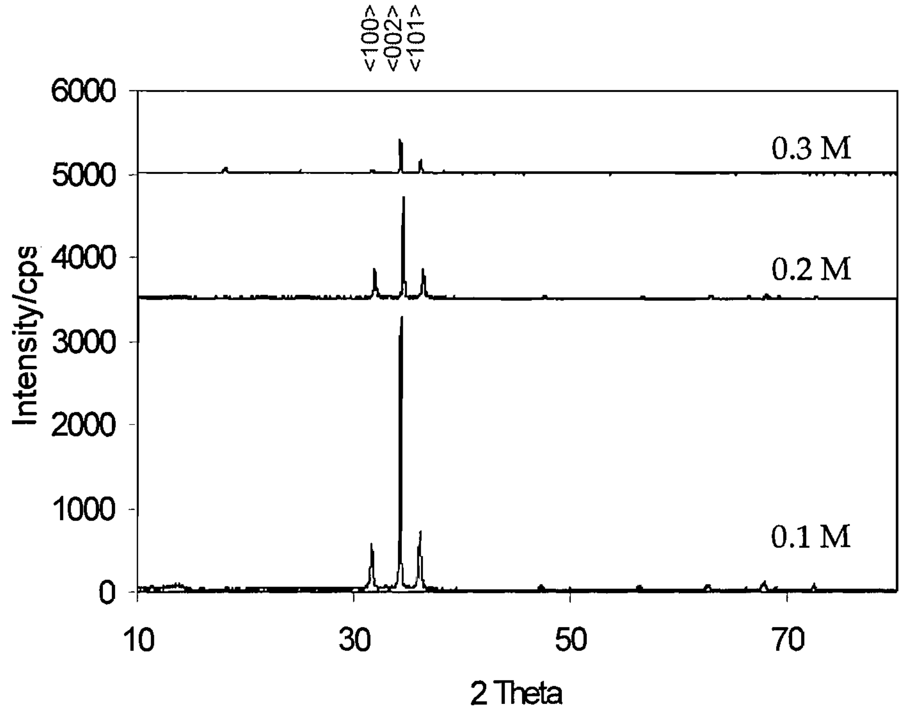

Figure 5.11: Wide angle XRD patterns for H_Ie-ZnO films prepared using 0.1 M, 0.2 M and 0.3 M solutions, electrodeposited on ITO films at a deposition potential of -1.145 V and a temperature of 50 °C.

Figure 5.11 shows wide angle XRD patterns for ZnO films grown using various zinc nitrate concentrations of zinc nitrate of 0.1 , 0.2 and 0.3 M. Table 5.3 shows the change in peak intensity ratio for the three primary diffraction order XRD peak for zinc oxide (002, 100 and 101). Due to the thickness of the films (5.7 to 23 μm) none of the peaks

Table 5.3: Variation of hkl of electrochemically deposited ZnO using different concentrations of precursor salt solutions.

Conc. $[Zn]^{2+}$		100	002	110	SEM Film Thickness/μm
0.10	Peak intensity	512	3282	679	14
	Ratio to 002	6.41	-	4.83	
0.20	Peak intensity	344	1209	364	23
	Ratio to 002	3.51	-	3.32	
0.30	Peak intensity	43	399	157	5.7
	Ratio to 002	9.28	-	2.54	

originating from the ITO substrate were observed. Previously it has been shown that thicker samples have preferential orientation of the films along the <002> plane (*30*). The electrodeposited films of zinc oxide have a preferred orientation in the <002> *c-axis* at 0.1 M. On increasing the concentration, film orientation tends towards the <110> direction and away from the <100> orientation. This could be a factor asscociated with the film thickness or the growth rate of the films promoting different growth structures. The preferential orientation of electrodeposited ZnO film changes with the concentration of the precursor salt. These changes occur on increasing the concentration from 0.1 to 0.3 M. The preferred orientation remains <002> at all concentrations, however the <100> peak becomes more predominent as the concentration of ZnO is increased.

Previously, for the electrodeposition of CdTe it was shown that in order to achieve high quality optical measurements electrodeposited films must be flat, defect free and not light scattering. Therefore, the deposition conditions were modified in an attempt to improve the film morphology.

5.3.6 Deposition time

Experiments were carried out to identify the extent of control over the deposited H$_I$-eZnO film thickness by using concentrations of 0.1 and 0.01 M zinc nitrate, a deposition potential of -1.145 V *vs.* SCE, a temperature of 50 °C (figure 5.12) and a variation in the deposition duration. The H_I-eZnO film thicknesses were measured from the charge passed during the electrodeposition (see section 3.4.1). The film thicknesses of the H_I-eZnO films appear to follow a linear trend over the 54000 second period using a concentration of 0.1 M zinc nitrate. Using 0.01 M zinc nitrate this trend is not observed; at longer deposition times (26000 seconds) the rate of deposition decreases and the film thickness becomes static. This is a direct indication of the depletion of the precursor salts in the template mixture. The 0.1 M zinc nitrate liquid crystal template mixture is not depleted after 26000 seconds, and as the electrodepositions require up to 54000 s, this suggests that template mixtures using 0.1 M zinc nitrate solution will provide a sufficient deposition source.

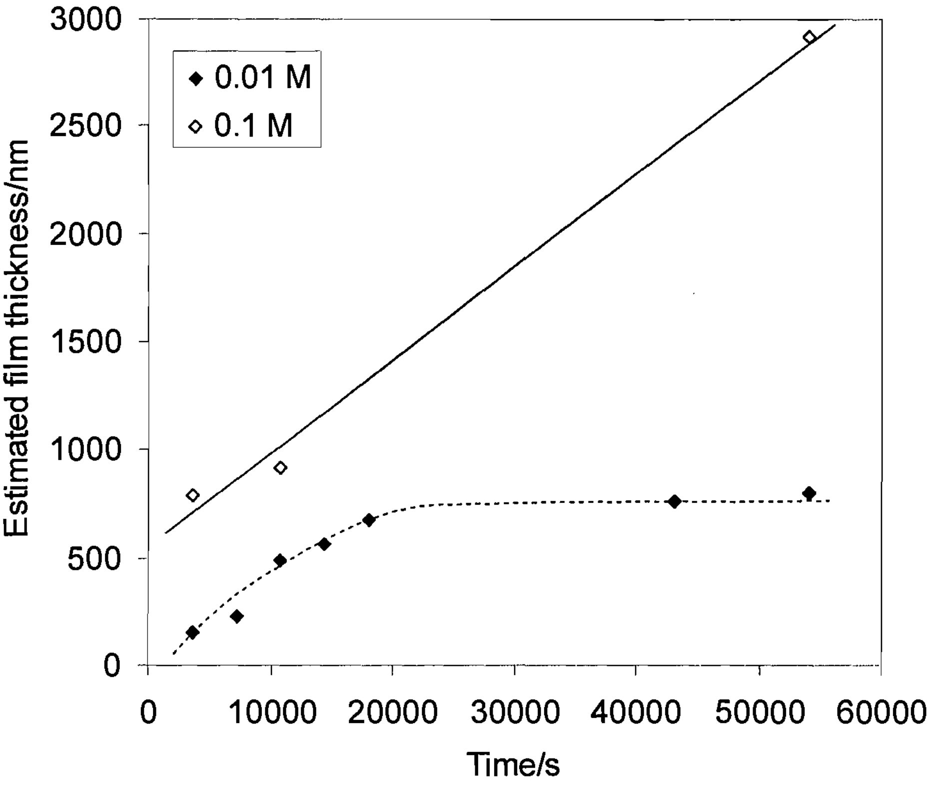

Figure 5.12: Estimated H_I-eZnO film thicknesses as a function of deposition times using 55 wt.% Brij®56 and 45 wt.% of a solution containing 0.01 M or 0.1 M zinc nitrate. The films were electrodeposited at -1.145 V *vs.* SCE and at a temperature of 50 °C.

5.3.7 Potential modulation

Pulsed electrodeposition is applied to deposit metals, alloys and metal oxides in an attempt to improve the characteristics of the material. Lower porosities (i.e. porosities not induced by surfactant templates), higher corrosion resistances but more importantly smoother films are the superior qualities obtained by other researchers using this technique (*41*). This technique can also be applied to promote nucleation, the formation of fine crystals, and a decrease in defects (e.g. pinholes) .The advantage of pulsed deposition is the apparent super purification (contaminant free) of deposits and the improvement to chemical and physical properties (*42*).

The effect of pulsed potential deposition on film morphology for ZnO films was studied and compared against films prepared by the constant potential method. Figure 5.13 shows the pulsed potential waveform for the modulated potential experiment and figure 5.14 shows the current time transient for the waveform. The pulse time for deposition can also be regulated using these conditions (i.e. concentration of precursor salt, temperature etc.). A potential (E_{dep}) of –1.145 V *vs.* SCE, 0.1 M, and 50 °C is optimal for the deposition of H_I-eZnO with E_{off} (the open circuit potential) as +0.3 V, in accordance with Lee and Tak (*30*), where the current was ~0. The total time for each experiment was 15 hours, with a deposition (E_{dep}) time of 1 hour and an E_{off} time of two hours. Longer relaxation times than used by Lee and Tak (*30*) were required due to the viscous nature of the liquid crystal template mixture. Increased viscosity of the solution would mean longer relaxation times are required for the concentrations to equilibrate.

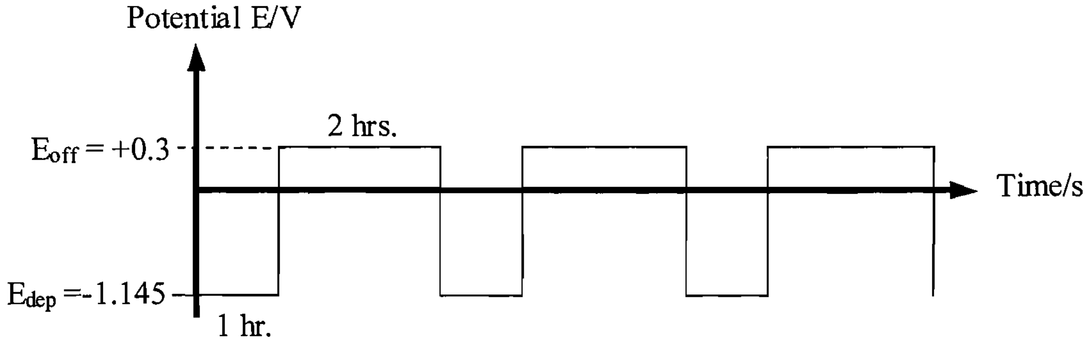

Figure 5.13: Rectangular pulsed wave and pulse parameters for the pulsed potential electrolysis.

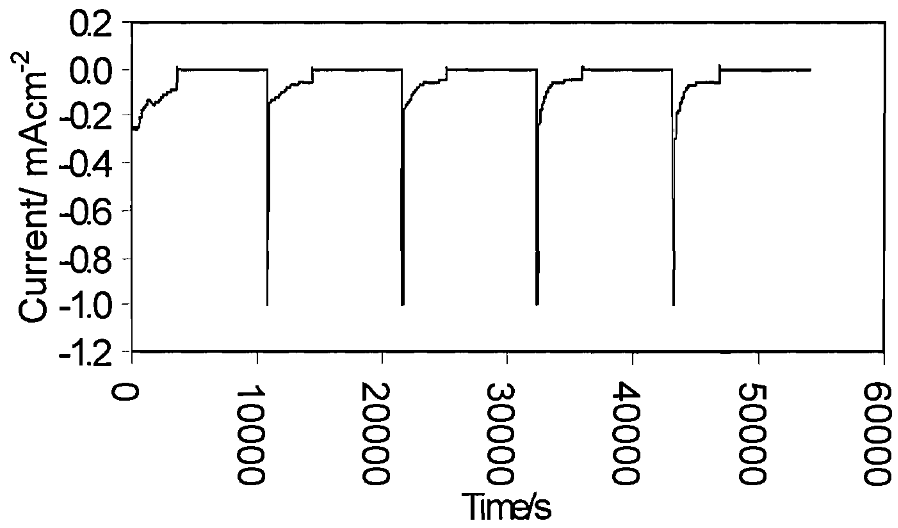

Figure 5.14: Current-time transient for the pulsed electrodeposition of zinc oxide for a solution containing 50 wt.% 0.1 M zinc nitrate and 50 wt.% Brij®56.

Figure 5.15 shows the wide angle XRD patterns for H_I-eZnO films prepared at a constant potential of -1.145 V and using modulated potentials of 0.3 and -1.145 V *vs.* SCE. The modulated potential experiment was carried out using the conditions shown in figure 5.13. Both films showed three intense diffraction peaks for ZnO, which are - <002>, <100> and <101>. These were observed previously in figure 5.9b for a H_I-eZnO film deposited at -1.145 V *vs.* SCE and in the literature. The ZnO film deposited using a modulated potential is void of all higher order diffraction peaks indicated by (*) in figure 5.15. Also, while films prepared using constant potentials (Figure 5.9a) all

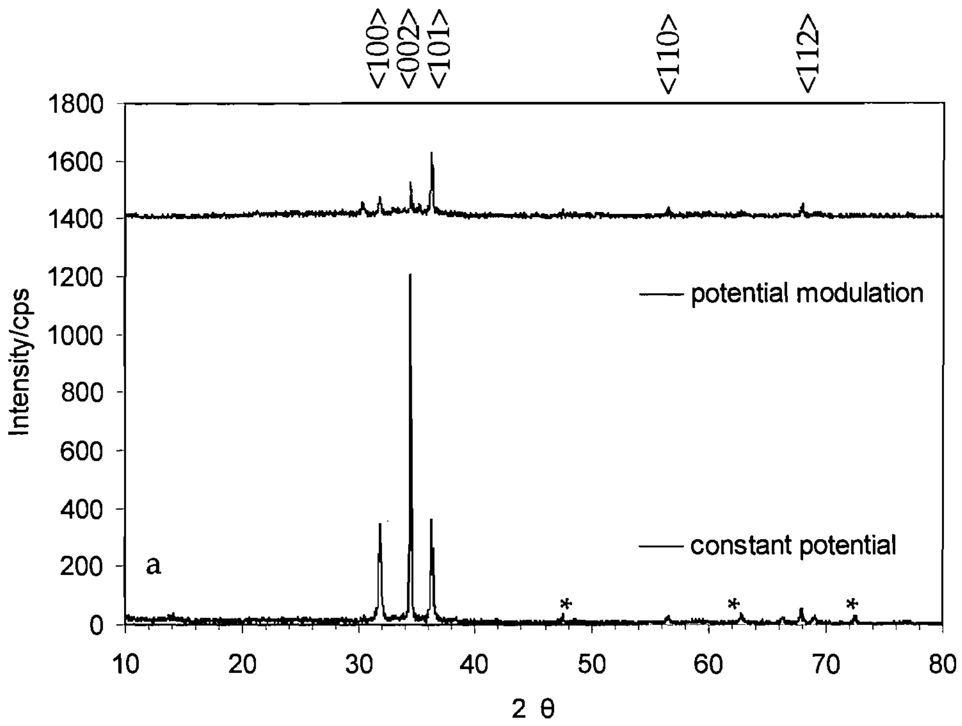

Figure 5.15: XRD patterns for H_I-eZnO films prepared at 50°C, (a). a deposition potential of -1.145 V with a pulse period of 3600 seconds and a open circuit potential of +0.3 V with a period of 7200 seconds and (b). a constant potential of -1.145 V *vs.* SCE.

exhibited preferential orientations of <002>, the modulated film showed a preferential orientation of <101>, in agreement with Maeda (*30*). The extent of this deviation was not clarified further. From previous research (*39*) it is assumed that the preferential orientation of the ZnO film could be controlled by further modifications to the pulse conditions. The deviation from the preferred orientation of <002> to <101> in the potential modulated film and this was further confirmed by an observed difference in SEM images shown in figure 5.16. Figure 5.16a shows the modulated potential ZnO film appeared denser and less granular on the electrode than the constant potential mesoporous ZnO film (5.16b). Figures 5.16c and d show the surface morphologies of the potential modulated and non-potential modulated ZnO films. Crystal growth is observed on both surfaces. Figures 5.15e and f show the cross sectional images of a constant potential deposited film and a modulated potential deposited film. The film grown using a modulated potential resulted in a ZnO film which appeared to be more densely packed with some crystallite growth on the top.

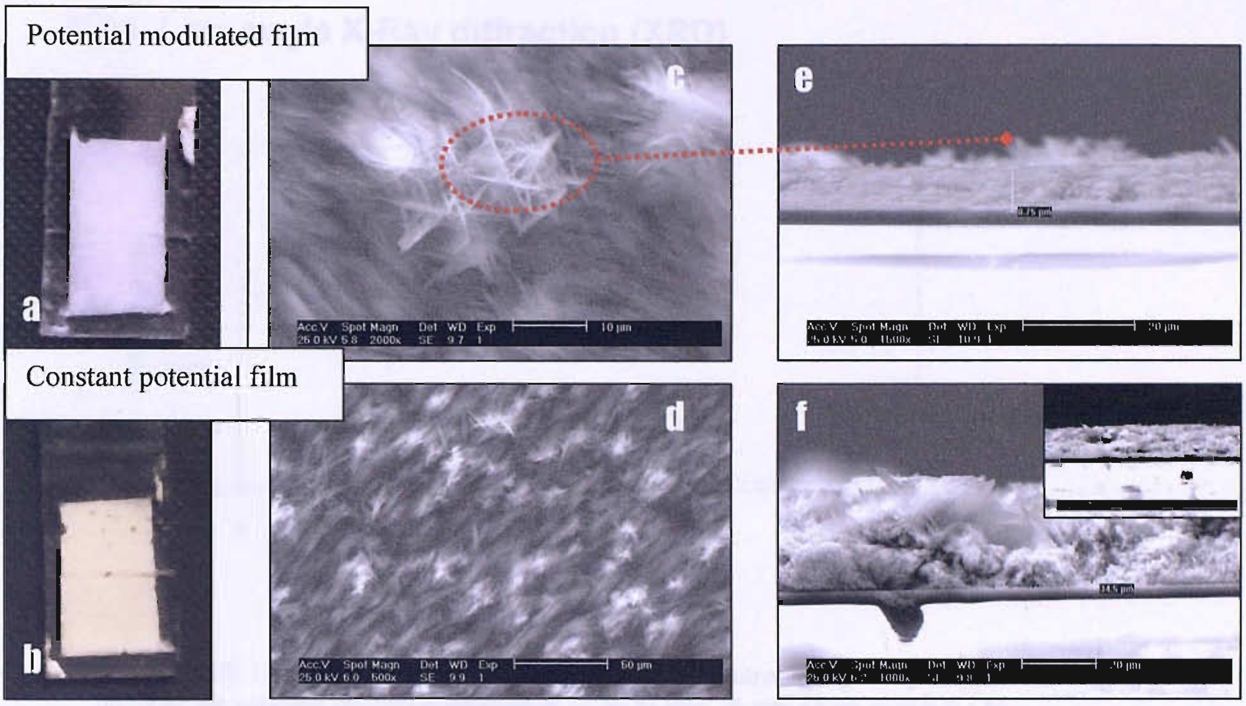

Figure 5.16: Images a, c, and e are digital, SEM and a SEM cross-section of the modulated potential ZnO film respectively. While images a, c, and e are a digital, SEM and SEM cross-section of the constant potential ZnO film.

5.3.8 Summary

Pulse deposition of mesoporous zinc oxide films produced films that were more compact than the non-pulsed counterparts using the pulse potential waveform described in section 5.4.7. Although this was the case, the wide-angle XRD data showed that the pulsed films were of a lower crystal quality, with poor orientation of the growth orientation in the film. These initial results do indicated that pulse plating can provide a method of orientation modification of the mesoporous zinc oxide films.

5.4 CHARACTERISATION OF MESOPOROUS ZnO FILMS

5.4.1 Low angle X-Ray diffraction (XRD)

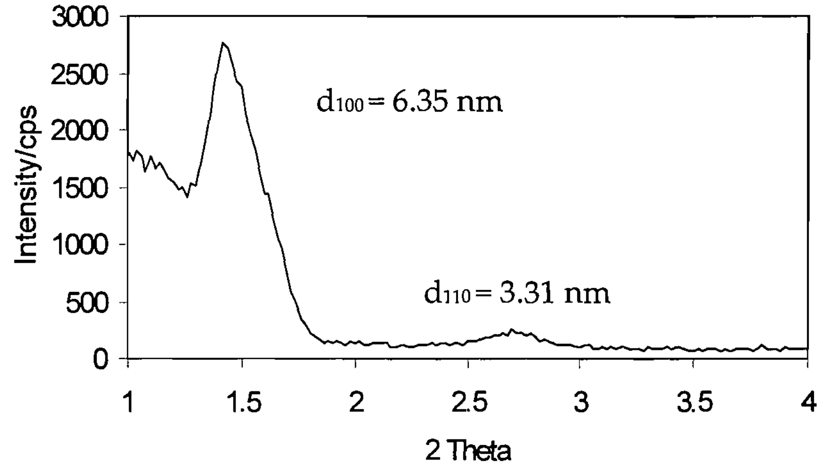

Figure 5.17: Low angle XRD pattern for the hexagonal lyotropic liquid crystalline phase of the template mixture consisting of 55 wt.% Brij®56 and 45 wt.% of a 0.1 M solution containing $Zn(NO_3)_2$ at a temperature of 50 °C.

Figure 5.17 shows the low XRD diffractograms obtained for the hexagonal phase of the template mixture using 55 wt.% Brij®56 and 45 wt.% of a 0.1 M zinc nitrate solution. The two diffraction peaks correspond to the d_{100} and the d_{110} diffraction planes of the hexagonal template with a d-spacing of 6.09 nm and 3.31 nm, respectively. These *d*-spacings are in the approximate ratio of 1:1√3, as expected for the hexagonal liquid crystalline phase. The results shown here are in good agreement with those observed for mesoporous films (see Chapter 4, table 4.2).

Figure 5.18 shows a diffraction pattern for an electrodeposited H_I-eZnO film on gold. We can identify a well-defined first order diffraction peak corresponding to a *d*-spacing of 6.35 nm and a pore-to-pore spacing of 7.33 nm. The peak position of the film is similar to that of the template mixture in figure 5.17, providing evidence for direct templating. The *d*-spacing for the H_I-eZnO films is also consistent with the values obtained for the primary reflection peak of metals, semiconductors and metal oxides with a porous nanostructure derived from the surfactant template mixture shown in table 4.2.

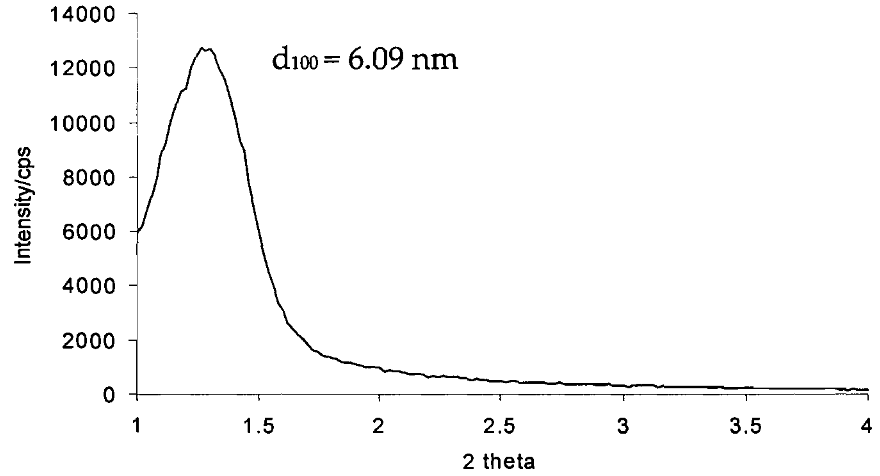

Figure 5.18: Low angle XRD pattern of H_I-eZnO deposited at 50 °C on gold from a hexagonal phase template mixture consisting of 55 wt.% Brij®56 and 45 wt.% of a 0.1 M solution containing $Zn(NO_3)_2$.

5.5 Electrodeposition of optically transparent mesoporous zinc oxide films by direct liquid crystal templating

5.5.1 Sodium ligninsulfonate as a levelling agent

The use of sodium ligninsulfonate in plating baths as a additive to reduce dendritic growth enhancing the quality of the film surface is evident (43). Here we will study the effect of sodium ligninsulfonate as a leveling agent in the electrochemical fabrication of mesoporous ZnO films.

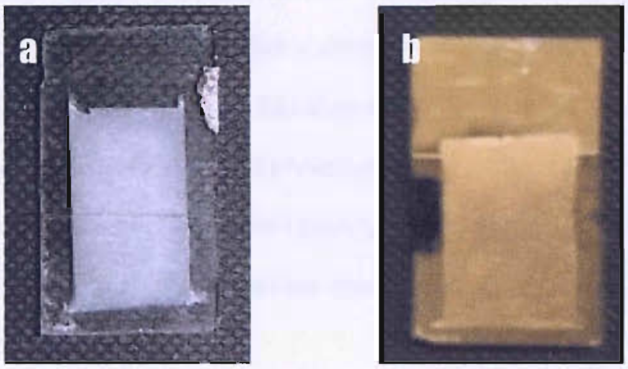

Figure 5.19: Digital images of Hi-eZnO films electrodeposited at -1.145 V and 50 °C on (a). ITO and (b). Au

One of the major problems faced with the electrodeposition of mesoporous zinc oxide in the domains of a liquid crystal template is the morphology of the deposited film. By comparison, H$_I$-eCdTe films have been show to produce highly reflective films with a mirror type finish without the use of elevated temperatures. The electrodeposition of mesoporous zinc oxide is highly reproducible with a clearly defined crystal structure by wide angle XRD. EDX measurements showed the films contained zinc and oxygen in near stoichiometric amounts. However, the films produced were commonly granular and not transparent in appearance. UV-Vis spectroscopy of these films exhibited no clear interference fringes, which provides evidence for flat films. The white granular mesoporous ZnO films produced by TLCT are light scattering and in order to produce films with better optical quality (e.g. films that are transparent in the visible region of the electromagnetic spectrum) the deposition conditions must be changed. Figure 5.19a and b show digital images of two ZnO films electrodeposited on

ITO and gold. The images show dense, white non-transparent ZnO films. Izaki *et. al.(21)* have discussed the possibility of improving the film transparency. This was carried out using a two-potential electrolysis method whereby a certain charge is passed at an initial deposition potential to promote nucleation. The potential was then stepped to a more positive potential in order to sustain growth. The method provided an increase in film growth by 20%, however the UV-Vis spectra of the films revealed no interference fringes. The electrochemical conditions for optical quality films have been highlighted by Pauporte (*21*), and Mari (*16*) with a distinct need for post-deposition treatment of ZnO samples. For example, for non-annealed samples the absorption edge is not always prominent and transmission is recorded to be as low as 10%. This could be directly related to the existence of other particles such as hydroxides, which are created during the deposition process, but does suggest that annealing the samples may improve the transparency of the films (*21*). Finally, Yamamoto *et. al.* have reported that ZnO transparency is a direct factor of the films roughness. They suggested that the surface must be void of crack or pits in order to improve the transparency (*44*).

In an attempt to improve the morphology of the films and to create more optically transparent films sodium ligninsulfonate was added to the electrolyte mixture at various concentrations in order to control the growth rate of ZnO and produce flatter more optically transparent films. The structure of lignin is shown in Figure 5.20. During electrodeposition nucleation occurs at surface site growth centres on working electrodes. These centres encourage further growth perpendicular to the surface as mass transport increases. The sodium ligninsulfonate attaches to the nucleated sites; reducing growth perpendicular to the substrate and forcing lateral growth at the substrate surface/areas which has no nucleation sites (*43*).

The following experiments were carried out using a 0.1 M zinc nitrate electrolyte solution (45 wt. %) and Brij®56 (55 wt. %), at 50 °C using a SCE reference electrode. Depositions have been carried out using 1.0 g dm^{-3}, 2.5 g dm^{-3} and 5.0 g dm^{-3} of the sodium ligninsulfonate at -1.145 V, -0.845 V and -0.745 V *vs.* SCE.

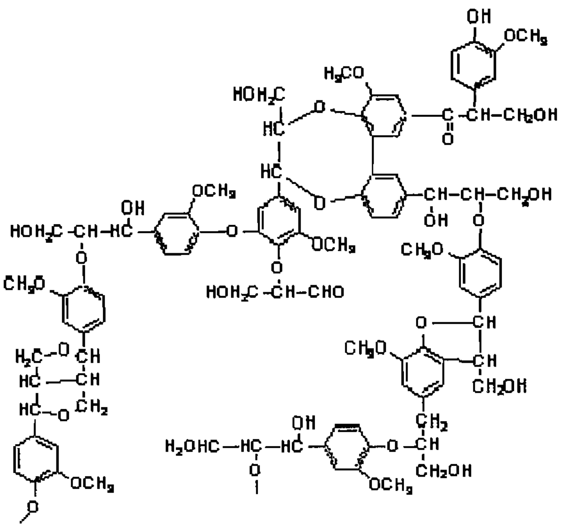

Figure 5.20: A small section of a lignin polymer, illustrating some typical chemical linkages seen in lignin. These compounds make up the second most abundant class of chemicals found in wood. Lignosulfonates are produced as sodium, calcium, magnesium or ammonium salts and can be converted to other salts through base-exchange procedures.

5.5.2 Sodium ligninsulfonate effects:

5.5.2.1 Sodium ligninsulfonate and liquid crystal template mixtures

Figure 5.21 shows the X-ray diffractograms for liquid crystal templates prepared using 45 wt.% of a 0.1 M zinc nitrate and 1.0 or 5.0 g dm^{-3} sodium ligninsulfonate solution and 55 wt.% Brij®56. The template mixtures prepared with 1.0 g dm^{-3} exhibited two broad diffraction peaks. The peak positioned at 1.4 (2θ) corresponds to the d_{100} diffraction giving a lattice parameter of 6.31 nm, and a pore-to-pore distance of 7.28 nm. A second peak is also observed and may be attributed to the d_{110} or d_{200}. Using the hkl spacings for a hexagonally packed material peaks with a ratio of $1:\sqrt{3}:2$ indicates hexagonal structuring. From this, we can predict that the peak at 2.65 (2θ) corresponds to diffraction from the d_{200} plane. The existence of 2 peaks (1.4 and 2.65 (2θ)) suggests that the template mixture is well ordered (long range ordering is apparent).

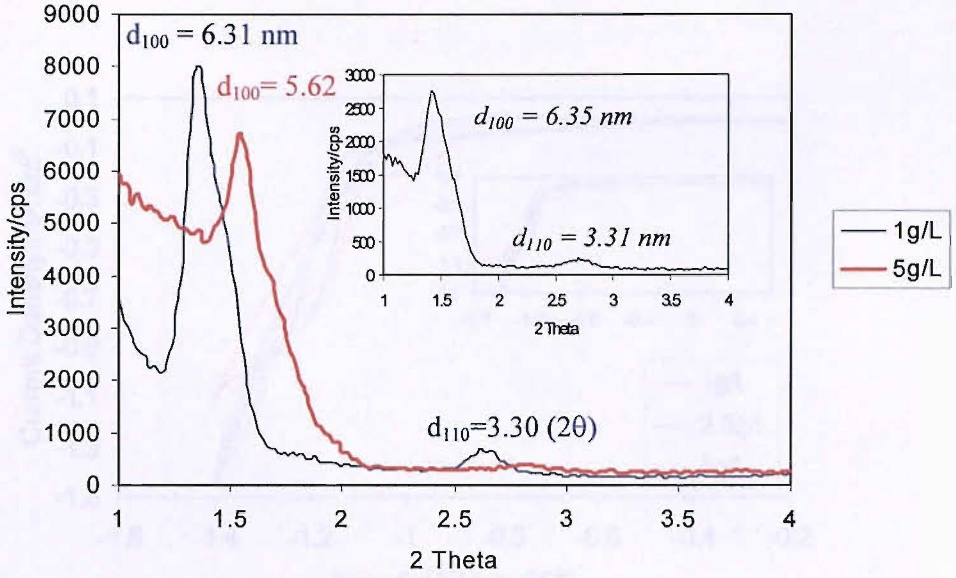

The low angle XRD pattern for a template mixture prepared with 5.0 g dm^{-3} is also shown in figure 5.21. This clearly reveals a single primary reflection at 1.57 ° (2θ) which translated into a lattice parameter of 5.62 nm. The liquid crystal template mixture is ordered and characteristic of a hexagonally ordered phase created using a $Zn(NO_3)_2$ precursor salt solutions and non-ionic surfactants (as with TeO_2 and $CdSO_4$ in sections: 3.51 and 4.51).

5.5.2.2 Cyclic voltammetry

A cyclic voltgammogram of an ITO electrode immersed in a template mixture composed of 55 wt.% Brij®56 and a 45 wt.% solution containing 0.1 M zinc nitrate and various concentrations (1.0, 2.5 and 5.0 g dm^{-3}) of sodium ligninsulfonate is shown in figure 5.22. All three scans commence at 0.0 V and were scanned negatively. There are no faradic responses until -0.4 V *vs.* SCE, after which a gradual increase in the cathodic current is observed for all concentrations of the lignosulfonic acid. This increased is assumed to be the onset of zinc oxide electrodeposition. In the reverse scan, no anodic current is evident, which is attributed to the stability of the electrodeposited ZnO films. The current response reveals a slight change due to the addition of the various sodium ligninsulfonate concentrations (figure 5.22). Increasing the concentration of the sodium

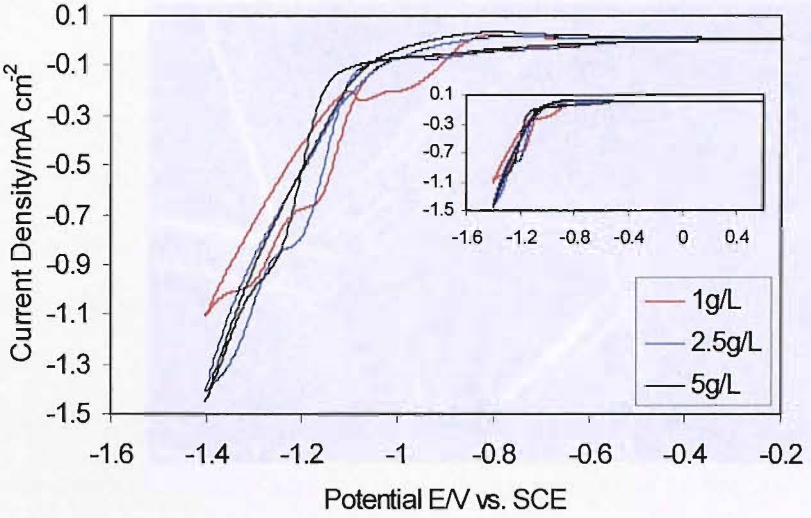

Figure 5.22: Cyclic voltammetry of an ITO electrode in a liquid crystal mixture containing a 0.1 M solution of zinc nitrate (45 wt.%), Brij®56 (55 wt.%) and 1, 2.5 and 5 g dm^{-3} lignosulfonic acid. Inset shows that there are not faradaic responses in the cyclic voltammetry at potentials greater than -0.4 V *vs.* SCE.

ligninsulfonate shows a slight increase in the current densities. For a concentration of 1.0 g dm^{-3} the current density reaches -1.1 mA cm^{-2}, and this increases to 1.55 mA cm^{-2} and 1.7 mA cm^{-2} for 2.5 g dm^{-3} and 5.0 g dm^{-3}, respectively. This is further confirmed by the appearance of the films; at –0.745 V the film there is no apparent deposition visible by the eye, however at –1.145 V *vs.* SCE the films are white and non-transparent. This will be further studied in the following section.

5.5.3 Scanning electron microscopy (SEM)

5.5.3.1 Modifying the electrodeposition parameters

Figures 5.23a to c show the surface morphology of H$_I$-eZnO films electrodeposited using three different concentrations of lignosulfonic acid. The additive was added at 1.0, 2.5 and 5.0 g dm^{-3} concentrations to 0.1 M solution of zinc nitrate solutions. Then 45 wt.% of this solution was mixed with 55 wt.% Brij®56. This liquid crystal template mixture was used to fabricate H$_I$-eZnO films at a deposition potentials of -0.745 V,

-0.845 V and -1.145 V *vs.* SCE and a cell temperature of 50 °C.

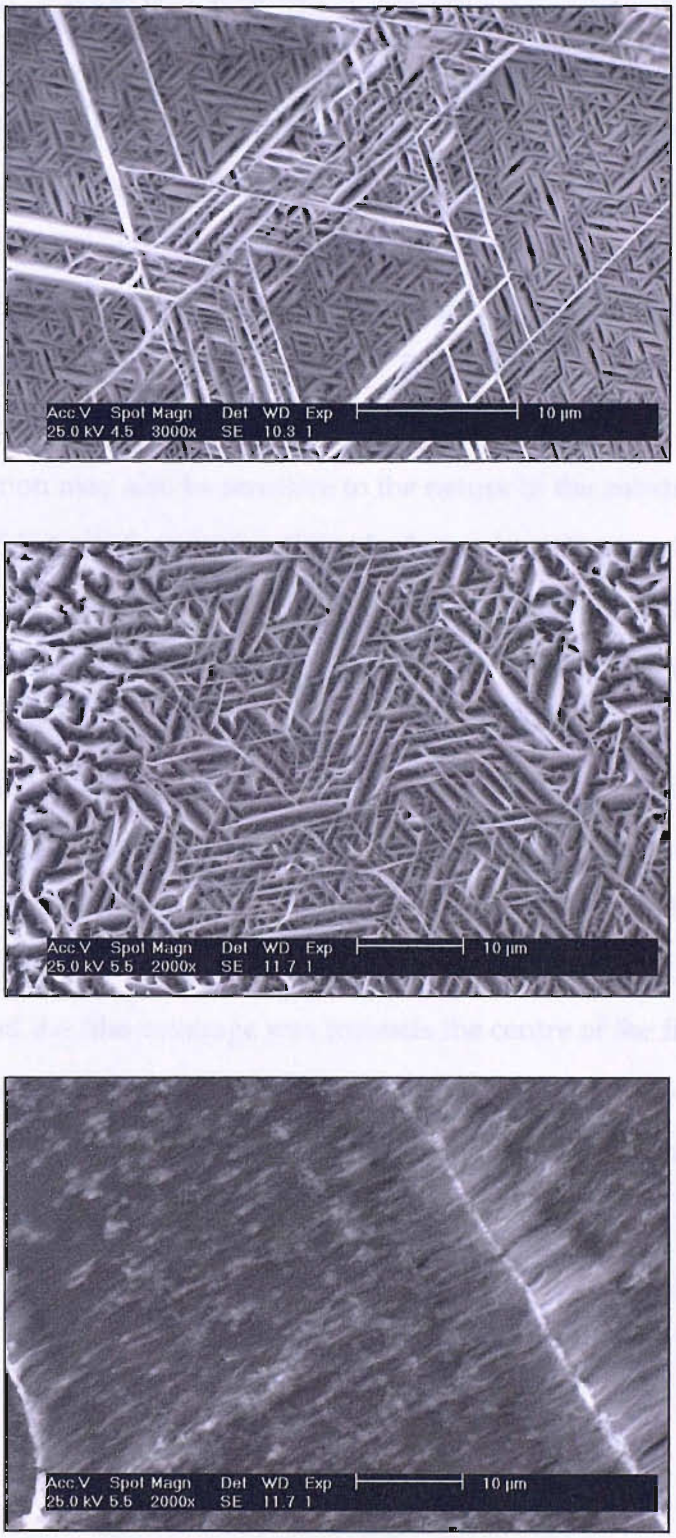

Figure 5.23: SEM micrographs of three films electrodeposited at -0.845 V *vs.* SCE at 50 °C. The template mixture contained a 45 wt.% solution of 0.1 M zinc nitrate, three concentrations of lignosulfonic acid (a). 1.0, (b). 2.5, (c). 5.0 g dm^{-3} and 55 wt.% Brij®56.

Figure 5.23 shows the effect of sodium ligninsulfonate at 1.0, 2.5 and 5 g dm^{-3} at a deposition potential of -0.845 V *vs.* SCE. The results, show a variety of surface morphologies, most interesting is image 5.23a which shows a highly ordered crystal lattice comprising triangular shaped terraces. Image 5.23b also shows similar features, however with less well-defined growth structures. Finally, figure 5.23c illustrates the deposition of H_I-eZnO using an electrolyte containing 5.0 g dm^{-3}. EDX results show that there are still visible areas of the electrode surface. This indicates the poor coverage of the electrode using these conditions. This is a direct result of the sodium ligninsulfonate's ability to inhibit the growth of ZnO on the surface of the electrode, but also the deposition may also be sensitive to the nature of the substrate. From the results, using -0.845 V *vs.* SCE and 1.0 or 2.5 g dm^{-3} of sodium ligninsulfonate. The adsorption sites on the surface may have been replaced with the additive thus reducing the deposition rate and sites when 5.0 g dm^{-3} of the additive is used.

Using a concentration of 1 g dm^{-3} in a 45 wt.% 0.1 M solution of zinc nitrate and 55 wt.% Brij$^{®}$56, H_I-eZnO films were electrodeposited at different potentials. Figure 5.24a and b show SEM images for H_I-eZnO films deposited at-0.845 V and -1.145 V *vs.* SCE, respectively. The films were white and granular. For figure 5.24b the grain lengths were up to 1 μm and the film coverage was towards the centre of the film, however the working electrode edges revealed a reduced coverage. Again, at -0.845 V *vs.* SCE the film appeared more ordered, with a network of diagonally aligned crystals on the surface.

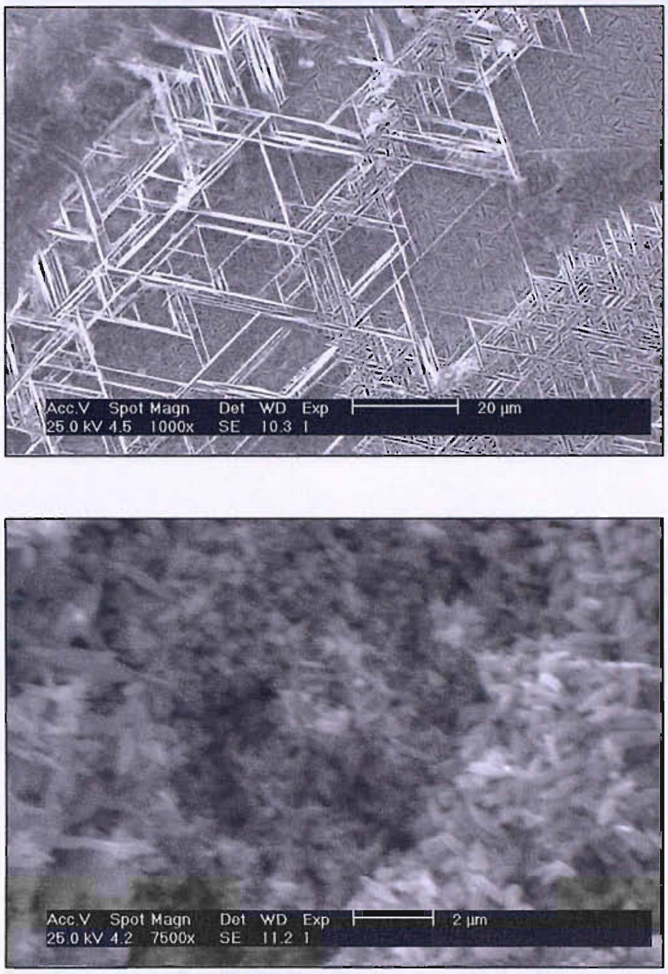

Figure 5.24: SEM micrographs of two films electrodeposited at (a). -0.845 and (b). -1.145 V *vs.* SCE. The mixture contained a 45 wt.% solution of 0.1 M zinc nitrate/1.0 g dm^{-3} lignosulfonic acid and 55 wt.% Brij®56.

A higher concentration of the additive (5.0 g dm^{-3}) was also employed. At -0.745 V, SEM images showed no visible deposition in the centre of the film (only around the edges). EDX analysis showed no results for zinc. Only a colour difference between deposition area and the substrate edge could be observed, however, low angle XRD did reveal a peak at ~1.5 ° (2θ). At more negative deposition potentials (-0.845 V *vs.* SCE) the film was dendritic, thick but lacked homogenous coverage.

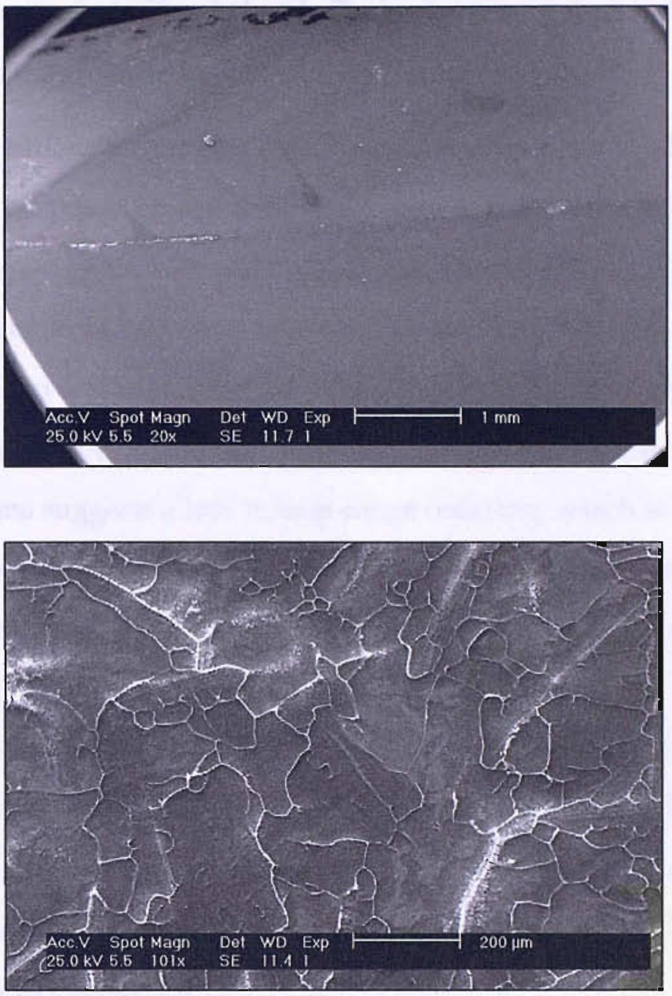

Figure 5.25: SEM micrographs of two films electrodeposited at (a). -0.745 V and (b). -0.845 V *vs.* SCE. The mixture contained a 45 wt.% solution of 0.1 M zinc nitrate/5.0 g dm^{-3} lignosulfonic acid and 55 wt.% Brij®56.

These images show the effect of adding sodium ligninsulfonate to the liquid crystal template mixture. At 1.0 g dm^{-3} the deposition occurs but at 5.0 g dm^{-3} the effect of the additive inhibits growth to such an extent that coverage no longer occurs on the electrode surface. At 2.5 g dm^{-3} ZnO deposition does occur with total film coverage, however the thickness of the film is severally depleted by comparison to the 1 g dm^{-3}.

5.5.3.2 Low angle XRD of H_I-eZnO electrodeposited in the presence of sodium ligninsulfonate

The diffraction pattern for the H_I-eZnO film, electrodeposited at –1.145 V *vs.* SCE from the domains of the liquid crystal template, is shown in figure 5.26. The diffraction pattern has been magnified. A well-defined, but broad peak at 1.2 (2θ) corresponding to a lattice parameter of 7.06 nm is observed for the deposited film. A pore-to-pore distance of 8.15 nm was calculated, using $d_{100}/\cos 30°$. The disappearance of the higher order diffraction peak (d_{200}) and the appearance of a broad d_{100} peak for the mesoporous films suggests a loss in long-range ordering, which is common when fabricating materials using TLCT by electrodeposition. This has been reported in numerous papers employing TLCT (*31, 45, 46*). Using only 1.0 g dm^{-3} of the additive consistently reproduced H_I-eZnO films. The addition of 1.0 g dm^{-3} sodium ligninsulfonate to a 45 wt.% of a solution containing 0.1 M zinc nitrate and 55 wt.% Brij®56 has shown little effect on the appearance of the low angle XRD template mixture and by comparison to a template mixture absent of additives (inset figure 5.16). Only the mesoporous ZnO film containing the 1.0 g dm^{-3} revealed a secondary d_{200} peak at approximately 2.6 (2θ).

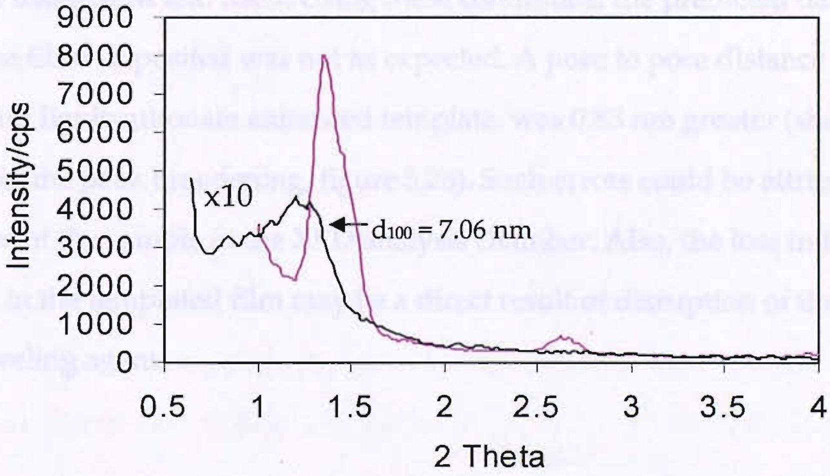

Figure 5.26: Low angle XRD patterns of a hexagonal template mixture consisting of 55 wt.% Brij56 and 45 wt.% of a solution containing 0.1 M zinc nitrate and 1.0 g dm^{-3} lingosulfonic acid (pink) and the electrodeposited film from the domains of the mixture (black).

Using an electrolyte solution containing 5.0 g dm^{-3} of the sodium ligninsulfonate however, the film did not exhibit any mesoporosity under XRD analysis. However, EDX analysis showed that the films contained equal amounts of zinc and oxygen. Although H_I-eZnO films could be prepared using an additive to modify the deposition rate, this films remained white and dendritic and not transparent as required.

5.5.3.3 Summary

Using high concentrations (2.5 and 5.0 g dm^{-3}) of the additive produced very small amounts of the electrodeposited material and in some cases no ZnO was visible by SEM. It is thought that the lignosulfonic acid blocks nucleation sites on the electrode surface and also reducs growth of nucleation centres on the surface. At concentrations of 1 g dm^{-3} zinc oxide film growth was possible with clearly defined, well-ordered lattice structure.

The rate of deposition was affected by the deposition potential at all concentrations of the additive. The use of sodium ligninsulfonate as a leveling agent in the electrodeposition of H_I-eZnO was at its most improved at 1.0 g dm^{-3} in a solution of 45 wt.% 0.1 M zinc nitrate and 55 wt.% Brij®56 at a deposition potential of -1.145 V *vs.* SCE and 50 °C. Although the film morphology was not featureless and flat as required, structural enhancement (highly defined crystals with an ordered ZnO lattice) was observed using SEM and XRD. Using these conditions, the predicted nanostructuring within the films deposited was not as expected. A pore to pore distance of 8.15 nm, for the sodium ligninsulfonate enhanced template, was 0.83 nm greater (shown by the increase in the peak broadening, figure 5.26). Such errors could be attributed to the alignment of the sample in the XRD analysis chamber. Also, the loss in the degree of ordering in the templated film may be a direct result of disruption of the mesophase. by the leveling agent.

5.6 CONCLUSIONS

H_I-eZnO films can be successfully prepared on both ITO and Au by electrodeposition using a precursor salt solution containing 45 wt.% of a 0.1 M zinc nitrate solution and 55 wt.% Brij®56. The electrodeposited films were a near direct cast of the mesoporous template mixture, with some error due to the loss of ordering during the deposition process. Template mixtures electrolyte anion and cation interaction with the head groups of the surfactants caused some hexagonal phase stability enhancement. This enhancement was confirmed by an increase in the isotropisation temperature observed by POM.

In general, the films were white and dendritic, but the films were in full agreement with wide angle XRD results for both the powdered and thin film ZnO. The films had a preferred orientation of <002> on both polycrystalline Au and ITO which equates to growth perpendicular to the substrate. In some cases, the orientation could be altered by a variation in the growth conditions. Variations in the pulse plating conditions (E_{off} and E_{on}) for H_I-eZnO and the electrodeposition potential -1.045 V to -1.245 V *vs.* SCE greatly affected the crystal structure of the films. This shows the sensitive nature of the electrodeposition of mesoporous ZnO films and that stringent control over the experimental conditions is required.

In order to use these mesoporous films in photoelectrochemical cells or optoelectronic devices, it would be necessary to improve the transparency of the films, which is influenced by the surface morphology of the film. A number of attempts were made in order to produce optically flat films; modulated potential electrodeposition, the addition of additives, and also by optimisation of the experimental parameters. All these methods reproducibly created different surface morphologies. Despite this, EDX and wide angle characterisation confirm the identity of the films to be ZnO with a general preferential orientation of <002>.

5.7 REFERENCES

1. L. Stolt, J. Hedstrom, M. Ruckh, J. Kessler, K. O. Velthaus, H. W. Schock, *Applied Physics Letters* **62**, 597 (1993).
2. D. Lincot, B. Canava, S. Quenet, S. Peulon, H. W. Schock, paper presented at the 14th European Photovoltaic Solar Energy Conference 1998.
3. T. Ikeda *Solar Energy Materials and Solar Cells* **34**, 379 (1994).
4. S. Sen, D. J. Leary, C. L. Bauer, *Thin Solid Films* **94**, 7 (1982).
5. Y. Segawa, A. Ohtomo, K. Kawasaki, H. Koinuma, Z. K. Tang, P. Yu, W. L. Wong, *Physical Staus. Solidi.* **669** (1997).
6. K. Vandeusden, C. H. Seager, W. L. Warren, D. R. Tallant, J. A. Voigt, *Applied Physics Letters* **68**, 4034 (1996).
7. Y. Chen, D. M. Bagnall, Z. Zhu, T. Sekiuchi, K. Park, K. Hiraga, T. Yao, S. Koyama, Y. M. Shen, T. Goto, *Journal of Crystal Growth* **181**, 165 (1997).
8. M. G. Ambia, M. N. Islam, M. O. Hakim, *Journal of Material Science* **29**, 6575 (1994).
9. S. Peulon, D. Lincot, *Advanced Materials* **8**, 166 (1996).
10. M. Izaki, T. Omi, *Applied Physics Letters* **68**, 2439 (1996).
11. R. Liu, A. A. Vertegel, E. W. Bohannan, T. A. Sorenson, J. A. Switzer, *Chemical Materials* **13**, 508 (2001).
12. M. H. Wong, *Nanotechnology* **14** (2003).
13. K. Keis, C. Bauer, G. Boschloo, A. Hagfeldt, A., K. Westermark, H. Rensmo, H. Siegbahn, *Journal of Photochemistry and Photobiology A: Chemistry* **148**, 57 (2002).
14. K. Keis, E. Magnusson, H. Lindstrom, S. Lindquist, A. Hagfeldt, *Solar Energy Materials and Solar Cells* **73**, 51 (2002).
15. K. Keis, L. Vayssieres, S. Lindquist, A. Hagfeldt, *NanoStructured Materials* **12**, 487 (1999).

6\. B.Mari, M. Mollar, A. Mechkour, B. Hartiti, M. Perales, J. Cembrero, *Microelectronics Journal* **35**, 79 (2004).

17. H. Luo, J. Zhang, Y. Yan, *Chemistry of Materials* **15**, 3769 (2003).
18. J. A. Switzer, *American Ceramics Society Bulletin* **66**, 1521 (1987).
19. L. Gal-Or, I. Silberman, R. Chaim, *Journal of the Electrochemical Society* **138**, 1939 (1991).
20. B. Canava, D. Lincot, *Journal of Applied Electrochemistry* **30**, 711 (2000).
21. T. Pauporte, D. Lincot, *Electrochemica Acta* **45**, 3345 (2000).
22. A. Goux, T. Pauporte, J. Chivot, D. Lincot, *Electrochemica Acta* **50**, 2239 (2005).
23. B. O' Regan, V. Sklover, M. Gratzel, *Journal of the Electrochemical Society* **148**, C498 (2001).
24. S. Peulon, D. Lincot, *Journal of the Electrochemical Society* **145**, 864 (1998).
25. I. S. Nandhakumar, T. Gabriel, M. Markham, D. C. Smith, J. J. Baumberg, G. S. Attard, *Chemical Communications* **12**, 1374 (2004).
26. T. Gabriel, I. S. Nandhakumar, G. S. Attard, *Electrochemical Communications* **4**, 610 (2002).
27. J. Swtizer, *Journal of the Electrochemical Society* **133**, 722 (1986).
28. M. Pourbaix, N. de Zoubov, in *Atlas d'equilibres Electrochimiques*. (Gaurthier Villers, Paris, 1963) pp. 406-413.
29. M. Izaki, S. Watase, H. Takahashi, *Applied Physics Letters* **83**, 4930 (2003).
30. K. Nomura, N. Shibata, M. Maeda, *Journal of Crystal Growth* **235**, 224 (2001).

31. G. S. Attard, P. N. Bartlett, N. R. B. Coleman, J. M. Elliot, J. R. Owen, J. H. Wang, *Science* **278**, 838 (1997).
32. V. Tohver, P. V. Braun, M. U. Pralle, S. I. Stupp, *Chemistry of Materials* **9** (1997).
33. N. B. Bartlett, J. Marwan, *Microporous and Mesoporous materials* **62**, 73 (2003).
34. Z. H. Gu, T. Z. Fahidy, *Journal of the Electrochemical Society* **146**, 156 (1999).
35. L. Zhang, Z. Chen, Y. Tang, Z. Jia, *Thin Solid Film* **192,** 24 (2005).
36. M. Li, J. Zhai, H. Liu, Y. J. Song, L. D. Zhu, *J. Phys. Chem. B* **107**, 9954 (2003).
37. Y. F. Mei, G. G. Siu, R. K. Y. Fu, P. K. Chu, Z. M. Li, Z. K. Tang, *Applied Surface Science* (2005).
38. M. Izaki, T. Omi, *Journal of the Electrochemical Society* **143**, L53 (1996).
39. M. Izaki, *Journal of the Electrochemical Society* **146**, 4517 (1999).
40. R. E. Maroti, *Solar energy and solar cells*, **85** (2004).
41. A. Stankeviciute, K. Leinartas, G. Bikulcius, D. Virbalyte, A. Sudacivi, E. Juzeliuna, *Journal of Applied Electrochemistry* **28**, 89 (1998).
42. J. Lee, Y. Tak, *Electrochemical and Solid State Letters* **4**, C63 (2001).
43. R. Wills, PhD, University of Southampton (2004).
44. T. Yamamoto, T. Shiosaki, A. Kawbata, *Journal of Applied Physics* **51** (1980).
45. A. H. Whitehead, J. M. Elliot, J. R. Owen, G. S. Attard, *Chemical Communications*, 331 (1999).
46. N. B. Bartlett, P. N. Birkin, A. M. Ganhem, P. de Groot, M. Sawicki, *Journal of the Electrochemical Society* **148**, C119 (2001).

CHAPTER SIX:

FINAL CONCLUSIONS AND FUTURE WORK

In this thesis mesoporous tellurium, cadmium telluride and zinc oxide films have been prepared using a non-ionic surfactant template by varying experimental paramters. Consequently, the development of an internal porous structure introduces a high surface area and also creates form birefringence within the material. The ~3 nm sized pores are within the required size to affect the rate of light traveling through the material. Thus, bandgap modification of the CdTe films can be carried out.

Control over the surfactant template mixture is paramount for the mesoporous structure. In order to avoid poor mesoporous structures of the semiconductor films during the deposition process carfeul control of the pH, concentration, surfactant composition, substrate deposition potential is required has been shown to be vital. Also, the final film must be flat, adherent and reflective leading to greater control over quantum confinement within the material. Based on these conditions the opportunity to use complexing agents in plating baths allows better control over depositon rates by improving the current. Currently H_I-eTe and H_I-eCdTe films electrodeposited over five hours give a thickness <1 μm thick, complexing agents could provide a route to shorter deposition times and therefore thicker films. The electrodeposition H_I-eZnO occurs at a faster rate than with H_I-eCdTe on both ITO and Au. As a result the electrodeposition of mesoporous ZnO films may require additives to produce high quality, flat films which may be transparent.

Further work is also required to produce films with the necessary optical properties to be used in photoelectrochemical cells. Initial work for PEC cells using CdTe and ZnO has been promising, initial photocurrent results both showing differences between the bulk films and the mesoporous films. Although not conclusive the results indicate that given the complexity of the experiement careful modification of the conditions may lead to potentially strong evidence for the mesooporous enhancement of increased photoefficiencies through the introduction nanostructuring within a thin semiconducting film.